

MICROSTRUCTURE AND PHASE BEHAVIOR IN  
COLLOIDS AND LIQUID CRYSTALS

Matthew Alan Lohr

A DISSERTATION

in

Physics and Astronomy

Presented to the Faculties of the University of Pennsylvania

in

Partial Fulfillment of the Requirements for the Degree of Doctor of Philosophy

2014

---

Arjun G. Yodh, Professor of Physics and Astronomy  
Supervisor of Dissertation

---

Randall D. Kamien, Professor of Physics and Astronomy  
Graduate Group Chairperson

Dissertation Committee

Randall D. Kamien, Professor of Physics and Astronomy

Peter J. Collings, Adjunct Professor of Physics and Astronomy

Kathleen J. Stebe, Professor of Chemical and Biomolecular Engineering

Gary M. Bernstein, Professor of Physics and Astronomy

# Dedication

Dedicated to my wife, Melissa.

Thank you for our life together.

# Acknowledgements

This work wouldn't exist without the constant support of many people over many years.

My wife, Melissa, has been extremely important in keeping me sane, fed, groomed and grounded throughout my graduate studies. When I was writing my undergraduate thesis, she walked into my room and noticed I had been so distracted by writing that I had let a bottle of detergent spill into the middle of the floor. My functionality during the writing of *this* thesis dissertation is largely due to her. More importantly, she makes me happier than I could ever imagine.

My advisor, Prof. Arjun Yodh, has been a great mentor who has been very supportive when I became frustrated with my research. During my graduate school visits, I asked every professor I met what they thought the worst thing about their department was. Many had clever and circuitous answers (“We don't have enough graduate students!”). Arjun was the only one who gave me a straightforward answer of, “What? No, there's nothing wrong with Penn. You should just come here.” I have since learned such frankness is an important part of being a good communicator, and I hope that his sincere, direct, patient and good-natured advice has molded me into a better scientist.

My family, currently spread across the country and globe, has been a constant source of love and support throughout my life and academic career. My parents, beyond being extremely supportive through my young and adult life, have always been thoughtful about my gifts and values, pushing me towards a fulfilling career while always encouraging my interests (be they science, music, theater, or beer). Though I love all my siblings equally, I have to give a special shout-out in this thesis to my brother Mike, a fellow scientist who has constantly encouraged

me to challenge my intellectual limits and, to quote Mr. Edward Abbey, “Subvert the Dominant Paradigm.”

The Yodh Soft Matter Group is full of awesome people who also happen to be great scientists. To my fellow graduate students, Dan Chen, Oni Basu, Peter Yunker, (Matt) Gratale, Zoey Davidson, and Wei-Shao Wei; to our postdocs, Zexin Zhang, Ke Chen, Tim Still, Ye Xu, and Joonwoo Jeong; and to our academic collaborators, Prof. Kevin Aptowicz and Prof. Piotr Habdas: you all have made this group a fun place to pursue one’s Ph. D, and I owe almost everything I learned in graduate school to the lot of you. I could not have hoped for a better group of people to work with over these years, and I hope to continue collaborating with all of you in the future.

Beyond my immediate group, I have had some great collaborators in and around Penn, without whom my work would be boring and incomplete. To Ahmed Alsayed, Marcello Cavarello, Mohammed Gharbi, Prof. Kathleen Stebe and Prof. Peter Collings, thank you for all your work sharing your experimental expertise and valuable insight into sometimes mysterious and temperamental materials. To Bryan Chen, Prof. Randall Kamien, Daniel Beller, Carl Goodrich, and Daniel Sussman, thank you for performing complex derivations and simulations to support my results, for taking the time to patiently explain finer points of various theories, and, most importantly, for sharing your scotch with me.

Speaking of Penn, I have to give credit to the Penn Physics department. Ever since I first visited Penn back when I was deciding where to go for graduate school, it was clear to me that this was a department full of well-rounded and interesting people. I am proud to have been a part of it, and I’m glad for all of the friends I’ve made there. Also, I have to thank the staff of the LRSM for making it a welcoming building to visit every day.

I never could have imagined that a close-knit group of open, friendly, passionate people would be interested in the same squishy things I thought were cool. So I have to thank the soft matter community at large. Though I will be stepping into a career in industry research and development, I hope to stay in touch, and can't wait to see the great new work you all produce on self-assembly, phase behavior, and nonlinear phenomena.

I am extremely grateful for the opportunities I have had to pursue undergraduate research, so I have to thank Prof. Peter Schiffer, Prof. Daniel Lathrop, Prof. Diane Henderson, Dr. Charles Doumalin, and Dr. Masafumi Fukuto, as well as the NSF's REU program, for getting me involved in interesting research early on. I still draw on things I learned from your labs to this very day.

I finally have to thank the city of Philadelphia for being an interesting and affordable place to live, and the perfect place for a budding scientist to spend formative years. Also, need to thank my cat Leela (a native of University City, found crouched under a car outside DRL by my friends and colleagues Peter Yunker and Erin Buckley) for being the sweetest pet any man could ask for, and comforting me during the more strenuous periods of my graduate career.

# ABSTRACT

## MICROSTRUCTURE AND PHASE BEHAVIOR IN COLLOIDS AND LIQUID CRYSTALS

Matthew Alan Lohr

Arjun G. Yodh

This thesis describes our investigation of microstructure and phase behavior in colloids and liquid crystals. The first set of experiments explores the phase behavior of helical packings of thermoresponsive microspheres inside glass capillaries as a function of volume fraction. Stable helical packings are observed with long-range orientational order. Some of these packings evolve abruptly to disordered states as the volume fraction is reduced. We quantify these transitions using correlation functions and susceptibilities of the orientational order parameter,  $\psi_6$ . The emergence of coexisting metastable packings, as well as coexisting ordered and disordered states, is also observed. These findings support the notion of phase-transition-like behavior in this class of quasi-one-dimensional systems.

The second set of experiments investigates cross-over behavior from glasses with attractive interactions to sparse gel-like states. In particular, the vibrational modes of quasi-two-dimensional disordered colloidal packings of hard colloidal spheres with short-range attractions are measured as a function of packing fraction. A crossover from glassy to sparse gel-like states is indicated by an excess of low-frequency phonon modes. This change in vibrational mode distribution is found to arise from highly localized vibrations that tend to involve individual

and/or small clusters of particles with few local bonds. These mode behaviors and corresponding structural insights may serve as a useful signature for glass-gel transitions in wider classes of attractive packings.

A third set of experiments explores the director structures of aqueous lyotropic chromonic liquid crystal (LCLC) films created on square lattice cylindrical-micropost substrates. The structures are manipulated by modulating the concentration-dependent elastic properties of LCLCs via drying. Nematic LCLC films exhibit preferred bistable alignment along the diagonals of the micropost lattice. Columnar LCLC films form two distinct director and defect configurations: a diagonally aligned director pattern with local squares of defects, and an off-diagonal configuration with zig-zag defects. We suggest that the formation of these patterns is tied to the relative free energy costs of splay and bend deformations in the precursor nematic films. The observed nematic and columnar configurations are understood numerically using a Landau-de Gennes free energy model. This work provides first examples of quasi-2D micropatterning of LC films in the columnar phase and the first micropatterning of lyotropic LC films in general; the work also demonstrates alignment and configuration switching of typically difficult-to-align LCLC films via bulk elastic properties.

# Contents

<b>Dedication</b>	<b>ii</b>
<b>Acknowledgements</b>	<b>iii</b>
<b>Abstract</b>	<b>vi</b>
<b>List of Figures</b>	<b>xxxii</b>
<b>1 Introduction</b>	<b>1</b>
1.1 Structure and Melting of Helical Packings . . . . .	3
1.2 Vibrational Signatures of Gel-like and Glassy Colloidal Packings . . . . .	6
1.3 Microscopic Ordering of Lyotropic Chromonic Liquid Crystals . . . . .	9
1.4 Organization of Thesis . . . . .	12
<b>2 Helical Packings and Phase Transformations of Soft Spheres in Cylinders</b>	<b>13</b>
2.1 Introduction . . . . .	13
2.2 Contextual and Theoretical Background . . . . .	15
2.2.1 Helical Packing Structures . . . . .	15

2.2.2	Transformations of Helical Structures . . . . .	19
2.2.3	Phase Transitions . . . . .	21
2.2.3.1	Phase Transitions, Long Range Order and Dimensionality . . . . .	22
2.3	Experimental Methods . . . . .	28
2.3.1	pNIPAm microspheres . . . . .	28
2.3.1.1	pNIPAm Synthesis and Fluorescent Functionalization . . . . .	29
2.3.1.2	pNIPAm Particle Diameter Characterization . . . . .	30
2.3.2	Microtube Geometry and Sample Configuration . . . . .	32
2.3.3	Fluorescence Confocal Microscopy . . . . .	33
2.3.3.1	Background on Confocal Microscopy . . . . .	34
2.3.3.2	Advantages and Disadvantages of TSM and CLSM . . . . .	36
2.4	Results and Analysis . . . . .	38
2.4.1	Characterization of 3D Structure . . . . .	38
2.4.2	Long-Range Orientational Order in Achiral Packings . . . . .	43
2.4.3	Theoretical Model for Long-Range Orientational Order in Helical Packings . . . . .	45
2.4.4	Orientational Order Parameter, Susceptibility, and Evidence of a Phase Transition in Experiment . . . . .	49
2.4.5	Structural Transformations in Chiral Packings . . . . .	53
2.5	Conclusions . . . . .	54
<b>3</b>	<b>Low-Frequency Modes as a Hallmark of Structural Crossovers in Quasi-2D Dense Attractive Colloidal Packings</b>	<b>56</b>
3.1	Introduction . . . . .	56

3.2	Contextual and Theoretical Background . . . . .	57
3.2.1	Attractive Glasses . . . . .	57
3.2.2	Gels . . . . .	59
3.2.3	Differences between Gels and Attractive Glasses . . . . .	60
3.2.4	Phonons in Disordered Solids . . . . .	61
3.2.4.1	Conventional Low-Frequency Phonon Behavior: The Debye Model . . . . .	61
3.2.4.2	Low-Frequency Phonons in Disordered Solids . . . . .	62
3.3	Experimental and Analytical Methods . . . . .	65
3.3.1	Sample Preparation . . . . .	65
3.3.1.1	Issues Forming Quasi-2D Thermal Attractive Monolayers . . . . .	65
3.3.1.2	Novel Monolayer Spreading From Lutidine Wetting . . . . .	67
3.3.1.3	Temperature Stability . . . . .	69
3.3.1.4	Monolayer Formation . . . . .	71
3.3.2	vDOS Calculation from Particle Trajectories . . . . .	71
3.3.3	Analytical Considerations for vDOS calculations . . . . .	74
3.4	Results and Discussion . . . . .	76
3.4.1	Conventional Structural Characteristics of Attractive Monolayers . . . . .	76
3.4.2	vDOS Shape as a Signature of Structural Transition . . . . .	80
3.4.2.1	Comparison of vDOS in Dense Packing to Simulations . . . . .	82
3.4.3	Localization of Low-Frequency Modes . . . . .	85

3.4.4	Qualitative Description of Structural Correlations to Localized Low-Frequency Modes . . . . .	88
3.5	Conclusion . . . . .	93

**4 Elasticity-Dependent Self-assembly of Micro-Templated Chromonic Liquid Crystal**

<b>Films</b>		<b>95</b>
4.1	Introduction . . . . .	95
4.2	Contextual and Theoretical Background . . . . .	97
4.2.1	Lyotropic Chromonic Liquid Crystals . . . . .	97
4.2.2	History of Chromonics . . . . .	100
4.2.3	Emerging Applications of LCLCs . . . . .	101
4.2.4	Barriers to Practical Application of LCLCs . . . . .	103
4.2.5	Elastic Deformations in LCLCs . . . . .	106
4.2.6	Defects in Columnar LCLCs . . . . .	108
4.3	Experimental and Numerical Methods . . . . .	110
4.3.1	Choice of LCLC Suspensions . . . . .	111
4.3.2	Synthesis and Loading of Micropost Arrays . . . . .	113
4.3.3	Polarizing Imaging and Director Field Analysis . . . . .	115
4.3.4	Numerical Modeling of Liquid Crystals in Micropost Arrays . . . . .	121
4.4	Results and Discussion . . . . .	124
4.4.1	Nematic Configurations . . . . .	124
4.4.1.1	Estimation of Anchoring Strength of Rubbing Alignment . . . . .	127
4.4.2	Columnar Configurations . . . . .	129

4.4.2.1	Experimentally Observed Columnar Patterns . . . . .	129
4.4.2.2	Numerical Reproduction of Columnar Patterns . . . . .	133
4.5	Conclusion . . . . .	137
<b>5</b>	<b>Preliminary Results: Novel Microstructures in Lyotropic Chromonic Liquid Crystals</b>	<b>138</b>
5.1	Nematic LCLC's in Micropost Arrays with a Deformed Interface . . . . .	139
5.2	Observations of Chiral LCLC Configurations in Tubes . . . . .	143
5.3	Mixtures of CLC and Surfactant Phases . . . . .	147
5.4	Diblock Copolymer Vesicles Suspended in CLCs . . . . .	150
5.5	Summary . . . . .	153
<b>6</b>	<b>Conclusions and Future Work</b>	<b>155</b>
6.1	Summary . . . . .	155
6.2	Future Work . . . . .	158
6.2.1	Three Dimensional Dynamics and Self-Assembly of Helical Structures	158
6.2.2	Precise Structural Nature and Generality of the Gel-Glass Crossover . .	161
6.2.3	Further Engineering of LCLC films via Microtemplating . . . . .	162
6.2.4	Continuing Work on Novel LCLC-Facilitated Microstructures . . . . .	163
	<b>Bibliography</b>	<b>164</b>

# List of Figures

1.1	Helical packings of spheres. (Left) Packings of balloons at festivals with (0,4,4) and (0,3,3) structures. (Middle right) Spherical candies arranged in a (0,6,6) structure in their cylindrical packaging. (Right) Fluorescence confocal microscopy image of a (2,3,5) packing of thermosensitive, micron-size pNIPAm particles in a glass microcapillary. . . . .	4
1.2	Qualitative phase diagram of disordered packings as a function of packing fraction ( $\phi$ ) and inter-particle attraction ( $U$ ). Images above illustrate an obviously sparse gel packing (left), obviously dense glassy packing (right), and an intermediate density packing of indeterminate phase (middle). . . . .	7
1.3	Cross-polarizing image of a drying droplet of a dilute DSCG suspension, showing a low-to-high concentration gradient from image top to bottom. Illustrations depict molecular structure in corresponding isotropic (I, top), nematic (N, middle) and columnar (M, bottom) regions. . . . .	10

2.1	Illustrations depicting the two-dimensional order of a hexagonal (2, 3, 5) structure (left) and a rhombic (3, 5) structure (right). Illustrations on the left demonstrate the three dimensional structure (adapted from [37]); illustrations on the right demonstrate the corresponding “unwrapped” two-dimensional structure. Particles on the edge are repeated for clarity. Numbers indicate relative distance along the tube direction; arrows indicate the wrapping of the 2D structured needed to create the corresponding 3D structure. . . . .	17
2.2	Illustration of possible ratios of inter-particle separation $d_{sep}$ and packing diameter $D$ (Fig. 2.13) at close packing for hexagonal and rhombic helical configurations (based on data from [37,53]). . . . .	19
2.3	(Left) Possible transformations between helical, hexagonally ordered states mediated by dislocation motion (adapted from [53]), arranged by ratio of packing diameter $D$ to particle radius $a$ at close packing. (Right) “Unwrapped” structure of a helical packing transitioning between a (2, 3, 5) (bottom, blue circles) and a (1, 4, 5) packing (top, purple circles) via motion of a 5-7 dislocation pair (yellow circles). . . . .	20
2.4	Qualitative illustrations of behavior of order parameters and associated susceptibilities with temperature in discontinuous 1st order (left) and continuous 2nd order phase transitions (right). . . . .	22

2.5	Bright field microscopy images of a dense aqueous suspension of pNIPAm microgel particles at 25 °C (left) and 28 °C (right). Particles deswell with increasing temperature (as depicted in the illustration insets), decreasing packing fraction, melting the packing from a crystalline packing (left) to an isotropic disordered fluid (right). Scale bar = 10 $\mu$ m. . . . .	29
2.6	Two-dimensional spatial correlation functions for the two sizes of pNIPAm microspheres (a, smaller, b, larger) used in helical packings experiments at different temperatures in a dilute suspension in a quasi-2D cell. Horizontal line indicates $g(r) = 1/e$ , an effective definition of sphere diameter. Shoulders in $g(r)$ curves in (a) occur due to the presence of one or two stuck particles in the field-of-view.	31
2.7	Approximate diameters for the smaller (blue ●) and larger (red ▲) pNIPAm particles used in helical packing experiments at different temperatures, with linear fits. . . . .	32
2.8	Imaging artifacts from confocal scans of helical packings. (a) Illustration of an $xy$ cross-section of the experimental configuration (not to scale). (b) Brightness of a confocal scan of a (2, 3, 5) packing averaged along the tube length ( $z$ direction) Inset: expected $xy$ brightness distribution with perfect imaging, given placement of particles in helical packing outlined by dotted lines. (c) $xz$ slices of a confocal scan of the same (2, 3, 5) packing close to the objective (bottom), at the middle of the packing (middle) and far from the objective (top). . . . .	36

2.9	Confocal scans of a $6\ \mu\text{m}$ polystyrene bead with a fluorescent shell, comparing TSM (a-b) and CLSM (c-d) scanning methods (taken from [87]). Note the slightly increased deformation from the expected circular shape in the CLSM images. . . . .	37
2.10	Confocal fluorescence cross-sections of six observed geometries of pNIPAM packings in microcapillaries (indicated by $(m, n, m + n)$ notation), along with corresponding reconstructions from particle locations determined using centroid-locating algorithms on full 3D confocal scans. . . . .	39
2.11	3D pair correlation function from positions of $\approx 1.7\ \mu\text{m}$ colloidal pNIPAM spheres in a (2,3,5) packing. First peak in $g(r)$ highlighted in red, with Lorentzian peak fit used to determine $d_{sep}$ is the blue dashed line. The vertical dotted line indicates cutoff for nearest neighbor determination. . . . .	40
2.12	Example of determination of helical structural integers $(m, n, m + n)$ . (a) Axial and azimuthal positions of tracked particles in a short axial section. The nearest neighbors of the green particle are highlighted in blue. Relative axial distance from the green particle listed to side. Note that the nearest neighbors have relative axial order of 2, 3 and 5. (b) Histogram of relative axial order for 1st, 2nd and 3rd closest nearest neighbors in the axial direction in a single packing. Peaks at values of 2, 3 and 5 indicate that this is a (2,3,5) packing. . . . .	41

2.13	Geometrical characteristics of observed structures, (2,2,4) (blue $\square$ ), (1,3,4) (purple $\circ$ ), (2,3,5) (green $\triangle$ ), (1,4,5) (cyan $\nabla$ ), (0,5,5) (red $\diamond$ ), (3,3,6) (dark green $\star$ ). Filled symbols indicate structures with observable Brownian motion. Dashed vertical lines indicate theoretical $D/d_{sep}$ values for predicted structures. Inset: Cartoon of axial cross-section of a (3,3,6) structure with $d_{sep} > d_{eff}$ . . . . .	42
2.14	Local maxima of orientational spatial correlation function $g_6(z)$ for samples with (2,2,4) packing (a) and (0,6,6) packing (b). Dashed lines: Full correlation function at $\phi/\phi_{max(224)} = 0.86$ and $0.63$ (a) and $\phi/\phi_{max(066)} = 0.64$ and $0.36$ (b), where $\phi_{max}$ is the maximum volume fraction for a given packing of hard spheres with the observed particle spacing. Empty symbols indicate samples with short-range order. Oscillations arise from the periodic distribution of particle positions along the tube axis. Full correlation functions were calculated for all volume fractions, but omitted for the sake of clarity. . . . .	44
2.15	Top: Mean values of translational (red $\blacktriangledown$ ) and orientational (blue $\blacksquare$ ) order parameters for (a) (2,2,4) and (b) (0,6,6) samples. Bottom: Orientational susceptibilities for (c) (2,2,4) and (d) (0,6,6) systems, for sample size = $75 \mu\text{m}$ ( $\circ$ ) and $\infty$ ( $\bullet$ ). Dashed vertical lines at $\phi/\phi_{max(224)} = 0.67$ and $\phi/\phi_{max(066)} = 0.38$ . . . . .	50
2.16	Snapshots of particle positions from a (0,6,6) structure exhibiting coexisting ordered and disordered domains. Color represents local variance of the phase of $\psi_6$ , $\langle \theta_{6j}^2 \rangle - \langle \theta_{6j} \rangle^2$ , in $1.2 \mu\text{m}$ segments. . . . .	52

2.17	Snapshots of particle positions from a (2,3,5) structure with emerging domains of (3,2,5) and (0,4,4) structures. Color represents phase of $\psi_{6j}$ , $\theta_{6j}$ , which characterizes packing orientation. Structures corresponding to each $\theta_{6j}$ given on right.	54
3.1	Qualitative phase diagram of disordered packings as a function of packing fraction $\phi$ and inter-particle attraction strength $U$ .	58
3.2	(Left) Illustration of the difference in low-frequency density of states $D(\omega)$ in an ordered Debye solid (black solid line) and a disordered glassy solid (dashed red line) with $d$ dimensions. Note the boson peak exhibited at low frequencies exhibited by the disordered solid. (Right) vDOS calculated from particle trajectories in quasi-2D disordered packings of thermal colloidal microgel spheres with soft repulsive interactions at various area fractions $0.840 < \phi < 0.885$ , adapted from [18]. Note low-frequency peak which changes height and frequency location with area fraction.	63
3.3	Formation of PS monolayers using water-lutidine phase separation, viewed under bright-field microscopy, with accompanying illustrations below. (Left) Three dimensional clusters form and sediment to the bottom of the sample cell at the aggregation temperature. (Middle) Heating sample above the aggregation regime causes phase separation of water and lutidine, pulling PS spheres into a monolayer of repulsive particles at the bottom surface. (Right) Lowering the temperature back to the aggregation regime pins particles to the surface, allowing them to aggregate from short-range attraction to a stable, percolating monolayer. Scale bars = $20\mu\text{m}$ .	67

- 3.4 Effect of temperature fluctuations in a lower stability objective heater (Bioptechs). (Bottom) Average particle displacement in a PS monolayer aggregate over the next 0.2 seconds during a temperature fluctuation of 0.1 °C, taking the sample out of the aggregation regime. (Top) Bright field microscope images of an attractive monolayer cluster during the temperature fluctuation. Red arrow indicates a sub-cluster of particles that undergoes an irreversible rearrangement during the temperature fluctuation. Scale bar = 10 $\mu$ m. . . . . 70
- 3.5 Higher stability objective heater setup (Bioscience Tools). (Left) Configuration of Biosciencetools heating objective collar and external temperature probe placed in sample immersion oil on an upright microscope setup (in experiments, an inverted microscope is used). (Middle) Temperature readout from external temperature probe immediately after an increase in set temperature from 33.4 °C to 33.8 °C. Temperature fluctuations stabilize after about 60 seconds from the start of the temperature change. (Left) Temperature readout from external temperature probe several minutes after a temperature change. Note fluctuations of  $\pm 0.03^\circ\text{C}$ . . . . . 70
- 3.6 Extrapolation of modes to compensate for low statistics in a packing with area fraction  $\phi = 0.84$ . (Left)  $1/\omega$  of several modes calculated for several ratios of  $N_p/N_f$ , with linear fits extrapolating these modes to the limit of  $N_p/N_f = 0$ . (Right) vDOS calculated for  $N_f = 7000$  (red points),  $N_f = 10000$  (green points), and extrapolation  $N_f \rightarrow \infty$  (black points). Note the increasingly better statistics do not significantly influence the vDOS curve shape at low frequencies. . . . . 76

3.7	vDOS curves of observed packings against unnormalized frequencies on a linear scale. Notice shifts in the location of the high-frequency peak from packing to packing. (Red, $\phi = 0.50 - 0.55$ ; Orange, $\phi = 0.56 - 0.62$ ; Yellow, $\phi = 0.64 - 0.65$ ; Green, $\phi = 0.69 - 0.74$ ; Olive, $\phi = 0.80$ ; Blue, $\phi = 0.81 - 0.82$ ; Black, $\phi = 0.84$ ). . . . .	77
3.8	Unprocessed bright-field microscopy images of investigated bidisperse attractive PS monolayer packings at various densities. Approximate area fraction $\phi$ indicated by inset. Scale bar = $10\mu\text{m}$ . . . . .	78
3.9	Bright-field microscopy images of investigated bidisperse attractive PS monolayer packings at various densities, with contrast and brightness enhanced for clarity. Approximate area fraction $\phi$ indicated by inset. Scale bar = $10\mu\text{m}$ . . . . .	79
3.10	Pair correlation function $g(r)$ of densest ( $\phi = 0.84$ , blue solid line) and sparsest ( $\phi = 0.50$ , red dotted line) observed packings. Sparse packing $g(r)$ shifted vertically by $+1.0$ for clarity. . . . .	80
3.11	(Left) Average number of nearest neighbors as a function of $\phi$ for experimentally observed packings, with a linear fit. (Right) Nearest neighbors vs. $\phi$ calculated for the particle positions of the observed $\phi = 0.84$ packing, with clusters of 2, 5 or 15 particles randomly removed. The dashed line is from the fit of experimental data on the left. . . . .	81

3.12 Vibrational density of states as a function of frequency  $\omega$  calculated from eigenmode distributions in packings with  $\phi < 0.67$  (i.e., six packings with  $\phi = 0.50, 0.55, 0.56, 0.62, 0.64,$  and  $0.65,$  each  $\pm 0.1$ ) (red lines) and  $\phi > 0.67$  (i.e., seven packings with  $\phi = 0.69, 0.74, 0.80, 0.80, 0.81, 0.82,$  and  $0.84,$  each  $\pm 0.1$ ) (blue lines). Thin, faded lines indicate vDOS for individual packings; thicker lines are the average vDOS for all packings in the sparse ( $\phi < 0.67,$  red) and dense ( $\phi < 0.67,$  blue) regimes. . . . . 82

3.13 vDOS curves from simulated dense, uniform bidisperse packings ( $\phi = 0.95,$  black;  $\phi = 0.898,$  purple;  $\phi = 0.833,$  blue;  $\phi = 0.816,$  green), along with an experimentally calculated vDOS curve from the densest observed packing ( $\phi = 0.84,$  red curve). Nearest neighbors determined by particle overlap in simulation indicated in the legend. . . . . 83

3.14 Histogram of participation ratio  $p(\omega)$  for low-frequency modes ( $\omega/\bar{\omega} < 0.1$ ) for packings with  $\phi < 0.67$  (open red squares) and  $\phi > 0.67$  (closed blue squares). Dashed line indicates  $p = 0.2$  cutoff for vDOS re-calculations. . . . . 85

3.15 Vibrational density of states re-calculated discounting highly localized modes ( $p < 0.2$ ) as a function of frequency  $\omega$  calculated from eigenmode distributions in packings with  $\phi < 0.67$  (i.e., six packings with  $\phi = 0.50, 0.55, 0.56, 0.62, 0.64,$  and  $0.65,$  each  $\pm 0.1$ ) (red lines) and  $\phi > 0.67$  (i.e., seven packings with  $\phi = 0.69, 0.74, 0.80, 0.80, 0.81, 0.82,$  and  $0.84,$  each  $\pm 0.1$ ) (blue lines). Thin, faded lines indicate vDOS for individual packings; thicker lines are the average vDOS for all packings in the sparse ( $\phi < 0.67,$  red) and dense ( $\phi > 0.67,$  blue) regimes. . . . . 86

3.16 Plots of particle locations from a sparser packing ( $\phi = 0.64 \pm 0.01$ ) overlaid with polarization eigenvector components corresponding to two modes with similar frequency ( $\omega/\bar{\omega} = 0.019$  (a) and  $0.021$  (b)) and significantly different localization ( $p(\omega) = 0.32$  (i.e., a more extended mode) (a), and  $p(\omega) = 0.069$  (i.e., a more localized mode) (b)). Scale bar =  $10\mu\text{m}$ . . . . . 87

3.17 Histograms of  $|\mathbf{e}_i(\omega)|$  for all modes with  $\omega/\bar{\omega} < 0.1$  in all observed packings with  $\phi < 0.67$  for extended ( $p > 0.2,$  solid squares) and localized ( $p < 0.2,$  empty squares) modes. . . . . 88

3.18	(a) Plot of particle locations in a $\phi = 0.64 \pm 0.01$ packing, with particles which have $ \mathbf{e}_i(\omega)  > 0.2$ for any mode where $\omega/\bar{\omega} < 0.1$ highlighted in red. Scale bar = $10\mu\text{m}$ . (b) Histogram of size of clusters of particles which dominate a low-frequency mode in sparse packings ( $ \mathbf{e}_i(\omega)  > 0.2$ , $\omega_n/\bar{\omega} < 0.1$ , $\phi < 0.67$ ). (c) Histogram of nearest neighbors per particle of each packing with $\phi < 0.67$ (black points) and for particles in all sparse packings which dominate a low-frequency mode (empty squares, $ \mathbf{e}_i(\omega)  > 0.2$ , $\omega_n/\bar{\omega} < 0.1$ ). . . . .	89
3.19	Illustration of single-particle deformations in a linear chain of particles, showing a particle with two neighbors in a line connected by springs (a) at its equilibrium position, with inter-particle spacing $r$ , (b) under a longitudinal deformation of size $\delta x$ , and (c) under a transverse deformation of size $\delta y$ . . . . .	91
3.20	Characterization of linear structure distribution in a packing with area fraction $\phi = 0.64$ . (Left) Histogram of $ \psi_{2i} $ for particles in the packing. (Right) Particle positions for $\phi = 0.64$ packing, with particles with $ \psi_{2i}  \geq 0.6$ highlighted in purple. Arrows indicate angle given by the complex phase of $\psi_{2i}$ . Scale bar = $10\mu\text{m}$ . . . . .	92
4.1	Illustration of the mesogen structure in lyotropic chromonic liquid crystals. (Top) Plank-like LCLC-forming molecules, when suspended in water, form linear aggregates, which act as mesogens for liquid crystal phases. (Bottom) The common liquid crystal phases of aggregates in chromonic liquid crystals are nematic (N) at intermediate concentrations and columnar (M) at higher concentrations. . . . .	99

4.2	Number of academic articles containing the keyword “chromonic” from Web of Science (open circles) and Google Scholar (filled squares) per year from the past few decades. . . . .	101
4.3	Nematic DSCG suspension placed between glass slides rubbed with an abrasive, creating an aligned film approximately $10\ \mu\text{m}$ thick, viewed under crossed-polarizers. Evaporation proceeds from an open edge beyond the upper right corner of the image, causing drying into the columnar phase. Though drying is slow, herringbone textures can be seen in the columnar phase. . . . .	105
4.4	Qualitative illustration of the director deformations contributing the splay ( $K_1$ ), twist ( $K_2$ ) and bend ( $K_3$ ) deformations. . . . .	107
4.5	Molecular structure and aqueous suspension phase diagram of disodium cromoglycate (left) and Sunset Yellow (right). Phase diagram of DSCG from [98]; phase diagram of SSY from [122]; molecule images from Wikipedia. . . . .	112

4.6 Configuration of micropost arrays loaded with liquid crystals. a) Bright-field microscopy image of an empty SU-8 micropillar array with post center spacing  $L = 14\mu\text{m}$ , diameter  $d = L/2 = 7\mu\text{m}$ , and height  $h = 5\mu\text{m}$ . Scalebar =  $50\mu\text{m}$ . Inset: close-up of microposts, indicating  $d$  and  $L$ . b) Schematic of micropost array configuration after loading with LCLC film. SU-8 microposts (1) sit atop a glass wafer (2). After being loaded with a LCLC (3), the wafer is placed in a glass petri dish (4) and immersed in hexadecane(5). c) Schematic of LCLC film loading procedure. A droplet of heated LCLC suspension is placed in a droplet onto a cleaned and heated micropost array where it begins to spread due to capillary forces (top); immediately afterward, hexadecane is placed to completely cover the sample, and LCLC droplet continues to spread (middle); after several minutes, the LCLC film has spread to cover the entire micropost array, leaving a level film at the post height (bottom). . . . . 114

4.7 Crossed-polarizer images from a movie of a rotating 30% wt/wt Sunset Yellow aqueous nematic film in an array of cylindrical microposts of diameter  $7\mu\text{m}$  and height  $5\mu\text{m}$ , overlaid with bright circles centered at tracked post centers. Polarizer and analyzer oriented along the vertical and horizontal of images. Scale bars =  $50\mu\text{m}$ . . . . . 116

4.8	Intermediate post-processing steps for post tracking a rotating 30 percent Sunset Yellow aqueous nematic film in an array of cylindrical microposts of diameter $7 \mu\text{m}$ and height $5 \mu\text{m}$ . (Top) Inverted cross-polarizer images, calculated from subtracting original image pixel values from the maximum pixel brightness. (Bottom) Inverted images convoluted with a uniformly bright disk of diameter equal to the post diameter, yielding near-gaussian peaks centered at the post centroids. Scale bar = $50 \mu\text{m}$ . . . . .	117
4.9	(a) Trajectories of 59 posts tracked through a $360^\circ$ sample rotation. (b) Trajectories with average translational motion per frame removed. . . . .	118
4.10	Selections of images of the SSY film from Figure 1, with net sample rotation and translation removed. Polarizer/analyzer are oriented at angles of $0^\circ$ ( $t = 0$ sec), $37^\circ$ ( $t = 6$ sec), and $55^\circ$ ( $t = 8$ sec) with respect to the vertical/horizontal of images. . . . .	118
4.11	(a) Selection of unprocessed video of SSY film under crossed-polarizers, when the polarizer/analyzer is oriented at an angle of $0^\circ$ ( $t = 0$ sec) with respect to the vertical/horizontal of the image. (b-c) Image brightness / transmitted light intensity at pixels 1 and 2, respectively, as a function of the angle of polarizer/analyzer to image horizontal/vertical, $\theta_{dir}$ . Red lines indicate fits to the function $I = I_0 \sin^2(2(\theta_{dir} - \theta_{pol})) + B$ , where $I_0$ is the difference in maximum and minimum intensity, and $B$ is the minimum intensity value. For (a), $\theta_{dir} = 42.3^\circ$ , and (b), $\theta_{dir} = 30.15^\circ$ . . . . .	120

4.12 (a) Relative in-plane director magnitude,  $I_0$ . Indications of defects at the edges of posts are shown as small dark spots. (b) In-plane director orientation (red lines) plotted over grayscale image of in-plane director magnitude  $I_0$ . For the sake of clarity, only every 10th pixel is represented in this image. . . . . 121

4.13 Micropost arrays filled with nematic DSCG (14% wt/wt) at room temperature. Crossed-polarizer (a & c) and crossed-polarizer with full wave retardation plate (b & d) images shown with bottom surfaces rubbed along a lattice diagonal (a & b) or a post lattice direction (c & d), as illustrated in the insets. Scale bar = 50  $\mu\text{m}$ . The slow axis of the retardation plate is given by the orange arrow in (b & d). . . 125

4.14 Average in-plane director orientation (red lines) from a minimization of the LdG free energy for a generic nematic in cylindrical micropost confinement, overlaid by the schlieren texture expected when viewed between crossed-polarizers. . . 126

4.15 Nematic films of 14% wt/wt DSCG (a-c) and 30% wt/wt SSY (d-f) in micropost arrays. Images show schlieren textures under crossed-polarizers (a & d), average in-plane director magnitude (b & e), and average in-plane director orientation for a selected region of 4 posts (c & f). Scale bar = 20  $\mu\text{m}$ . . . . . 127

4.16 Results of LdG numerical modeling with varying planar oriented anchoring strength along the bottom of the cell. The planar anchoring is parallel to one of the lattice axes (in this case along the  $x$  direction) and has a strength  $W$ . a) Absolute value of the angle of the stable defect orientation with respect to the bottom surface anchoring direction  $|\phi_d|$ , as a function of anchoring strength  $W$ . Each point is averaged over 10 random initial configurations.  $W_{max} = 1.0 \times 10^{-7} \text{ J/m}^2$  is set at the value of  $W$  resulting in  $|\phi_d| = \phi_{min} = 40.5^\circ$ . Bottom: simulation results for local director orientation (red lines) and corresponding schlieren textures given polarizer, analyzer, lattice axes and rubbing direction (dashed lines / red arrow) given in schematic (e) for (b)  $W_1 = 3.52 \times 10^{-10} \text{ J/m}^2$ , (c)  $W_2 = 7.04 \times 10^{-7} \text{ J/m}^2$  and (d)  $W_3 = 3.48 \times 10^{-6} \text{ J/m}^2$ . . . . . 130

4.17 Columnar film of DSCG dried from a nematic DSCG film of initial concentration 17% wt/wt. Images show (a) crossed-polarizer image of the film; (b) bright field image of the film (where defects are visible as dark lines); (c) probability distribution of in-plane director orientations with respect to the horizontal post lattice spacing direction; (d) average in-plane director orientation for four posts, colored by angle using the same scheme as (c) and plotted over the average in-plane director magnitude (bright=in-plane, dark=out-of-plane/disordered). Scale bar = 10  $\mu\text{m}$ . . . . . 132

4.18 Columnar films dried from (left) nematic DSCG film of initial concentration 18% wt/wt and (right) SSY. Images show (a) crossed-polarizer image of the film; (b) bright field image of the film (where defects are visible as dark lines); (c) probability distribution of in-plane director orientations with respect to the horizontal post lattice spacing direction; (d) average in-plane director orientation for four posts, colored by angle using the same scheme as (c) and plotted over the average in-plane director magnitude (bright=in-plane, dark=out-of-plane/disordered). Scale bar = 10  $\mu\text{m}$ . . . . . 133

4.19 Average in-plane director orientations from expanded LdG free energy minimizations in micropillar confinement for effective Frank elastic constant ratios  $K_3/K_1 = 0.09$  (a-c) and  $K_3/K_1 = 0.03$  (d-f) for in-plane director initializations of  $45^\circ$  (a & d),  $40^\circ$  (b & e), and  $30^\circ$  (c & f) from the horizontal post lattice spacing direction. Line coloring highlights distinct regimes of director orientation (blue = close to horizontal, red = most off-horizontal, green = intermediate orientation); darker backgrounds indicate regions with the 40% greatest contribution to Frank free energy bend,  $b = ((\mathbf{n} \cdot \nabla)\mathbf{n})^2$ . . . . . 135

4.20	Final mean director orientation from expanded LdG free energy minimizations as a function of deviation of initialized director angle from the lattice diagonal. Mean director angles $> 36^\circ$ correspond to “square” defect wall configurations (blue area of graph); mean director angles $< 36^\circ$ correspond to “zigzag” defect wall configurations (mauve area of graph). Filled circles represent effective Frank free energy constants $K_3/K_1 = 0.09$ ; open squares represent effective Frank free energy constants $K_3/K_1 = 0.03$ . . . . .	136
5.1	Illustration of LCLC film configuration with deformed nematic interfaces. Since the film is in nematic-isotropic coexistence, though the top of the aqueous film is level, the isotropic-nematic interface wets the microposts and deforms. . . . .	140
5.2	Cross-polarizing images of a nematic SSY film (polarizer and analyzer vertical and horizontal, respectively) with a deformed interface. Insets: Enlargements of cross-polarizer texture between four posts. . . . .	141
5.3	(Right) Cross-polarizer image of the “pinwheel” texture with corresponding approximated average in-plane director orientation sketched in red dotted lines. (Left) Illustration of the presumed shape of the deformed nematic-isotropic interface between four posts. Dark lines trace the surface of the interface. . . . .	142
5.4	(Top) Nematic DSCG in a microcapillary with inner diameter $< 10\mu\text{m}$ under cross polarizers. (Bottom) Nematic DSCG with added PEG in a microcapillary with inner diameter $< 10\mu\text{m}$ under cross polarizers with a full wavelength retardation plate. . . . .	144

5.5	DSCG emulsion droplets at 15 % wt/wt suspended in mineral oil in glass microcapillaries, under cross-polarizers (top) and with a full-wavelength retardation plate (bottom). . . . .	145
5.6	Isotropic-nematic coexistence of DSCG in a microcapillary, under cross-polarizers with a full wavelength retardation plate. . . . .	146
5.7	Twisted disclination lines observed in nematic DSCG filled capillaries, several days after filling. Viewed under cross-polarizer with full wavelength retarding waveplate. . . . .	147
5.8	Cross-polarizing images of 15% wt/wt SDS/butanol mixture in 10% wt/wt aqueous DSCG solution. The system exhibits nematic-isotropic and/or columnar-isotropic coexistence via crowding effects. . . . .	149
5.9	Variety of SDS/decanol/water mesophases including 3% wt/wt DSCG (top, cross-polarizer, bottom, cross-polarizer with full-wavelength retarding waveplate). Left: SDS/decanol in nematic calamitic ( $N_C$ ) phase (5% decanol, 33.5% SDS). Middle: SDS/decanol in nematic discotic ( $N_D$ ) phase (5.9% decanol, 31% SDS)/ Right: SDS/decanol in lamellar ( $L_\alpha$ ) phase (9.4% decanol, 29.2% SDS). . . . .	150
5.10	Cross-polarizing images of PEO-PBD vesicle in nematic DSCG shortly after initial suspension. Top: Temperature increase from 25C to 36C (left to right) induces swelling of crumpled vesicle. Bottom: Cooling from 36C to 25C (left to right) causes vesicle to deswell and crumple. . . . .	151

5.11 Vesicles in nematic DSCG 3 days after initial cooling, under cross-polarizers.  
Image at the far right demonstrates deformation of vesicle shape by a moving  
isotropic-nematic interface. . . . . 152

# Chapter 1

## Introduction

The creation of unique materials through the careful control of microstructure is an exciting new activity at the forefront of condensed matter physics. Microstructured photonic metamaterials, for example, exploit micron-size refractive patterns to create substances with unusual optical properties, e.g., superlenses which defeat the conventional diffraction limit. Biomimetic materials replicate micro-textures observed in the natural world, for example, in order to synthetically reproduce the hydrophobicity of lotus leaves, the adhesive feet of geckos, and the brilliant structural colors of butterfly wings. Such materials have exciting emerging applications in robotics, display, and energy technologies.

The implementation of such sophisticated concepts and technologies requires detailed control of materials at a micro- and nano-scale. Fabrication of two- and three-dimensional (2D, 3D) microstructures, for example, has been facilitated by the refinement of techniques such as photolithography and high-resolution 3D printing. Similarly, recent strides have been made towards creation of self-assembling colloidal microstructures [40, 103], which could eventually

lead to more scalable methods for microstructure production. An attractive and possibly simpler approach towards the same goal is to grow complex material structures starting with surface templates or micro-patterns. In principle, these micro-patterns could be modulated which, in turn, could manipulate structure of the coupled three-dimensional material.

The study of microstructured materials has been stimulated not only by our increased ability to *create* microstructures, but also by the growing portfolio of innovative methodologies to quantitatively *observe* these structures. In particular, digital recording technology and computer processing power have evolved dramatically over the past few decades and have made it possible to precisely quantify and analyze the microscopic structure and dynamics of soft materials via video microscopy [26]. Precise quantification of particle trajectories, for example, has facilitated the technique of microrheology [17] and the measurement and study of vibrational modes [18, 43, 54, 72]. These techniques, in turn, have brought deeper understanding of the microscopic origins of the glass transition [18, 43, 72], melting [1, 51], and other interesting materials physics.

This dissertation investigates the behavior of a variety of soft materials. The research involves fabrication of novel microstructures and then rigorous measurement and analysis of their configurations and dynamics. For example, by creating helical packings of thermal colloidal spheres in hollow cylindrical micro-capillaries, we gained fresh insight into the structural stability and melting physics of quasi-1D helical materials [94]. In a different vein, we investigated a largely unexplored area of the colloidal “phase diagram,” wherein a so-called attractive glass can cross over to become a gel; the experiments developed a novel method for creating

and manipulating colloidal monolayers, and then used the resulting packings to identify vibrational (and microstructural) signatures of the gel-glass transition. Finally, we investigated the substrate-induced self-assembly of a relatively unexplored class of soft materials called lyotropic chromonic liquid crystals (LCLCs). We made significant progress using micropost arrays to template LCLC films with microstructures that affected the LCLCs via the materials' elastic properties [95]. Besides the work discussed in this thesis, the author played a *contributing* role on several other projects in the Yodh lab. These experiments were concerned with the evaporative deposition of colloidal particles, and particularly how capillary interactions between anisotropic microscopic particles can modify their deposition behavior during drying [175–177].

The remainder of this chapter will provide a brief introduction to the primary topics explored in this dissertation. Though the projects described address different fundamental physical problems (melting and structure in confinement, glass-gel “phase behavior”, and templated liquid crystal structures), all of these experiments share state-of-the-art experimental techniques and analysis to understand soft matter phenomenology and phase transitions.

## **1.1 Structure and Melting of Helical Packings**

Helical packings arise from a fairly simple geometrical constraint. When uniform spheres are confined at high densities to the interior of a cylinder whose diameter is of the same order as the sphere diameter, they then form an ordered packing of intertwining helices of adjacent particles. The structure of these packings resembles a two-dimensional hexagonal lattice wrapped into a tight cylinder. Though such structures can be produced at any size, only during the past decade have researchers been able to create such helical packings on the micro- [66, 92, 109, 161] and

nano-scale [75, 171], wherein thermal fluctuations become important.



Figure 1.1: Helical packings of spheres. (Left) Packings of balloons at festivals with  $(0,4,4)$  and  $(0,3,3)$  structures. (Middle right) Spherical candies arranged in a  $(0,6,6)$  structure in their cylindrical packaging. (Right) Fluorescence confocal microscopy image of a  $(2,3,5)$  packing of thermosensitive, micron-size pNIPAm particles in a glass microcapillary.

Thus, the stability of such structures in the presence thermal fluctuations was largely unconsidered until recently, with most research being content to study athermal varieties of such systems [9, 10, 53, 132, 133]. Further, since there exists a widely held assumption that stable crystalline packings with long-range order cannot exist in one dimensional systems [126, 162], it is reasonable to suspect that helical packings might not be stable. In practice, the helical microstructures we explore experimentally (and indeed many analogous structures) are not truly one-dimensional; rather, they resemble a tightly wrapped periodic two-dimensional pattern. Thus, the exact helical microstructures that thermal colloids form under confinement, their stability, and their phase behavior are not intuitively apparent.

**Chapter 2** of this thesis describes work identifying helical colloidal packings at the microscale and examining the thermal stability of such structures. The colloids employed are packings of fluorescently-labeled thermoresponsive microgel spheres in glass microcapillaries. By imaging this system with fluorescence confocal microscopy (a non-trivial task, due to the

highly curved and index-mismatched interfaces of these samples), we quantified both the structural properties and their Brownian dynamics at multiple particle-to-tube-diameter ratios, and as a function of the particle volume fraction. We observed that this system forms helical packings, and that these packings remained stable in the presence of thermal fluctuations at volume fractions significantly below close packing. Then, by decreasing the particle diameter (i.e., by increasing the sample temperature), and thus decreasing the overall volume fraction, we were able to observe the melting of these helical crystals. Careful examination of the dynamics and fluctuations of local order parameters around the melting transitions provided evidence of a phase-transition-like crossover between long-range orientationally ordered and fluid states. To some degree, these observations provide a counterexample to the widely accepted idea that one cannot observe stable phases in one dimension (e.g., in the limit of infinitely long samples). Though translational order in such packings should still not be stable, we observe evidence of stable orientationally ordered phases, and further, we observe transitions from one phase to another. We used orientational order parameters to locally identify helices of different pitch and to discover how helical structures can transform between different local pitches and chiralities prior to melting in a manner inconsistent with well-understood dislocation-mediated structural transitions of athermal packings. This work has been published [94]. In **Chapter 2** we discuss the background, experimental challenges, results and analysis with greater depth than we have presented in [94].

## 1.2 Vibrational Signatures of Gel-like and Glassy Colloidal Packings

The relationship between the microscopic structure and macroscopic properties of a solid is an exciting issue in the current study of disordered materials [4, 29, 36, 62, 142]. For example, regions prone to mechanical failure are difficult to identify from structure alone in amorphous solids, though they are readily apparent in crystalline solids as micro-structural defects and grain boundaries [1]. Nevertheless, subtle structural signatures can be helpful for characterizing the behavior of disordered materials. In fact, recent studies in disordered dense colloidal packings have made progress identifying signs of structural order at the onset of the glass transition [152, 187], and identifying rearrangement-prone “soft spots” in glassy packings from quasi-localized low-frequency vibrational modes [12, 13, 19, 42, 101, 165] and regions with smaller-than-average local bond coordination [174].

Packings of particles with short-ranged attraction are typically described by two kinds of dynamically arrested states [160, 181, 182]. The term “attractive glass” is used to denote a dense packing of particles with uniform structure, while the term “gel” is used to describe a broad class of sparse dynamically arrested packings. Despite such fundamentally different qualitative descriptions, gels and attractive glasses are difficult to distinguish in systems with strong inter-particle attractions and intermediate densities. Typically, gels are qualitatively distinguished from glasses by obvious structural inhomogeneities, a task made very difficult in *nearly* uniform packings. Additionally, gels share some dynamical traits of glassy materials, such as dynamical heterogeneity [24], and a prevalence of low-frequency vibrational modes compared to ordered solids [139]. Some recent studies have characterized this transition through the observation of

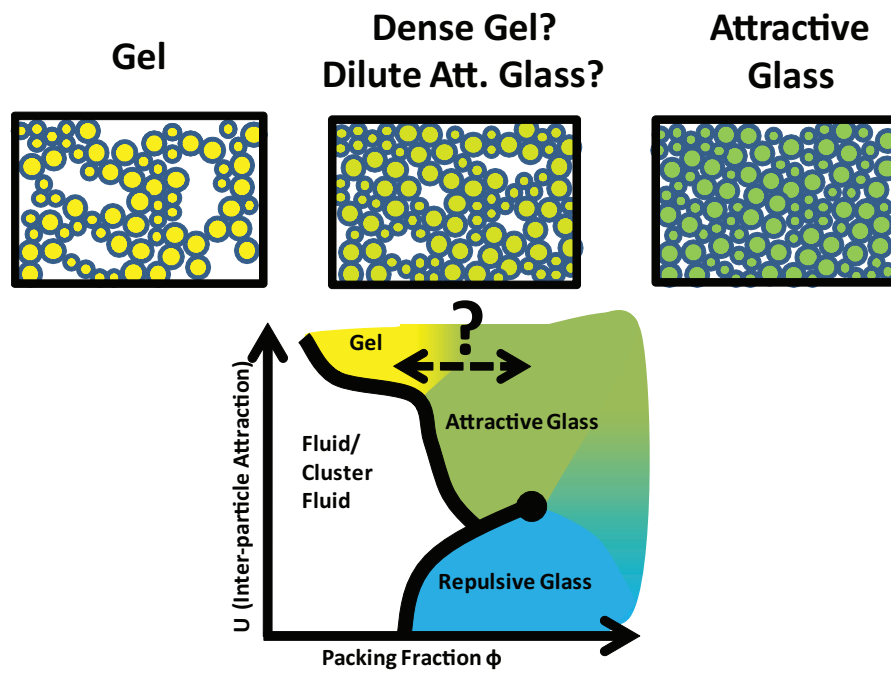


Figure 1.2: Qualitative phase diagram of disordered packings as a function of packing fraction ( $\phi$ ) and inter-particle attraction ( $U$ ). Images above illustrate an obviously sparse gel packing (left), obviously dense glassy packing (right), and an intermediate density packing of indeterminate phase (middle).

two-step rheological yielding [86], changes in slow relaxation times [182], scaling of bulk elastic properties [183], and deviation of a phase boundary line from percolation theory [34]. However, there has not yet been a distinct microstructural or localized dynamical signature of the gel-to-glass crossover in a static experimental sample (i.e., a sample of thermal particles which is dynamically arrested and not experiencing external shear) with strong inter-particle attractions.

**Chapter 3** examines the crossover from glassy to gel-like dynamics and structure in quasi-2D colloidal packings with short-ranged attraction. We create monolayers of bidisperse micron-sized polystyrene colloids by exploiting a novel spreading behavior of binary water-lutidine mixtures refined through careful experimentation. Using this method, we can track vibrations in even the densest, most uniform glassy packings. Starting from these particle trajectories, we apply a well-implemented method for calculating the vibrational density of states (vDOS) [18, 43, 54, 72] for the first time in spatially heterogeneous, attractive colloidal packings. The shape of the resulting vDOS curves demonstrates a distinctive crossover from typically glassy behavior at high area-fractions to curves demonstrating an excess of low-frequency vibrational modes below a certain density threshold. The shape of the characteristically “gel-like” curves is attributed to the appearance of low-frequency phonon modes localized to individual/small clusters of low-coordination particles. Though the exact structures surrounding these individual particles are not always the same, this vibrational behavior helps us to elucidate the microstructural origin of the differences between attractive glasses and gels. This work is complete, and we are in the process of submitting it for publication.

### 1.3 Microscopic Ordering of Lyotropic Chromonic Liquid Crystals

While liquid crystals (LCs) have been extensively utilized in display technologies for the past several decades, scientists and engineers are now turning to new implementations of this broad class of materials for photonic, mechanical, and sensory applications. Many of these applications require a sophisticated control of liquid crystalline order at the microscopic scale. For example, recent mechanisms have been proposed that employ emulsion droplets of thermotropic LC's as highly sensitive sensors for endotoxins [93]. Further, recent theoretical studies have proposed that films carefully assembled from tiles with liquid crystalline order and mechanical anisotropy could form self-folding materials [107, 108]. Micropatterned polarizing materials from liquid crystals are also crucial to the development of new holographic display technologies [102, 151].

Lyotropic chromonic liquid crystals (LCLCs) are a relatively unexplored class of anisotropic fluids conducive to microscale self-assembly [98, 99, 150]. LCLCs are typically composed of molecular aggregates of plank-like polyaromatic compounds with ionic side-groups in an aqueous suspension. As the concentration of such a suspension increases, the density and average length of these aggregates increases, eventually forming a nematic (N) and then a columnar (M) phase. These mesophases are thus significantly different from more commonly utilized thermotropic and amphiphilic lyotropic liquid crystals.

Because of their aqueous nature, low toxicity, and low cost, LCLCs are promising for utilization in a variety of applications. Micropatterned films of LCLCs, specifically, have a wide variety of emerging applications distinct from other types of liquid crystals, including inexpensive polarizing films [32, 98, 99], holographic displays [102, 151], organic electronics and

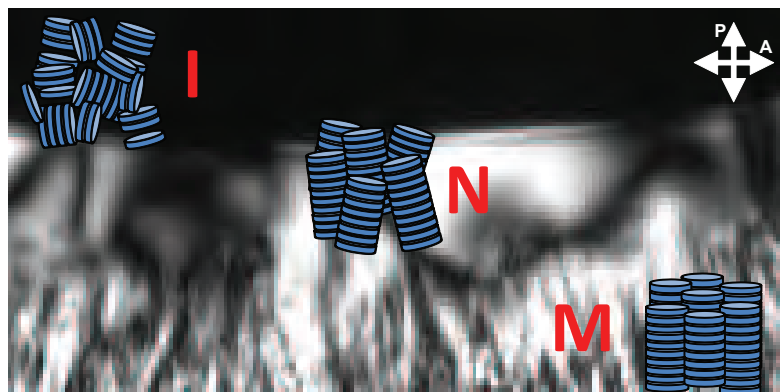


Figure 1.3: Cross-polarizing image of a drying droplet of a dilute DSCG suspension, showing a low-to-high concentration gradient from image top to bottom. Illustrations depict molecular structure in corresponding isotropic (I, top), nematic (N, middle) and columnar (M, bottom) regions.

solar cells [115, 119], biosensors [144, 168], aqueous colloidal, nanotube and bacterial assembly [38, 113, 120, 146, 188], and precursors to structured graphene-based materials [49, 110]. LCLCs also offer useful attributes for fundamental investigation of the effects of elasticity on self-assembly behavior, since their elastic properties can be tuned via control of mesogen concentration [189], depletants, and ions [121]. Indeed, studies have demonstrated that LCLCs in micro-scale confinement form unique, elastic-property-dependent configurations [64, 158].

In this thesis, we describe the manipulation of aqueous LCLC suspensions in an effort to observe novel finely tunable microstructure assemblies. **Chapter 4** reviews and elaborates on our published work examining the assembly of microstructure in LCLC films templated by cylindrical micropost arrays [95]. A fundamental understanding of the detailed microstructure in these films is enabled by a novel method for high-resolution director field determination that combines polarizing microscopy, video microscopy and particle tracking techniques. This work is also facilitated by numerical free energy solutions for a liquid crystal under micropost confinement. The presence of a square lattice of cylindrical microposts is discovered to create a significant

alignment/anchoring effect on nematic films, biasing a bistable alignment along lattice diagonals. Drying the film to the columnar state results in two classes of defect wall “tile” patterns, i.e., depending on the type and initial concentration of the LCLC used. By pushing numerical models for nematic LCLC’s to a columnar limit, and comparing our results with known characteristics of nematic LCLC suspensions, it is shown that the difference in columnar patterns arises from a competition of bend and splay elastic deformations as the nematic approaches the columnar phase. A new method for templating microstructure in liquid crystal films by modulating their elastic properties is thus discovered.

**Chapter 5** describes additional preliminary work exploring novel LCLC configurations. It was hoped that LCLCs may assemble into unique and useful configurations by placing them in new microscale confinement geometries, as well as observing how they interact with ordered amphiphile structures. Indeed, both thin nematic LCLC films, with varying thickness and LCLCs, confined to narrow cylinders, appear to demonstrate novel twisted configurations due to coupling between nematic elastic deformations and confining surfaces. Additionally, dense surfactant-based lyotropic LCs were observed to drive LCLC-forming molecules into columnar structures which co-organize with the surrounding LC structure, and self-assembled diblock copolymer vesicles were observed to deform in novel ways when suspended in nematic LCLCs. These results are not yet published, but they should serve as starting points for new and exciting studies with novel LCLC assemblies.

## 1.4 Organization of Thesis

This remainder of this thesis is organized into several chapters, each elaborating on the context, theory, experimental details, and the results of the separate studies discussed above. **Chapter 2** describes work on helical packings of thermoresponsive colloidal spheres in glass capillaries which has been published [94]. **Chapter 3** describes a study of the vibrational modes of quasi-two dimensional attractive packings of colloidal spheres; this study is currently being written and submitted for publication. **Chapter 4** describes published work on elasticity-dependent configurations of LCLC films in micropost arrays [95]. Additionally, the results of preliminary (but unpublished) experiments on novel microstructured chromonic liquid crystal systems are briefly summarized in **Chapter 5**; though unpublished, these experiments should nucleate future work. Finally, **Chapter 6** summarizes the results presented in previous chapters and elaborates on directions for future study.

## **Chapter 2**

# **Helical Packings and Phase**

# **Transformations of Soft Spheres in**

# **Cylinders**

### **2.1 Introduction**

“Crystalline” or “ordered” materials are composed of particles with even, periodic spacing over large length scales. Long-range translational order is a common signature of stable solid phases of matter, whether in ordered packings of the atoms in metals or colloidal spheres packed in a FCC or BCC lattice. Such phases are common in three-dimensions (3D), though the physics of lower dimensionality materials can diminish such order. Crystalline packings in two-dimensions

(2D), for example, only display quasi-long-range translational order, and the uniformity of particle spacings decays algebraically over long distances [85, 117, 173]. One-dimensional materials are prohibited from exhibiting translationally ordered phases, as there exists no significant free energy barrier between translationally ordered and disordered phases [162], and ordered phases themselves are unstable to fluctuations [126]. These concepts imply that ordered one-dimensional materials are not stable, which would suggest the formation of crystalline nanowires are problematic at best.

Order, however, is not necessarily restricted to the uniform spacing of particles as defined by *translational* order. Orientational order, based on the local arrangements of particles rather than their spacing, does not follow the same dimensional restrictions as translational order. For example, two-dimensional crystals exhibit truly long-range orientational order, and proposed two-dimensional phases with no translational order still exhibit quasi-long-range orientational order [85, 117, 173]. Additionally, both quasi-crystals and liquid crystals are structured, stable phases of matter which exhibit orientational order without regular spacings of constituent particles. Thus, a quasi-one dimensional (1D) material which exhibits some degree of orientational order might demonstrate phases that are stable against thermal fluctuations.

To this end, packings of soft colloidal spheres in cylinders provide a fascinating and useful model experimental system to quantitatively investigate order and phase transformations in quasi-1D. At high densities, spheres in cylindrical confinement form helical crystalline structures [37, 53]. Such packings are observed in foams [9, 10, 132, 133], biological microstructures [37], colloids in micro-channels [66, 92, 109, 161] and fullerenes in nanotubes [75, 171].

Simulations suggest that transitions between different helical ordered states [84, 131] and between quasi-1D ordered and disordered states [33, 46, 61] should exist in thermal systems, but such transitions have not been investigated experimentally. To date, research on this system class has been limited to static snapshots and athermal media.

In this chapter, we explore ordered and disordered structures in a quasi-1D thermal system of soft particles with adjustable diameter and volume fraction. In particular, we create helical packings of thermoresponsive particles in glass microcapillaries. We show theoretically that phases with long-range orientational order can exist in quasi-1D, and we demonstrate experimentally that such phases with long-range orientational order exist at volume fractions below maximal packing. Then, we study volume-fraction induced melting of these orientationally ordered phases into liquid phases. The orientational order parameters and susceptibilities that characterize these phases and the crossover between phases are measured and analyzed. Coexisting regions of ordered and disordered states and coexisting ordered domains with different pitch and chirality are observed. Such coexistence effects suggest the presence of abrupt or discontinuous volume-fraction driven transitions between the quasi-1D helical structures. Interestingly, these orientationally ordered phases in quasi-1D share physical features with orientationally ordered phases observed [51, 112, 184] and predicted [85, 117, 173] in 2D.

## **2.2 Contextual and Theoretical Background**

### **2.2.1 Helical Packing Structures**

From the placement of atoms in the alpha helix of a protein molecule, to the placement of leaves on the stem of a flower, to the pillars of balloons festooning a graduation ceremony,

helices of discrete particles are common to find among quasi-linear structures of all sizes. In the soft matter community, recent work has observed formation of helical structures via self-assembly of micro- and nano-scale chiral filaments of bent-core molecules [60], and dipolar Janus particles [56]. Despite the complicated self-assembled nature of such systems, complex inter-particle interactions need not be required to form helical structures.

In fact, such helical structures are readily formed by isotropic particles confined to the surface or interior of similarly sized cylinders. These structures have been found in experiments with granular materials [53], foams [9, 10, 132, 133], colloidal suspensions [66, 92, 109, 161] and carbon fullerenes [75, 171], as well as in computer simulations [33, 46, 61, 84, 131, 167]. When isotropic particles are packed into such a geometry, the resulting placement of particles at the surface resembles a two-dimensional hexagonal or rhombic packing of circles on a plane wrapped onto a cylinder (Fig. 2.1). The pitch of these structures at maximal packing is determined by the ratio of sphere diameter to the diameter of the confining cylinder. For athermal or close packed structures, hexagonal surface packings occur only at discrete ratios of cylinder and sphere diameter, with rhombic structures filling intermediate ratio geometries (Fig. 2.2).

A formal notation for distinguishing these geometries was originally developed to describe phyllotactic structures [37, 53]. Hexagonal surface packings are given a three integer label  $(m, n, m + n)$ , while rhombic packings have a two integer label  $(m, n)$ . These descriptors include detailed information about the topology and geometry of these packings, and can be interpreted in several ways. Most simply, if one looks at a single particle in the packing and labels all other particles in the packing by their relative distance along the cylinder axis direction  $z$ , the descriptor is given by the integers associated with the neighbors of the selected particle

(Fig. 2.1).

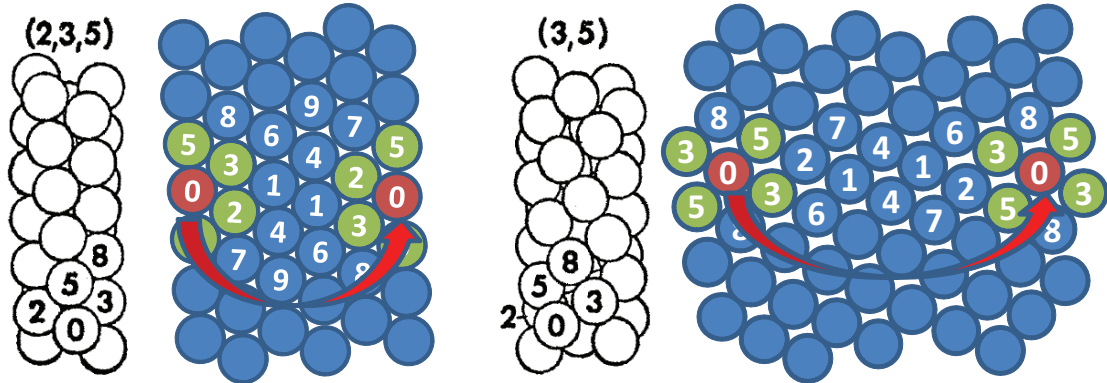


Figure 2.1: Illustrations depicting the two-dimensional order of a hexagonal  $(2, 3, 5)$  structure (left) and a rhombic  $(3, 5)$  structure (right). Illustrations on the left demonstrate the three dimensional structure (adapted from [37]); illustrations on the right demonstrate the corresponding “unwrapped” two-dimensional structure. Particles on the edge are repeated for clarity. Numbers indicate relative distance along the tube direction; arrows indicate the wrapping of the 2D structured needed to create the corresponding 3D structure.

Equivalently, one can consider these descriptors as similar to the vectors used to describe the chirality of carbon nanotubes. As mentioned previously, these helical packings can be seen as a thin slice of a two-dimensional hexagonal (or rhombic) lattice wrapped onto itself into a cylinder. The integers in the descriptor then describe the path traced along two lattice directions to reach the particle that the slice wraps itself upon to form the helical packing.

Information about the packing’s chirality can be inferred from these integer descriptors. Though all packings in these geometries are helices, not all of them are necessarily chiral. Achi-ral packings have descriptors where  $m = 0$  or  $n = 0$ , indicating that a line of particle contacts, or parastichy, runs along the circumference of the confining tube, or  $m = n$ , indicating that, in the hexagonal case, one of the parastiches runs along the  $z$ -axis of the cylinder. Any other packing where  $m \neq n$  has an inherent chirality. Particles with identical topology and opposite chirality are distinguished by different ordering of the first two integers in the descriptors, e.g.

(2,3,5) and (3,2,5).

The integer descriptors also indicate the number of individual particle helices which can be observed in the packing. As stated previously, each integer in this descriptor indicates a particular neighboring particle of any particle in the packing, based on its relative  $z$ -distance. The helical line of adjacent particles connecting particle 0 and particle  $m$  is referred to as the  $m$ -parastichy (in the parlance of phyllotaxis). In a given packing, there will be  $m$  distinct  $m$ -parastichies; as such, the smallest integer in the descriptor gives the minimum number of particle helices which can characterize a packing. For example, in a (1,3,4) packing, a 1-parastichy characterizes the entire packing, while the minimum number of distinct helices in a (2,3,5) packing are two interlacing 2-parastichies.

Though this integer descriptor yields a decent amount of information about these packings, they do not by themselves serve to describe every geometrical quantity. To learn the ratio of particle diameter/separation to cylinder diameter, or the angular pitch of a particular parastichy/helix in the packing, one needs additional information. From the integers described above, one can construct a relationship to describe additional geometrical parameters. For example, following [53], one can relate  $m$  and  $n$  to the divergence angle  $\alpha$  (the relative angle separating neighboring particles in cylindrical coordinates) by the following relation:

$$\frac{(m+n)(n-m)}{m(m+2n)} = \frac{\sin(\frac{1}{2}(m+n)\alpha)\sin(\frac{1}{2}(n-m)\alpha)}{\sin(\frac{1}{2}(m+2n)\alpha)\sin(\frac{1}{2}m\alpha)}. \quad (2.1)$$

Though the above equation is not analytically solvable, numerical solutions of such equations yield well-defined geometrical characteristics for each packing which are consistent with experimental studies.

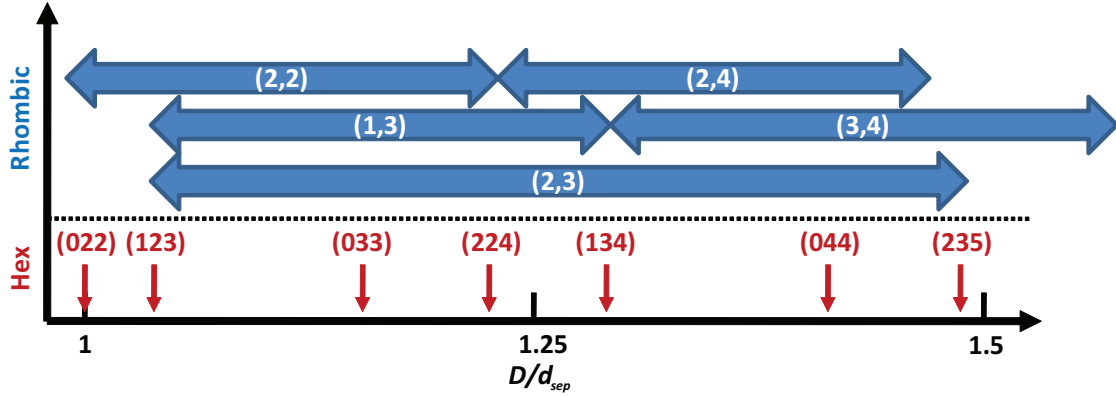


Figure 2.2: Illustration of possible ratios of inter-particle separation  $d_{sep}$  and packing diameter  $D$  (Fig. 2.13) at close packing for hexagonal and rhombic helical configurations (based on data from [37, 53]).

### 2.2.2 Transformations of Helical Structures

Movement of athermal particles in dense packings confined to a cylindrical boundary which is stretched or compressed yields information about how helical packings can change pitch and chirality [53]. Transformations between different helical structures in such systems can occur as continuous deformations mediated through an intermediate rhombic phase, or as discontinuous changes in structure mediated by defects. In either case, the transformations adhere to rules related to the topology of packings.

Continuous transformations between such packings are mediated by deformations of the hexagonal structure through an intermediate rhombic phase. Generally, a  $(m, n, m + n)$  packing can transform to a packing sharing two of the same integers. For example, the  $(2, 3, 5)$  packing depicted in Fig. 2.1 can deform continuously to a  $(3, 5, 8)$  packing through an intermediate rhombic  $(3, 5)$  packing. During this transformation, particles 0 and 3 (along the 3-parastichy) and particles 0 and 5 (along the 5-parastichy) remain in contact. As the contact between the particles labeled 0 and 2 is broken and these pairs move apart, the 0 and 8 particles move closer

together, until they come into contact. During this deformation, the particle packing continuously increases in diameter. In terms of the two-dimensional “unwrapping” of these packings, this deformation can be considered as the continuous stretching of a rhombic packing along the azimuthal direction. Through such deformations, any  $(m, n, m + n)$  packing can transform to a  $(n, m + n, m + 2n)$  through an intermediate rhombic  $(n, m + n)$  packing, or to a  $(n - m, m, n)$  packing through an intermediate rhombic  $(m, n)$  packing.

Discontinuous transformations between helical packings are mediated by the propagation of defects. Consistent with a conceptual understanding of these geometries as wrapped packings of 2D hexagonal lattices, a defect in this system consists of a dislocation, or a pair of particles with 5 and 7 nearest neighbors. A dislocation moving through one of these packings will cause a change in the orientation in the local hexagonal orientation, or equivalently, a change in the packing structure (as depicted in Fig. 2.3). Dislocations can thus mediate a change in a  $(m, n, m + n)$  structure to a  $(m \pm 1, n, m + n \pm 1)$ ,  $(m, n \pm 1, m + n \pm 1)$ , or  $(m \pm 1, n \mp 1, m + n)$  packing.

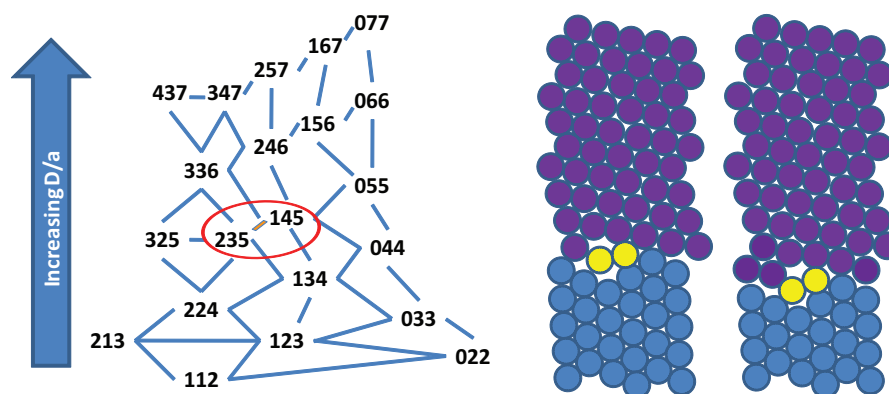


Figure 2.3: (Left) Possible transformations between helical, hexagonally ordered states mediated by dislocation motion (adapted from [53]), arranged by ratio of packing diameter  $D$  to particle radius  $a$  at close packing. (Right) “Unwrapped” structure of a helical packing transitioning between a  $(2, 3, 5)$  (bottom, blue circles) and a  $(1, 4, 5)$  packing (top, purple circles) via motion of a 5-7 dislocation pair (yellow circles).

Though these aforementioned transformations are geometrically intuitive, they may not describe all physical systems. For example, they often necessitate dramatic changes in packing diameter or linear particle density, and they may completely skip over phases which might be more energetically favorable given the confining geometries. Indeed, simulations indicate that transitions in thermal packings of spheres in cylinders are mediated by different mechanisms [61].

### 2.2.3 Phase Transitions

In the study of condensed matter physics, the crossover between states of different degrees of order and symmetry is a fundamental and important field of study. The physics of such crossovers is particularly interesting when the transition between two states exhibits some discontinuity in free energy, often reflected by a discontinuous change in order parameter. Such an occurrence is known as a *phase transition*. Though the term phase transition might be used informally by a layperson to indicate a gradual change in matter, its use in the physics community specifically indicates crossovers exhibiting some discontinuity in free energy or order.

Phase transitions are typically categorized as first or second order. First order phase transitions exhibit a discontinuous jump in free energy/order with temperature as the system moves between phases. Consequently, these transitions are characterized by a latent heat which is absorbed/released by the system. Additionally, an additional hallmark of first order phase transitions is the stable coexistence of phases. A common physical example used to illustrate discontinuous transitions is the phase behavior of water between its vapor and liquid states or its liquid and ice states.

Second order phase transitions, on the other hand, exhibit a continuous change in free energy or order with temperature. However, the *rate of change* in free energy or order parameter with

temperature will change discontinuously at the transition temperature. As there is no latent heat in this type of transition, phase coexistence is not observed. These transitions are characterized by a divergence in the susceptibility of the order parameter at the transition temperature (in first order transitions, the susceptibility of the order parameter jumps discontinuously). A common example of continuous phase transitions is the ferromagnetic transition, as is captured by the 2D Ising model.

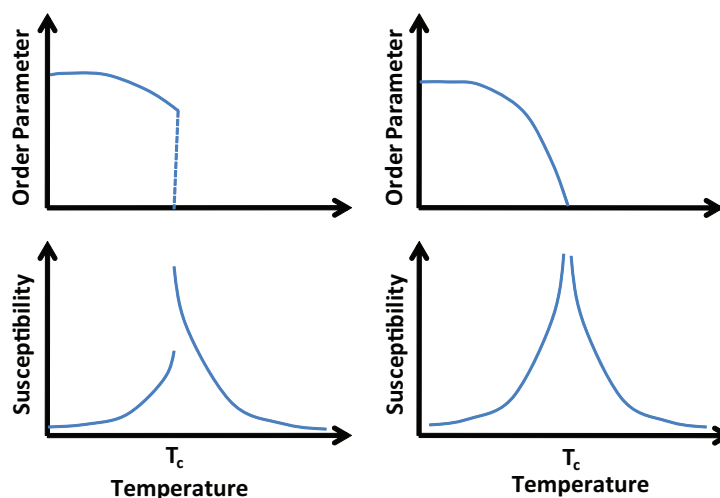


Figure 2.4: Qualitative illustrations of behavior of order parameters and associated susceptibilities with temperature in discontinuous 1st order (left) and continuous 2nd order phase transitions (right).

### 2.2.3.1 Phase Transitions, Long Range Order and Dimensionality

Phase transitions and the stability of long range order are properties of packings closely tied to dimensionality. In three dimensions, it is well known that crystalline particle packings have long-range translational and orientational order. In colloidal systems, evidence of the first-order solid-fluid transition is seen as fluid-solid coexistence in ordered packings [1,3,41,135,136,190].

Phase transitions and long-range order in two-dimensional packings are more complex and

are not entirely understood. There are several proposed mechanisms for melting in two dimensions, including grain-boundary induced melting [21, 81], or geometrical defect condensation [44], but the most widely-cited theory for phase transitions of packings in two dimensions is known as Kosterlitz-Thouless-Halperin-Nelson-Young (KTHNY) theory [85, 117, 173]. In this framework, ordered two dimensional solids experience a two-step melting process. At low temperatures, the two-dimensional crystal phase is stable; this phase has quasi-long-range translational order (which decays algebraically with distance or system size), and long-range orientational order. Then, above some transition temperature  $T_m$ , thermally activated dislocation pairs break into free dislocations, destroying translational order. Interestingly, however, the system still retains quasi-long-range orientational order, and is thus termed the “hexatic” phase. Finally, above a second higher transition temperature  $T_i$ , the free dislocations dissociate into free disclinations, destroying orientational order, and leading to an entirely disordered isotropic fluid phase. These effects were first observed experimentally by [112]. Relatively more recently, the two-step melting processes have been clearly observed in systems of colloidal particles interacting via long-range repulsive dipolar forces [184] and colloidal particle systems with short range repulsive interactions so that the transition is purely mediated by volume-fraction [51], though the exact order of these transitions is not necessarily clear [51].

It is perhaps common knowledge (among condensed matter physicists) that an infinite one-dimensional system of particles does not exhibit a stable translationally ordered phase, nor a true phase transition. Arguments to these effects are typically made by disproving the stability of a long-range ordered phase to thermal fluctuations, or by showing that there cannot be discontinuous change in free energy between ordered and disordered phases.

The most well-known argument against 1D phase transitions comes from the work of van Hove [162]. To paraphrase a critique of this work by [27]: this argument is carried out by treating a 1D system of pair-wise interacting hard-core particles as an eigenvalue problem. After re-writing the system's partition function as a transfer operator, van Hove finds its largest eigenvalue, which turns out to be the only relevant contributor to the free energy of the system. Using functional analysis, van Hove demonstrates that this free energy can be written as an analytic function of temperature. As phase transitions by their very definition need to exhibit some discontinuity in free energy, this effectively disproves the presence of a phase transition in this system.

Another famous argument, originally made by Peierls, indicates that a one-dimensional system can not exhibit stable long-range translational order. Following [125] and [16], we imagine a one-dimensional line of particles spaced evenly, with an inter-particle spacing  $a$ , and we assume a harmonic interaction between particles. In this case, when the  $n$ th particle in the chain deviates from its equilibrium position by  $u_n$ , it will have an increase in energy,  $U$ , defined by

$$U = \frac{1}{2}Ku_n^2. \tag{2.2}$$

Here,  $K$  acts as a stiffness constant defining energy/force relationships to a stretched spring between particles. That is, a particle moved from its equilibrium position by  $u_n$  will experience a restoring force  $f = -Ku_n$ .  $K$  is related to the Young's modulus  $Y$ ; a force  $F$  applied to a such chain of  $N$  particles of length  $L = Na$  will cause a change in length  $\Delta L$ , given by  $F = Y\Delta L/L$ , where  $Y = KL$ . Decomposing these displacements into normal modes of the

periodic array, we can write

$$u_n = \sum_q c_q e^{iqna}. \quad (2.3)$$

Here the  $q$  denote different normal modes of the system;  $q$  is the wavenumber of the wave-like phonon modes for the described periodic chain or particles. Using this expansion, we can evaluate the average squared difference in fluctuations of particles separated by a distance  $na$ . By implementing equipartition theory, and also assuming a chain long enough so that we can make continuum approximations, we find the mean-squared difference in displacements of the first and the  $n$ th particles in the chain, given by

$$\langle (u_n - u_0)^2 \rangle \propto \frac{k_B T}{K} \int \frac{dq}{2\pi} \frac{1}{q^2} \approx \frac{k_B T}{K} na, \quad (2.4)$$

where  $\langle \rangle$  indicates an ensemble average,  $u_0$  is the displacement of the first particle in the chain from its equilibrium position,  $k_B$  is the Boltzmann constant and  $T$  is the temperature of the system. We see from this relationship that mean square fluctuations from equilibrium particle positions will increase proportional to the system length  $Na$ . Thus, long-range periodic translational order will be unstable to fluctuations in a 1D chain of infinite length, i.e., thermal-induced fluctuations in position will eventually exceed the lattice spacing. However, we note that the fluctuations are also directly proportional to temperature and inversely proportional to the effective spring constant between particles. Thus, these fluctuations will not appear significant in a chain with inter-particle interactions very strong compared to the temperature and the system length, that is, where  $K \gg k_B T Na$ . This could explain the apparent stability of periodic structures in quasi-1D materials. For example, in carbon nanotubes, the covalent bonds between

atoms are strong enough so that the length necessary to observe significant fluctuations in atomic spacing is longer than the tubes themselves.

Quasi-1D systems are generally not be “immune” to this argument. For example, in a periodic helix of particles (with the location of particle  $n$  at cylindrical coordinates  $[\mathbf{r}, n\phi_0, nz_0]$ , one could perform a similar calculation for fluctuations in both the vertical position of particle  $n$ ,  $z_n = nz_0$ , and the angular position of particle  $n$ ,  $\phi_n = n\phi_0$ ). In both cases, the integrand in Equation 2.4 would lead to thermal fluctuations which scale with the length of the chain.

However, as is explored in more detail in section 2.4.3, this growth of fluctuations with system size is different for particle packing *orientation* as compared to particle *position*. The robustness of orientational order to fluctuations is due to a coupling of the local orientation of the packing to the positions of the surrounding particles. To put it in more mathematical terms, the local orientation  $\theta$  of a particle packing is proportional to a local gradient in the particle positions; that is,  $\theta \propto \nabla \times u$ . If fluctuations in the local orientation were evaluated using a method similar to the one above (as is done in section 2.4.3), then an extra factor of  $q$  arises in the integrand which (after integration) keeps the fluctuations from diverging with system size. Furthermore, simulations of simple quasi-1D systems with an orientational degree of freedom (i.e., rods, ellipses, needles, or rectangles with centers fixed on a one-dimensional line) not only exhibit long-range orientational order, they imply that a “melted” state *without* long-range orientational order may not exist for this specific system class [50, 70].

As pointed out by [27], arguments against one-dimensional phase transitions and long-range

order also do not apply for quasi-1D systems with more complicated interactions, that is, particles with long-range and cooperative/many-body interactions. For example, in a model described in [80], a zipper of  $N$  links that can only be opened from one end is one dimensional system which has been proven to exhibit a phase transition.

Thus, the most appropriate dimensional perspective for approaching ordered helical packings of colloidal particles in cylinders is not immediately clear. Though the particles are largely confined to one dimension, it cannot be ignored that these packings have some three dimensional structure. Additionally, the structure of the helical packings, as described in Section 2.2.1, resembles a two-dimensional hexagonally packed crystal with a very short periodicity in one dimension.

Finally, the confining cylindrical boundary of these helical packings may also play an important role in influencing local order and phase behavior. For example, the local orientation of particles in a three-dimensional crystal grown on a flat surface would couple to the orientation of said plane. As we discuss in section 2.2.1, the helical pitch (or local packing orientation) of these structures is strongly coupled to their diameter. Confinement of spheres in a cylinder of fixed diameter might then bias the preferred pitch of the packing formed within. The curvature of the confining cylindrical boundary may thus enhance the orientational order of these structures.

Quantification of long-range order and phase behavior in these packings is an important aspect of the experimental work described later in this chapter. Excitingly, it does seem that we have found experimental evidence of both long-range orientational order and for discontinuous phase transition behavior in these helical structures.

## 2.3 Experimental Methods

To study the thermal stability and volume-fraction mediated melting of crystalline helical packings in cylindrical confinement, we employ a novel experimental system of thermoresponsive colloidal particles confined to glass microcapillaries. We faced many unique experimental challenges when assembling, imaging and analyzing this particular system, which are detailed in the following section.

### 2.3.1 pNIPAm microspheres

The colloidal particles used in these experiments are aqueous microgels of poly-N-isopropylacrylamide (pNIPAm). These particles are composed of a sparse crosslinked pNIPAm network; in fact, a given particle's mass is only taken up by approximately 3% polymer. As a result, the particles have soft sphere interactions, deforming under pressure or crowding. This softness makes pNIPAm particles quite useful for creating and then controlling dense packings in tight confinement. In geometries where more commonly used hard-sphere colloidal particles (i.e. polystyrene, polymethylmethacrylate) will easily jam, pNIPAm particles will deform, flow and re-arrange. Additionally, the composition of pNIPAm gives them an index of refraction closely matched to that of water, making them useful for three dimensional imaging applications.

The primary experimental benefit of pNIPAm microspheres compared to other commonly used colloids is their thermo-responsive diameter. The polymer pNIPAm undergoes a temperature induced phase transition in water from being largely hydrophilic to largely hydrophobic at a lower critical solution temperature (LCST) of 32 – 34° C. When crosslinked into a microgel sphere, this results in a swollen, larger-diameter sphere at temperatures below the LCST, and

a collapsed, small-diameter sphere at temperatures above the LCST. Approaching the LCST, the aqueous solvent quality gradually decreases. This effect causes a gradual and predictable deswelling of the particles, leading to a near-linear change in diameter with temperature. This predictable and reversible change in particle diameter has led to these particles becoming widely used in experimental studies of volume-fraction mediated phase behavior [178].

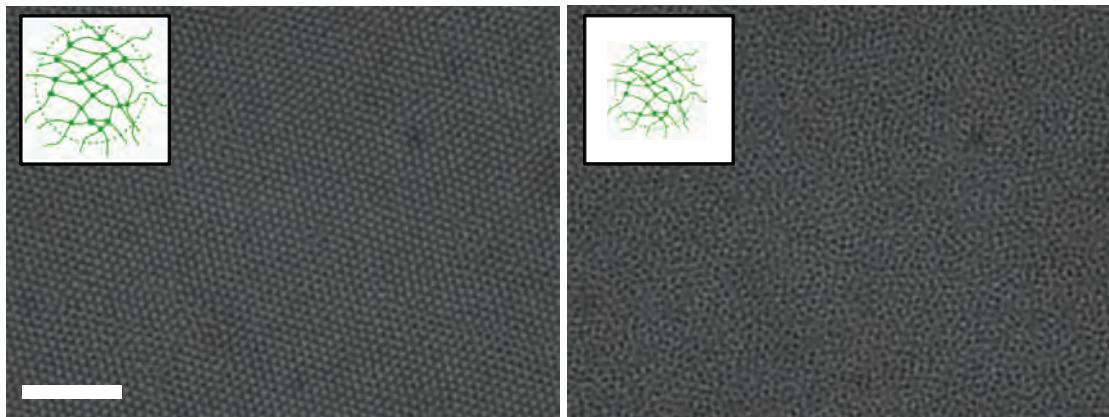


Figure 2.5: Bright field microscopy images of a dense aqueous suspension of pNIPAm microgel particles at 25 °C (left) and 28 °C (right). Particles deswell with increasing temperature (as depicted in the illustration insets), decreasing packing fraction, melting the packing from a crystalline packing (left) to an isotropic disordered fluid (right). Scale bar = 10 $\mu$ m.

### 2.3.1.1 pNIPAm Synthesis and Fluorescent Functionalization

The pNIPAm particles used were synthesized using a surfactant-mediated emulsion polymerization method, which has been well characterized elsewhere [100, 127, 140, 178]. In order to image these particles using fluorescence confocal microscopy, they are functionalized with a fluorophore. Specifically, an additional copolymer, 2-aminoethylmethacrylate hydrochloride (AEMA), is added to the pNIPAm microgels during the synthesis process. This provides the microgels with additional free amine groups, i.e., more than if they were made using NIPAm monomer alone. After synthesis, the particles are swollen in a suspension of a rhodamine-based

fluorescent dye, 5-(6)-carboxytetramethylrhodamine, succinimidyl ester (TAMRA), which covalently bonds to the free amine groups in the microgels. The particles are then thoroughly washed and re-suspended in an aqueous solution.

### 2.3.1.2 pNIPAm Particle Diameter Characterization

Though dynamic light scattering is a prolific and useful technique for characterizing the size of colloidal particles, and it certainly captures the linear changes in particle diameter with temperature expected for pNIPAm particles, light scattering does not yield a particularly useful diameter value for characterizing dense colloidal packings. Dynamic light scattering extracts a hydrodynamic diameter  $d_h$  for particles, derived from the particle diffusion coefficient,  $D$ , which is measured by laser intensity fluctuations scattered through a dilute suspension of particles and defined via the Stokes-Einstein relation:

$$d_h = \frac{k_B T}{3\pi\eta D}. \quad (2.5)$$

Here,  $\eta$  is the fluid viscosity. The resulting hydrodynamic diameter  $d_h$  is typically only 80%-90% of the inter-particle separation observed in close-packed, dynamically arrested packings of pNIPAm spheres. There are multiple reasons for this difference, including the porous nature of the pNIPAm particles, as well as the difficulties in defining a discrete “diameter” for a particle with a soft inter-particle potential.

We derive a more useful “value” of particle diameter from direct microscopic observations of inter-particle interactions. Dilute suspensions of the same pNIPAm particles used in the helical packing experiments were placed between glass coverslips such that the gap between coverslips

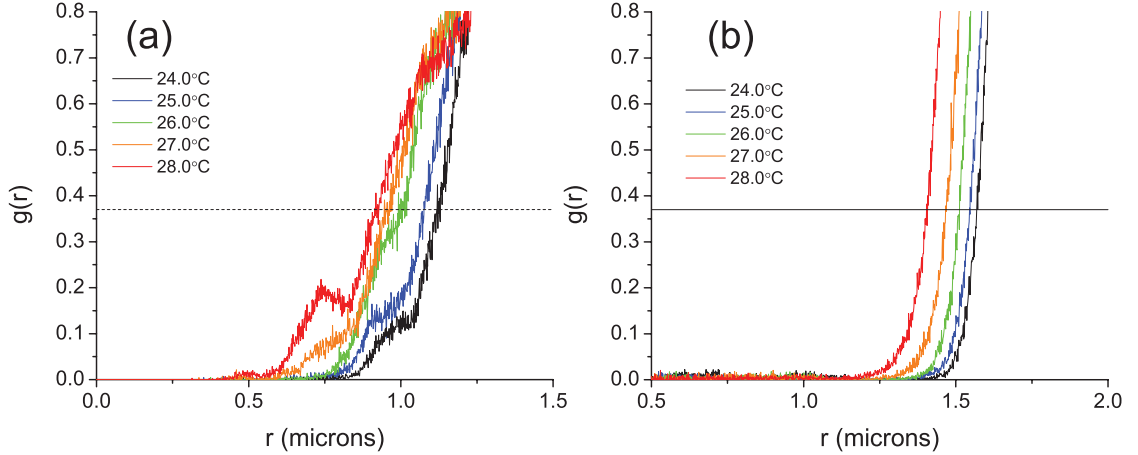


Figure 2.6: Two-dimensional spatial correlation functions for the two sizes of pNIPAM microspheres (a, smaller, b, larger) used in helical packings experiments at different temperatures in a dilute suspension in a quasi-2D cell. Horizontal line indicates  $g(r) = 1/e$ , an effective definition of sphere diameter. Shoulders in  $g(r)$  curves in (a) occur due to the presence of one or two stuck particles in the field-of-view.

was slightly larger than the diameter of the pNIPAM particles, creating a quasi-2d monolayer. Videos of these particles diffusing in two dimensions were taken using a  $100\times$  oil-immersion objective (N.A. = 1.4) at five temperatures from 24 to 28 °C. Particle centers were tracked using standard particle tracking routines [26]. The two dimensional pair correlation function  $g(r)$  of the particle locations was then calculated from the particle tracks. At each temperature, the approximate diameter of the particles taken to be the first value  $r$  where  $g(r) = 1/e$ , since, in the first approximation,  $g(r) = e^{-U(r)/k_B T}$ , and the effective diameter of particles is often taken as the value of  $r$  for which  $U(r) = k_B T$ .

We take a linear fit of these data points to find a functional relationship between effective particle diameter and temperature (shown in Fig. 2.7), since previous studies have observed a linear relationship between diameter and temperature for pNIPAM particles in this temperature range [1, 51, 52, 174, 187]. For the larger species used in this experiment, we find the relationship  $d_{eff} = 2.52\mu\text{m} - 0.037(\mu\text{m}/^\circ\text{C}) \times T$ , and for the smaller species, we find

$$d_{eff} = 2.41\mu\text{m} - 0.054(\mu\text{m}/^\circ\text{C}) \times T.$$

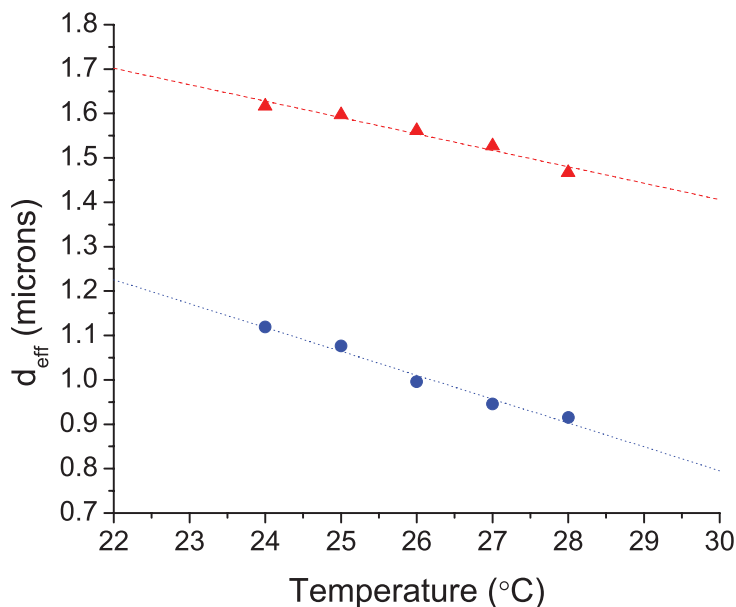


Figure 2.7: Approximate diameters for the smaller (blue ●) and larger (red ▲) pNIPAm particles used in helical packing experiments at different temperatures, with linear fits.

### 2.3.2 Microtube Geometry and Sample Configuration

We create glass microtubes through a multi-step stretching process. We start with borosilicate tubes with outer diameter of 5 mm and inner diameter of 1 mm. We heat and melt this tube over a propane / oxygen flame, remove the tube from the flame, and stretch the glass quickly by hand. This stretching extends a several centimeter-long region to a length of several feet. This thinner tube is then stretched a second time on a micropipette puller (Sutter Instrument Co.). This process creates a final tube with an outer diameter of 20-100  $\mu\text{m}$ , and an inner diameter of one to several  $\mu\text{m}$ . The final inner diameter of the tube depends largely on the fine details of the pulling process. Though micron-sized capillaries can surely be made in an easier manner, this multi-step melting and pulling process serves to clean the inner diameter of the tube

through repeated melting which prevents aggregation of the pNIPAm particles on the walls of the capillary (pNIPAm microgels tend to irreversibly stick to untreated glass surfaces).

A dense suspension of pNIPAm microspheres is then carefully loaded into a glass microcapillary. After a second round of pulling, the ends of each capillary are broken such that the newly pulled area with outer diameter of approximately  $100\ \mu\text{m}$  is left with slightly thicker ends (outer diameter approximately 1 mm). One of these ends is connected to a vacuum pump, while the other end is immersed in a dense suspension of pNIPAm microspheres ( $\phi > 0.3$ ). The vacuum draws in the pNIPAm suspension until the capillary is entirely filled ( $\approx 10$  minutes). After filling, the thick ends of the capillary are broken, and it is placed on a glass microscope slide. It is completely covered with UV-curable epoxy and a large glass coverslip. This seals the ends of the tube, prevents evaporation of the sample, creates a refractive-index matched geometry, and restricts movement of the hair-thin capillary. The temperature of the sample is then cycled from room temperature ( $22 - 25\ ^\circ\text{C}$ ) to  $29\ ^\circ\text{C}$  multiple times over a period of several hours. This permits jammed areas of the microsphere packing to melt and re-form and thereby converge to an equilibrium configuration.

### **2.3.3 Fluorescence Confocal Microscopy**

In the following subsection, we discuss the advantages and drawbacks of several fluorescence confocal microscopy methodologies for acquiring three-dimensional images of the helical colloidal packings.

### **2.3.3.1 Background on Confocal Microscopy**

Confocal microscopy has existed for nearly a half century, though decades of engineering and analysis have yielded many improvements with respect to speed and, to a lesser extent, resolution [111,124]. The distinguishing feature of a confocal microscope is the presence of a pinhole in front of the detector. This pinhole is located at a conjugate focal point, or “confocal” point, of the focal point located in the sample. This pinhole blocks light emitted from an out-of-focus plane, thereby improving the axial resolution of images and blocking background fluorescence. In addition, the existence of the confocal pinhole greatly improves the in-plane (lateral) resolution of the image, making confocal microscopy ideal for a variety of high-resolution scanning techniques.

The original confocal setup used a stage-scanning mechanism to create complete images; the sample was moved to expose its entire volume to a single illumination point. This mechanism not only hindered the speed of scanning, but the rapid motion of the stage can interfere with the sample. Since confocal microscopy techniques are extensively used to image fragile biological samples, most modern commercial confocal systems use techniques which involve scanning the illumination point/apertures, rather than the sample. These can be generally categorized as either spinning disk/tandem scanning confocal microscopes (TSM), or confocal laser-scanning microscopes (CLSM).

Tandem-scanning confocal microscopy was first developed by Egger and Petran in 1967. This technique was based off a variation of an early video-formation technique developed by Paul Nipkow in 1884, the Nipkow disk. This disk contains a series of pinholes distributed at uniform angular and radial spacing; when placed in front of an image, a single rotation of this

disk allows a full scan of the image, converting the original two-dimensional image into a one dimensional series of intensities. The revised Nipkow/Petran disk used in TSM is employed in place of the single confocal aperture in the confocal microscope. Though the confocal image is taken only in discrete points, the spinning of the disk allows a full  $xy$  scan of the image, and the distribution of the pinholes enables multiple points to be imaged in tandem. The development of this scanning technique led to an exponential increase in the scanning speed compared to other confocal microscopes at the time, providing video-rate image sampling (30 frames/sec).

Confocal laser-scanning microscopy (CLSM) is a more recent technology that utilizes a single confocal pinhole (or, in some cases, a slit), but employs mirrors to shift the lateral position of the focused beam within the sample. Though this seems like a more sophisticated technology than TSM, CLSM has both relative advantages and disadvantages compared to spinning-disk microscopies. CLSM is often preferred in biological applications, since it has a much higher lateral and axial resolution than spinning-disk methods due to its use of a single pinhole. In addition, since an entire beam is focused to a single point on a sample, CLSM has much more efficient illumination than TSM. Historically, most CLSM setups provided much slower scans than TSM, but increased innovations have given CLSM setups faster scanning speeds over the past decade or so. However, the increased intensity of the excitation beam can result in dye saturation, which decreases the relative fluorescence of the in-focus plane. In addition, since they require high-quality lasers, CLSM setups typically cost several orders of magnitude more than spinning-disk optical systems (which don't require laser sources, though they are often required for quality fluorescence images).

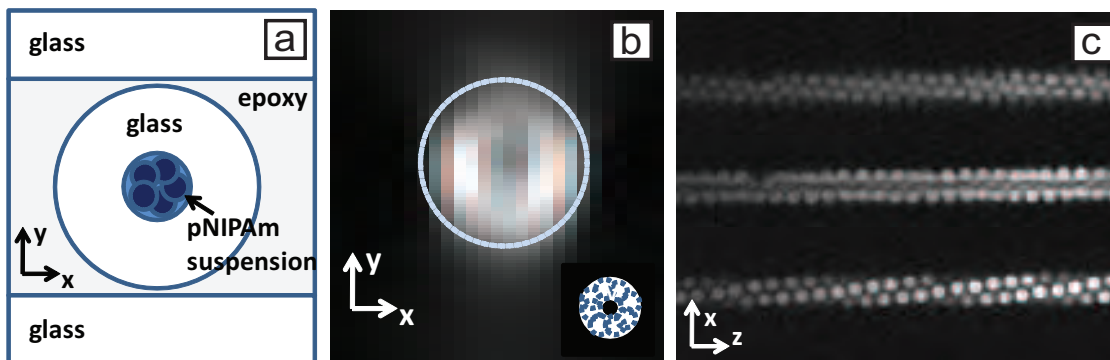


Figure 2.8: Imaging artifacts from confocal scans of helical packings. (a) Illustration of an  $xy$  cross-section of the experimental configuration (not to scale). (b) Brightness of a confocal scan of a (2, 3, 5) packing averaged along the tube length ( $z$  direction) Inset: expected  $xy$  brightness distribution with perfect imaging, given placement of particles in helical packing outlined by dotted lines. (c)  $xz$  slices of a confocal scan of the same (2, 3, 5) packing close to the objective (bottom), at the middle of the packing (middle) and far from the objective (top).

### 2.3.3.2 Advantages and Disadvantages of TSM and CLSM

Though both TSM and CLSM setups were available in our laboratory, our TSM setup (QLC-100, Visitech Int.) provided slightly higher quality images and video compared to our CLSM system (VT-Eye, Visitech Int.) for this particular geometry of microgel packings in cylinders. This difference may seem counterintuitive, considering the increased sophistication and newness of the CLSM system, but there are a few potential explanations. As previously mentioned, the CLSM setup requires higher intensity sample illumination, and it was thus more prone to cause photobleaching in our samples, which was problematic when trying to track particle dynamics in real-time videos that lasted for at least several minutes.

Additionally, aberrations in the three-dimensional structure apparent in all confocal images were amplified in the CLSM scans. Though the microcapillary was immersed in index-matched UV epoxy, the index mismatched, highly curved boundary between the glass tube ( $n = 1.52$ ) and the interior aqueous suspension ( $n = 1.33$ ), as well as a slight index mismatch between

pNIPAm particles and the surrounding aqueous media, caused significant distortions in scans for three-dimensional structure. As mentioned previously, TSM utilizes multiple pinpoints of light passing straight through the sample, while CLSM utilizes a single point, or line of light, coming into the sample at an angle. In an index-matched and/or isotropic geometry, there should not be a difference in these imaging techniques. However, as shown in the imaging of the fluorescent surface of a polystyrene bead in Fig. 2.9 [87], differences in the imaging of curved, index mismatched interfaces are apparent.

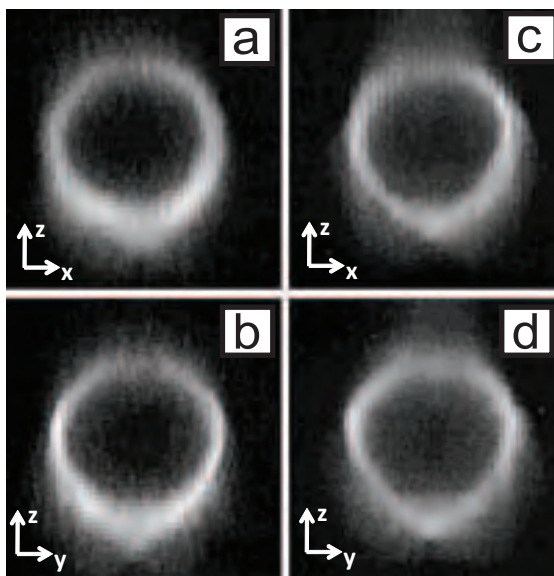


Figure 2.9: Confocal scans of a 6  $\mu\text{m}$  polystyrene bead with a fluorescent shell, comparing TSM (a-b) and CLSM (c-d) scanning methods (taken from [87]). Note the slightly increased deformation from the expected circular shape in the CLSM images.

## 2.4 Results and Analysis

### 2.4.1 Characterization of 3D Structure

At high densities (low temperature), we observe crystalline helical packings with varying pitch and chirality dependent upon particle- and tube-diameter. The observation of large ordered domains is consistent with the tendency for these nearly monodisperse particles to form uniform crystals in 2D [51] and 3D [1].

We analyze the three-dimensional structure of these packings from the particle center locations tracked to subpixel resolution from tandem-scanning/spinning disk confocal fluorescence microscopy scans using common particle tracking routines [26]. There are some imaging aberrations from highly curved, index mismatched interfaces in these samples. One of these aberrations results in a slight stretching of the image in the vertical (scan) direction, which we correct by estimating the extent of the tube packing in the  $y$  direction and then re-scaling it to the extent of the packing image in the  $x$  direction. Tracking using just the routine defined in [26] is not sufficient to locate particle centroids; increasing the contrast and defining a brightness threshold is usually necessary to distinguish between the individual particles in packings this dense. Even with these corrections, due to the inherent difficulties of 3D confocal imaging of index mismatched tubes, some particles furthest from the objective are not detected by this algorithm.

Though the 3D tracking is not completely precise, it does yield sufficient information to identify important structural parameters in these packings. The average inter-particle spacing  $d_{sep}$  is determined from the 3D pair correlation function,  $g(r)$ . Since each structure contains approximately 100 particles, the resolution of this correlation function is fairly poor. Thus, we determine  $d_{sep}$  by fitting a Lorentz peak,  $f(r) = f_0 + A(\omega/(4(r - r_0)^2 + \omega^2))$  to the first peak

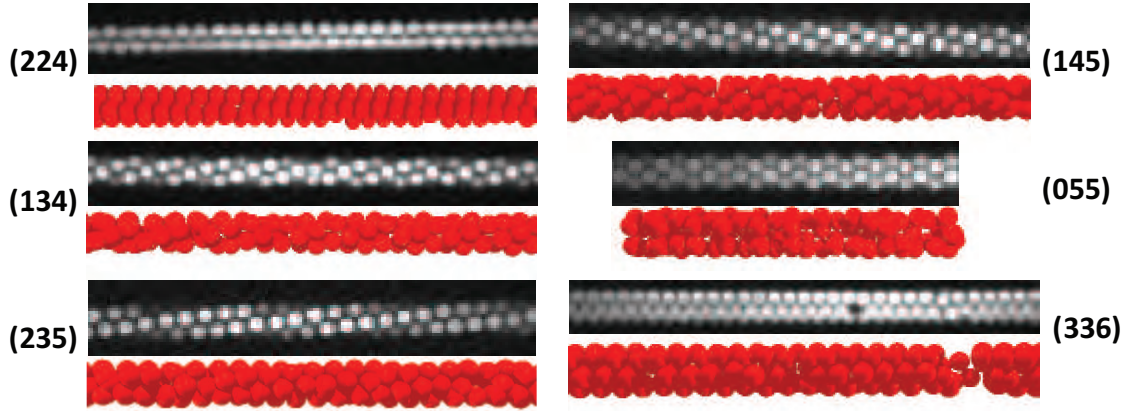


Figure 2.10: Confocal fluorescence cross-sections of six observed geometries of pNIPAm packings in microcapillaries (indicated by  $(m, n, m + n)$  notation), along with corresponding reconstructions from particle locations determined using centroid-locating algorithms on full 3D confocal scans.

in  $g(r)$  (see Fig. 2.11). The center of this function,  $r_0$ , gives us the values for  $d_{sep}$ . The value for structure diameter  $D$  was taken as twice the average value of the radial positions of the particles in the structure in cylindrical coordinates, with the center of the tube given by the average  $x$  and  $y$  positions of the particles. Note, this parameter is not the *tube* inner diameter; the tube diameter  $D_{tube}$  is related to the structure diameter  $D$  and the effective diameter of spheres in the tube  $d_{eff}$  by  $D_{tube} = D + d_{eff}$ . The relationship between  $D$ ,  $d_{sep}$  and  $d_{eff}$  is illustrated in Fig. 2.13.

We use 3D positions of particles to identify packings by the sets of phyllotactic integers  $(m, n, m + n)$  described in Section 2.2.1. As mentioned previously, particles in hard-sphere helical packings predicted for cylinders [5] have six nearest neighbors whose relative order along the tube axis corresponds to a characteristic set of three integers  $(m, n, m + n)$ . The indices indicate the unit vectors in the unwrapped triangular lattice connecting any point to itself in the helical structure. Alternatively, one notices that the three indices indicate the relative distance

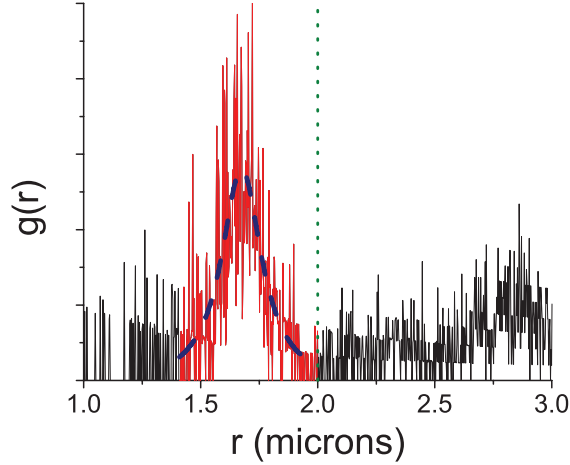


Figure 2.11: 3D pair correlation function from positions of  $\approx 1.7\mu\text{m}$  colloidal pNIPAm spheres in a (2,3,5) packing. First peak in  $g(r)$  highlighted in red, with Lorentzian peak fit used to determine  $d_{sep}$  is the blue dashed line. The vertical dotted line indicates cutoff for nearest neighbor determination.

of a particle’s nearest neighbors along the axis of the cylinder. For example, if any given particle’s nearest neighbors are the second, third or fifth closest particles in the axial direction, it is described as a (2,3,5) packing.

We use this latter definition of the phyllotactic indices to categorize the structures. After identifying particle centers in 3D using common particle tracking routines [26], the nearest neighbors of each particle in an image are identified as those closer than the far end of the first maximum in the 3D pair correlation function  $g(r)$  (see Fig. 2.11). After an individual particle in the packing is selected, all other particles are given integer values based on the order of their axial distance from the selected particle in either direction. The integer values of the nearest neighbors are then recorded. This process is repeated for every particle in the structure. This creates histograms of the relative axial order of the neighboring particles. The peaks in these histograms then identify the integers  $(m, n, m + n)$  describing the ideal packing (Fig. 2.12).

We observe all varieties of predicted helical packings with a tube-diameter-to-particle-spacing

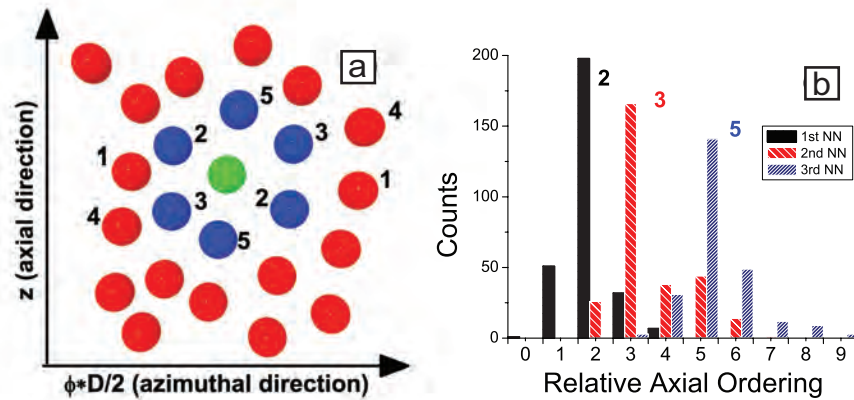


Figure 2.12: Example of determination of helical structural integers  $(m, n, m + n)$ . (a) Axial and azimuthal positions of tracked particles in a short axial section. The nearest neighbors of the green particle are highlighted in blue. Relative axial distance from the green particle listed to side. Note that the nearest neighbors have relative axial order of 2, 3 and 5. (b) Histogram of relative axial order for 1st, 2nd and 3rd closest nearest neighbors in the axial direction in a single packing. Peaks at values of 2, 3 and 5 indicate that this is a (2,3,5) packing.

ratio  $D/d_{sep} < 3$  in 15 samples (Fig. 2.13), with the exception of the structure (0,4,4). The ratio  $D/d_{sep}$  fell within experimental error of the predicted maximally packed hard-sphere values. Granted, the experimental error is fairly large, but this error is mostly due to the artifacts of confocal scanning of an optically distorted sample.

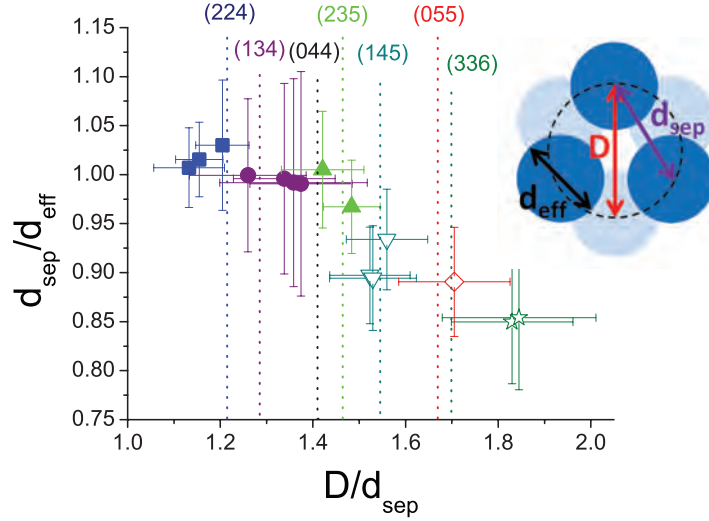


Figure 2.13: Geometrical characteristics of observed structures, (2,2,4) (blue  $\square$ ), (1,3,4) (purple  $\circ$ ), (2,3,5) (green  $\triangle$ ), (1,4,5) (cyan  $\nabla$ ), (0,5,5) (red  $\diamond$ ), (3,3,6) (dark green  $\star$ ). Filled symbols indicate structures with observable Brownian motion. Dashed vertical lines indicate theoretical  $D/d_{sep}$  values for predicted structures. Inset: Cartoon of axial cross-section of a (3,3,6) structure with  $d_{sep} > d_{eff}$ .

Importantly, ordered structures were found to exist over a range of volume fractions below maximal packing. When the effective particle diameter  $d_{eff}$  was such that  $d_{sep}/d_{eff} < 0.95$ , the particles did not appear to move (i.e., motions greater than  $0.2 \mu\text{m}$  were not observed during the 10-second 3D confocal scan). In such cases, we consider the particles to be packed closer than their effective diameters. For  $d_{sep}/d_{eff} > 0.95$ , particles fluctuate significantly about their equilibrium positions. Though helical structures have been observed in many athermal systems (i.e. foams, granular packings, etc), we believe our observations to be the first direct observation

of thermal helical crystalline structures existing at volume fractions below close packing.

### 2.4.2 Long-Range Orientational Order in Achiral Packings

The volume fractions of such samples were lowered further to determine how the packings transform to isotropic states. Two uniformly ordered achiral packings were chosen and are presented here for careful analysis: a (2,2,4) packing of larger microspheres ( $d_{eff} \approx 1.71 \mu\text{m}$  at  $22^\circ\text{C}$ ) and a (0,6,6) packing of smaller microspheres ( $d_{eff} \approx 1.23 \mu\text{m}$  at  $22^\circ\text{C}$ ). The sample temperature was increased in steps of  $0.2 - 0.7^\circ\text{C}$ . At each temperature step, after allotting ample time for the sample to reach thermal equilibrium (e.g., at least 5 minutes), videos of two-dimensional cross-sections of the packings were taken at 15 - 30 frames per second for approximately 5 minutes. Though these two-dimensional videos lose some of the structural information available in three dimensional scans, they provide data at much higher speeds and yield better axial position tracking of particles in view.

A local orientational order parameter,  $\psi_{6j} = \sum_k^{N_{nn}} e^{6i\theta_{jk}} / N_{nn}$ , quantifies helical order in these systems. Here,  $\theta_{jk}$  is the angle between the axis of the tube and the bond between particles  $j$  and  $k$ , and  $N_{nn}$  is the number of nearest neighbors of particle  $j$ . Though this order parameter is typically used for two-dimensional planar systems, it is acceptable to use in the analysis of two-dimensional slices of helical packings. Helical packings are effectively two-dimensional triangular lattices wrapped onto cylinders, and the observed cross-sections of these particular packings exhibit only slight variation from the ideal two-dimensional hexagonal lattice.

We examined the spatial extent of orientational order along the tube by calculating the orientational spatial correlation function,  $g_6(z = |z_j - z_k|) = \langle \psi_{6j}^* \psi_{6k} \rangle$ , where  $z_j$  is the axial position of particle  $j$ . As depicted in Fig. 2.14, the resulting correlation functions decrease quickly at low

volume fractions, as expected in a disordered state. However, at high volume fractions, these functions exhibit long-range order within the experiment's field of view. These experimental observations are consistent with an expectation of long-range orientational order. Granted, the finite size of the system restricts observations of correlations beyond much more than an order of magnitude in separation distance, so it is difficult to declare with certainty that these correlation functions do not drop off exponentially at longer distances, or decay algebraically (as is the case with quasi-long-range orientational order in 2D hexatic phases). However, though long-range *translational* order is impossible in a one dimensional system at finite temperature [162], as discussed in Section 2.2.3, long-range *orientational* order could be possible, just as it is in the much-storied theory of two-dimensional melting [117].

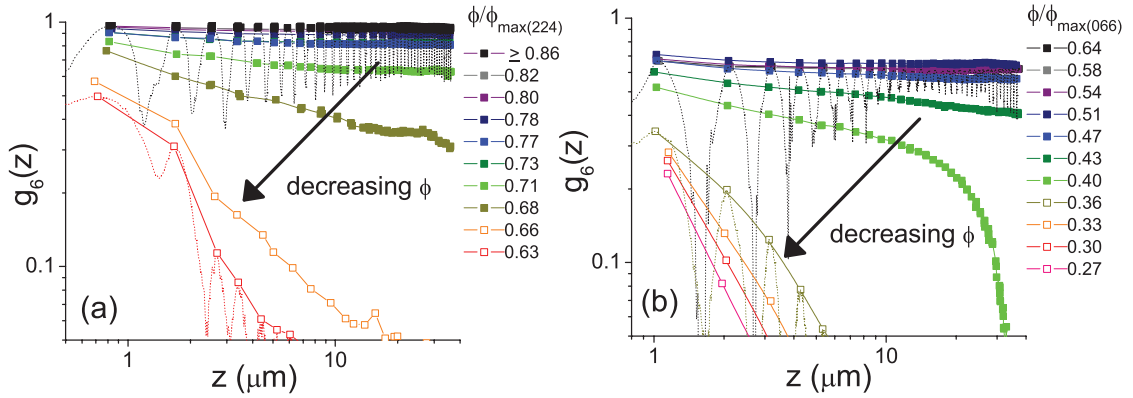


Figure 2.14: Local maxima of orientational spatial correlation function  $g_6(z)$  for samples with (2,2,4) packing (a) and (0,6,6) packing (b). Dashed lines: Full correlation function at  $\phi/\phi_{\max(224)} = 0.86$  and  $0.63$  (a) and  $\phi/\phi_{\max(066)} = 0.64$  and  $0.36$  (b), where  $\phi_{\max}$  is the maximum volume fraction for a given packing of hard spheres with the observed particle spacing. Empty symbols indicate samples with short-range order. Oscillations arise from the periodic distribution of particle positions along the tube axis. Full correlation functions were calculated for all volume fractions, but omitted for the sake of clarity.

To our knowledge, the existence of long-range orientational order has not been characterized in previous studies of packing in cylindrical systems [33, 46, 61, 84, 131]. At low volume

fractions, one expects long-range orientational correlations to disappear, and this behavior is observed in our experiment. It is important to consider, however, that this analysis requires a 2D projection of a three-dimensional structure. Since our three dimensional confocal imaging is rather limited, it is difficult to tell the exact degree to which these particles are localized to the surface of the cylinder. Thus, we emphasize that further analysis of the three-dimensional structure would elucidate whether a generalization of the two-dimensional KTHNY theory [117] is truly appropriate for this system.

We also note that, though the observed correlation functions are persuasive evidence for long-range orientational order, the true nature of this ordering could be quite complicated. For example, the orientational order might just persist in this system to outside the scope of the experimental field of view, and thus might not actually be truly long-ranged. Or, if it is truly long-range, orientational order could be enhanced, by interactions of the packings with the highly curved boundary. As mentioned in section 2.2.1, the helical structures we observe have a very well-defined geometrical relationship between packing diameters and pitch (which is related to the local packing orientation). Thus, the diameter of the confining tube could be considered as an “ordering field”, causing a preference for packings with a certain local orientation.

### **2.4.3 Theoretical Model for Long-Range Orientational Order in Helical Packings**

Here we now present a theoretical argument, which was worked out largely by B. G. Chen with guidance from Prof. R. Kamien, wherein we show that long-range orientational order could persist even in this quasi-one-dimensional system. We do this by evaluating the orientational correlation function  $g_6(r)$  using the isotropic elasticity free energy [117] in an “unwrapping” of the particles on the cylinder surface onto a two-dimensional infinitely long strip. We assume that

particles are packed densely enough so that fluctuations along the radial direction of the cylinder may be neglected. In this discussion, we refer to the direction along the length of the cylinder as the  $x$  direction. As  $x \rightarrow \infty$ ,  $g_6$  approaches a constant. Thus, finite correlations exist at infinite distance, a hallmark of a phase with long-range order.

The above argument is performed by following the same strategy used by Nelson and Halperin in [117], but this time applied to a quasi-*one*-dimensional system to show that there is long-range orientational order in such systems at low temperatures. The system we consider is a two-dimensional box which is infinite in the  $x$  direction and periodic with length  $L$  in the  $y$  direction. Note that such a system applies to the problem of spherical particles in a cylinder if we assume that at high densities, the outer layer of spheres in the cylinder behave as if they were disks lying in a two-dimensional strip with periodic boundary conditions – that is, we “un-wrap” the spheres onto a plane and neglect the radial (which become out-of-plane) fluctuations. This maps  $\psi_6$  defined in the quasi-*one*-dimensional system approximately onto the  $\psi_6$  that was measured on the surface of the cylinder.

We calculate a few quantities in the low-temperature (“solid” phase) by using an isotropic Lamé elasticity free energy. The following expression is appropriate for the elasticity of a triangular lattice with the given geometry:

$$F = \frac{1}{2} \int_{-\infty}^{\infty} dx \int_0^L dy [\lambda u_{ii}^2 + 2\mu u_{ij} u_{ij}] \quad (2.6)$$

Here  $u_{ij} = \frac{1}{2} (\partial_i u_j + \partial_j u_i)$  is the displacement from the (zero-temperature, hexagonal) ordered state. This free energy assumes that there exist nonzero elastic moduli  $\lambda$  and  $\mu$ , a natural assumption we must make.

As in two-dimensions, at finite temperatures, there can be no long-range positional order in this system, so fluctuations drive the correlations of  $\psi_G = e^{iG \cdot u}$  (the density amplitude at reciprocal lattice vector  $G$ ) to zero at large  $x$ . This can be seen by evaluating  $\langle \psi_G(x) \psi_G^*(0) \rangle$ :

$$\begin{aligned}
\langle \psi_G(x) \psi_G^*(0) \rangle &= \langle e^{iG \cdot (u(x) - u(0))} \rangle \\
&= \exp \left( -G^2 [\langle u(0)^2 \rangle - \langle u(x)u(0) \rangle] \right) \\
&= \exp \left( -G^2 \frac{k_B T}{L} \sum_{n=-N}^N \int_{-\Lambda}^{\Lambda} \frac{dq_x}{2\pi} \right). \tag{2.7}
\end{aligned}$$

To calculate the correlation function of orientational order, we first define  $\psi_6 = e^{6i\theta}$ , where  $\theta$  measures the bond angles between nearest neighbor particles (the factor of 6 arises from the triangular symmetry of the lattice). Furthermore, we will use the fact that the angle  $\theta$  can be shown to be  $\frac{1}{2} \nabla \times u$ .

The fact that the theory is quadratic allows us to take two shortcuts. First, we can evaluate  $\langle \psi_6(r) \psi_6^*(0) \rangle$  (where  $r = (x, y)$ ) as the exponential of an average. Second, this average can be evaluated simply since the inverse of the elasticity dynamical matrix is known [6,8] to be

$$D_{jn}^{-1} = \left\{ \frac{1}{\mu q^2} \left( \delta_{jn} - \frac{q_j q_n}{q^2} \right) + \frac{1}{\lambda + 2\mu} \frac{q_j q_n}{q^4} \right\}.$$

It may be worthwhile to point out that we can guess the result from ‘‘counting powers of  $q$ ’’. We can see that translational order is destroyed in this system by estimating the scaling of the (Fourier-space) correlation function of  $u$  at low  $q$ . To do this, we integrate  $D_{jn}^{-1}$  in one dimension. But  $D_{jn}^{-1}$  scales as  $q^{-2}$ , so the result  $\int q^{-2} dq$  scales like  $1/q$ . This diverges at low  $q$ , meaning that long-wavelength fluctuations drive positional correlations to zero.

However, since  $\theta$  is related to the *derivative* of  $u$ , the (Fourier-space) correlation function of  $\theta$  will involve an extra factor of  $q$  for each  $\theta = \nabla \times u$ . We thus expect the two-point correlation function to scale as  $\int dq(q^2)(q^{-2}) \sim q$ , which is finite at low  $q$ , indicating long-range order at infinity.

We now proceed with a more detailed calculation of the real-space orientational order correlation function:

$$\begin{aligned}
\langle \psi_6(r)\psi_6^*(0) \rangle &= \exp[-36(\langle \theta^2(0) \rangle - \langle \theta(r)\theta(0) \rangle)] \\
&= \exp \left[ -\frac{9k_B T}{2\pi L} \epsilon_{ij}\epsilon_{mn} \sum_{n=-N}^N \int_{-\Lambda}^{\Lambda} dq_x q_i q_m \left( 1 - e^{i(q_x x + 2\pi n y/L)} \right) D_{jn}^{-1} \right] \\
&= \exp \left[ -\frac{9k_B T}{2\pi \mu L} \sum_{n=-N}^N \int_{-\Lambda}^{\Lambda} dq_x \left( 1 - e^{i(q_x x + 2\pi n y/L)} \right) \right] \\
&= \exp \left[ -\frac{9k_B T}{2\pi \mu L} \sum_{n=-N}^N \left( 2\Lambda - e^{i2\pi n y/L} \frac{e^{i\Lambda x} - e^{-i\Lambda x}}{ix} \right) \right] \\
&= \exp \left[ -\frac{9k_B T}{2\pi \mu L} \left( 2\Lambda(2N+1) - \frac{\sin(2\pi(N+1/2)y/L)}{\sin(\pi y/L)} \frac{2\sin(\Lambda x)}{x} \right) \right]. \quad (2.8)
\end{aligned}$$

We now let the cutoff  $\Lambda$  be  $2\pi(N+1/2)/L$  and use the sinc function ( $\text{sinc } t = (\sin t)/t$ ):

$$\begin{aligned}
\langle \psi_6(r)\psi_6(0) \rangle &= \exp \left[ -\frac{9k_B T}{\pi^2 \mu} \left( \Lambda^2 - \Lambda^2 \frac{\pi y}{L} \frac{\sin(\Lambda y)}{\sin(\pi y/L)\Lambda y} \frac{\sin(\Lambda x)}{\Lambda x} \right) \right] \\
&= \exp \left[ -\frac{9k_B T \Lambda^2}{\pi^2 \mu} \left( 1 - \frac{\text{sinc}(\Lambda x)\text{sinc}(\Lambda y)}{\text{sinc}(\pi y/L)} \right) \right]. \quad (2.9)
\end{aligned}$$

For large  $x$ , this quantity approaches the constant  $\exp\left(-\frac{9k_B T \Lambda^2}{\pi^2 \mu}\right)$ , and hence this quasi-one-dimensional system has long-range orientational order. This result suggests that our experimentally observed long-range correlations in the orientational order parameter at high densities are real.

We emphasize that the above relation should not be fit to experimental or simulation data in the present form for the following reasons. First, the elastic field theory describes the sphere systems at large wavelengths. This approach is fine for the purposes of searching for long-range orientational order, but it is inappropriate for extraction of quantitative correlation functions.

Another issue is that the precise functional form of the above relation arises from the cutoff scheme chosen. Ideally, one would apply a physical theory which describes the higher wavelength modes and how the system responds to them (in the case of spheres, part of this scheme could be a density functional-like theory), which would be more suitable for capturing the behavior of the correlation function over short distances than the hard cutoff that we used. Thus the primary experimentally accessible result for comparison to theory is the fact that the correlation function remains finite at infinity.

#### **2.4.4 Orientational Order Parameter, Susceptibility, and Evidence of a Phase Transition in Experiment**

To quantify the crossover from long-range to short-range order in the experimental system, an average orientational order parameter  $|\psi_6|$  is defined for each frame, where  $\psi_6 = \frac{1}{N} \sum_j^N \psi_{6j}$ . The height of the first peak of the one-dimensional axial structure factor  $S(k_{max})$ , where  $S(k) = [N(N-1)]^{-1} \left| \sum \sum e^{ik|z_l - z_m|} \right|$ , is used as a translational order parameter. Here,  $z$  denotes the

axial position of each particle,  $N$  is the number of particles in the field of view at a given time, and  $k_{max}$  is chosen iteratively for each volume fraction.

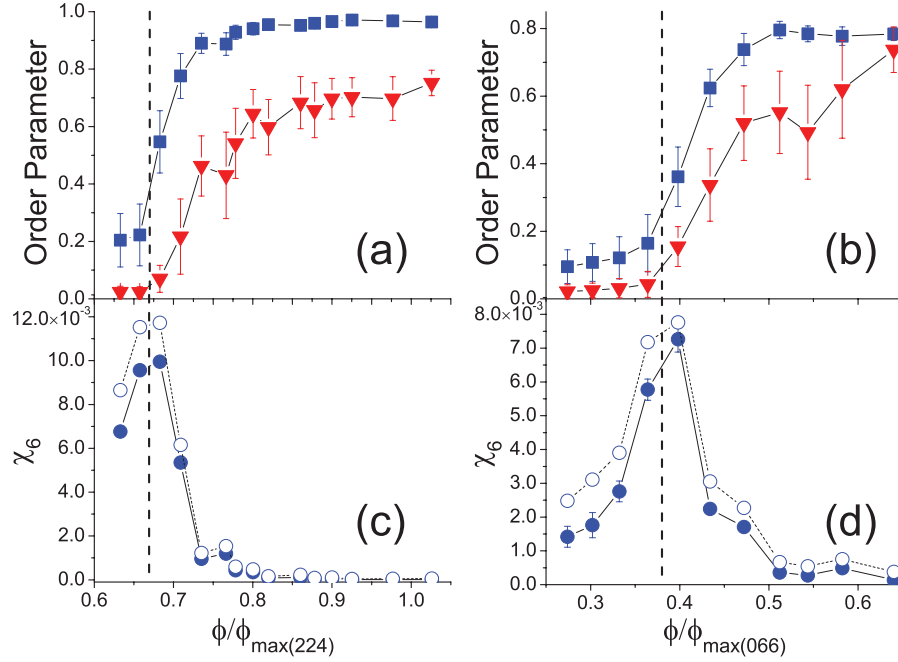


Figure 2.15: Top: Mean values of translational (red  $\blacktriangledown$ ) and orientational (blue  $\blacksquare$ ) order parameters for (a) (2,2,4) and (b) (0,6,6) samples. Bottom: Orientational susceptibilities for (c) (2,2,4) and (d) (0,6,6) systems, for sample size = 75  $\mu\text{m}$  ( $\circ$ ) and =  $\infty$  ( $\bullet$ ). Dashed vertical lines at  $\phi/\phi_{max(224)} = 0.67$  and  $\phi/\phi_{max(066)} = 0.38$ .

In Fig. 2.15, it is evident that both the average translational and orientational order parameters cross from an ordered state at high volume fraction to a disordered state at low volume fraction, though the change in  $|\psi_6|$  is significantly sharper than the change in  $S(k_{max})$ . The orientational crossover complements a recent simulation which finds a similar crossover in hard sphere packings with decreasing density [33].

While such order parameters help to qualitatively identify a crossover, this type of analysis by itself is sensitive to finite-size and finite-time ambiguities. Previous work has shown that fluctuations in order parameter are more useful for identifying phase transition points and are

therefore less susceptible to such finite-size effects [51]. To characterize fluctuations in orientational order, we calculate the orientational susceptibility,  $\chi_6 = \langle |\psi_6|^2 \rangle - \langle |\psi_6| \rangle^2$ , where  $\langle \rangle$  represents the time average. Statistical effects of the finite size of the system are accounted for by calculating the susceptibility of different sub-segments of length  $L$  in the system and extrapolating to the limit  $L \rightarrow \infty$ , similar to the calculations in [51]. Specifically, we calculated  $\chi_6$  in different size sub-boxes within the sample and extrapolated to  $\chi_{6\infty}$ , thus attaining the thermodynamic limit.

Plots of  $\chi_6$  and  $\chi_{6\infty}$  in Fig. 2.15 clearly demonstrate a peak in the orientational susceptibility. The location of this peak coincides with the onset of both orientational and translational order in the system. Translational susceptibilities were also calculated, but did not exhibit clear peaks or trends with respect to the order parameters or volume fraction. We do not expect any transition-like behavior from translational susceptibilities, due to arguments from [162] against long-range translational order, which apply in quasi-1D.

The existence of a diverging susceptibility of an order parameter typically indicates a phase transition [70]. However, it is difficult from the given data points to determine if this data truly diverges, and whether this divergence would indicate a first-order (asymmetrically diverging at different temperatures from either side) or second-order (symmetrically diverging at one temperature) phase transition. One of the most obvious indicators distinguishing a first-order and second order transition is the existence of stable coexistence between ordered and disordered phases. Qualitative observation of the melting of these packings shows evidence of more and less ordered states coexisting. However, quantification of structural order parameters does not show distinct regions quite as easily. Specifically, the local magnitude of the the orientational

order parameter,  $|\psi_{6i}|$ , does not show much local variance, though there are obvious qualitative differences in the dynamics through the sample.

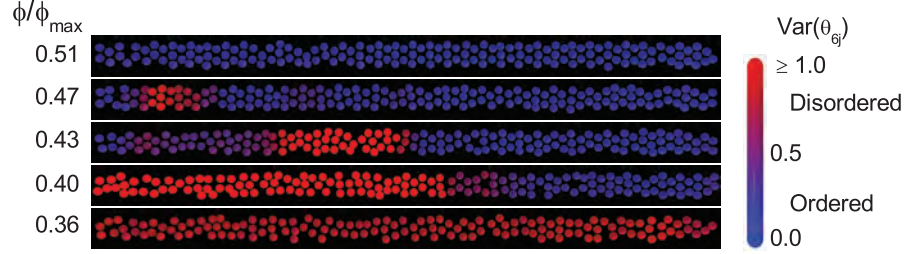


Figure 2.16: Snapshots of particle positions from a (0,6,6) structure exhibiting coexisting ordered and disordered domains. Color represents local variance of the phase of  $\psi_6$ ,  $\langle \theta_{6j}^2 \rangle - \langle \theta_{6j} \rangle^2$ , in  $1.2 \mu\text{m}$  segments.

To better quantify the change in structural order and dynamics qualitatively observed in the system, we look at the phase of the local order parameter. Being a complex order parameter, we can represent  $\psi_{6i}$  as  $|\psi_{6i}|e^{i\theta_{6i}}$ , where  $|\psi_{6i}|$  gives the local degree of hexagonal order around a single particle  $i$ . The phase of this order parameter,  $\theta_{6i}$ , indicates the local rotation angle of the hexagon of particles surrounding particle  $i$ . The variance of  $\theta_{6i}$  over time gives us an idea of the local dynamics and structural fluidity. Indeed, looking at the spatial distribution of  $\text{var}(\theta_{6i})$  clearly indicates the coexistence of more fluid and solid-like domains. Specifically, upon closer examination of the (0,6,6) sample, we observe coexistence of ordered and disordered domains for  $\phi/\phi_{\max(066)} = 0.47 - 0.40$  (Fig. 2.16). We also observe the appearance of a disordered domain in the (2,2,4) sample at  $\phi/\phi_{\max(224)} = 0.68$ . The appearance of these coexisting domains is consistent with the spatial correlation functions exhibiting neither long-range nor short-range behavior at intermediate volume fractions in Fig. 2.14 ( $\phi/\phi_{\max(066)} = 0.40$ ,  $\phi/\phi_{\max(224)} = 0.68$ ). The presence of such solid-liquid coexistence has also been seen in recent simulations of hard spheres in cylinders [61].

### 2.4.5 Structural Transformations in Chiral Packings

In certain observed samples, domains with different local pitch and structure often appear as volume fraction decreases (Fig. 2.17). The appearance of these domains was difficult to quantify, since domains would grow, shrink and/or disappear with decreasing volume fraction. Also, since each domain was equally ordered, just with a different crystal lattice orientation relative to the cylinder geometry, conventional order parameters were not helpful distinguishing structures (for example,  $|\psi_{6i}|$  would have practically the same local value between two structures of different pitch or chirality).

Therefore, we again turn to the phase of the local orientational order parameter  $\psi_{6i}$ ,  $\theta_{6i}$ , to characterize the local structural pitch. As mentioned in the previous section,  $\theta_{6i}$  indicates the local rotations of hexagons with respect to the long axis of the cylinder. More specifically,  $\theta_{6i} = 0$  indicates a lattice vector running along the long axis of the cylinder, while  $\theta_{6i} = \pm\pi$  indicates a lattice vector running around the circumference of the cylinder. When the helical hexagonal packings are “unrolled” onto a plane, each packing  $(m, n, m + n)$  will have a unique characteristic  $\theta_{6i}$ . For example, in the regime of structural diameters observed in our experiments,  $\theta_{6i} = 0.67$  indicates a  $(2, 3, 5)$  structure. Additionally, the magnitude of  $\theta_{6i}$  will indicate the topology of the structure, and its sign will indicate its chirality. For example, while  $\theta_{6i} = 0.67$  indicates a  $(2, 3, 5)$  structure,  $\theta_{6i} = -0.67$  indicates a  $(3, 2, 5)$  structure.

The structures observed in coexisting states were those with most similar predicted linear densities and  $D/d_{sep}$  values. Specifically, as shown in Fig. 2.17, a structure starting in a  $(2, 3, 5)$  configuration transitions to domains with local structures of  $(3, 2, 5)$  and  $(0, 4, 4)$ . Additionally, a second sample starting in the  $(0,6,6)$  structure was seen to transition to  $(2, 4, 6)$  and  $(1, 5, 6)$

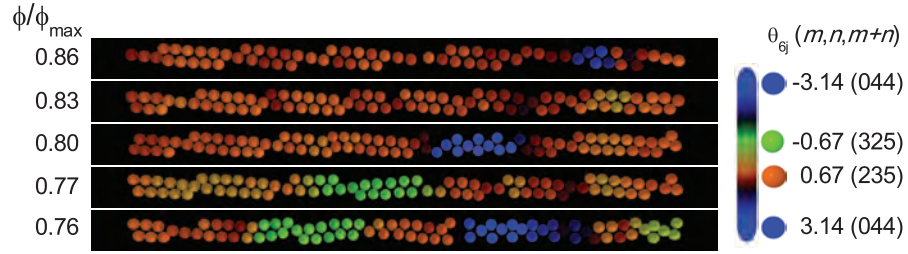


Figure 2.17: Snapshots of particle positions from a (2,3,5) structure with emerging domains of (3,2,5) and (0,4,4) structures. Color represents phase of  $\psi_{6j}$ ,  $\theta_{6j}$ , which characterizes packing orientation. Structures corresponding to each  $\theta_{6j}$  given on right.

domains. A third packing saw transitions between (2, 5, 7) and (1, 6, 7) domains. These results, specifically, transitions between structures with similar  $D/d_{sep}$  values, are consistent with hard sphere simulations [84, 131].

This coexistence of ordered structures should not be confused with dislocation-mediated structural transformations theoretically studied [53] and observed [9, 10, 132, 133] in athermal helical crystals, and described in more detail in Section 2.2.2. This is largely because certain observed boundaries between coexisting structures, specifically, (2, 3, 5) and (0, 4, 4) structures, as well as (0, 6, 6) and (2, 4, 6) cannot be mediated by the presence of a single dislocation. If transitions and coexistence of such packings are mediated by the formation and glide / climb of multiple dislocations, it is difficult to observe from this data, as three dimensional packing geometries and dislocation configurations are difficult to extract.

## 2.5 Conclusions

In summary, we created ordered helical packings of thermoresponsive colloids and observed the presence of long-range order resilient to thermal fluctuations. Sharp crossovers from orientationally ordered to disordered phases with decreasing volume fraction were observed. In addition,

we find basic evidence for abrupt volume-fraction driven structure-to-structure transitions. These findings raise and elucidate fundamental questions on the subject of melting in 1D.

Even so, the nature of this crossover is complicated, and merits further study. For example, there is some uncertainty whether it is truly appropriate to treat phase behavior in this system as “quasi-2D”, or whether the apparent stability of orientational order stems from interactions of the packing with its confining boundary. Such questions could be answered with an improved experiment using higher-resolution 3D particle tracking to observe radial fluctuations of particle positions in ordered and disordered phases. Also, if the observed long-range orientational order is, in actuality, only of the order of the system size, it would be useful to perform further experiments probing the relationship between inter-particle interactions and order lengthscales.

A more sophisticated theoretical treatment which includes effects of system boundaries would also help clarify such questions. Additionally, examining other quasi-1D systems with orientational order theoretically and experimentally, i.e. liquid crystals or anisotropic particle packings in confinement, might clarify the robustness of orientational order in restricted dimensions. It might be particularly interesting to create experimental realizations of simulated 1D systems which always demonstrate long-range orientational order (i.e., rotating anisotropic particles with centers on a fixed line) [50, 70].

## **Chapter 3**

# **Low-Frequency Modes as a Hallmark of Structural Crossovers in Quasi-2D Dense Attractive Colloidal Packings**

### **3.1 Introduction**

Philip W. Anderson stated in 1995 that “the deepest and most interesting unsolved problem in solid state theory is probably the theory of the nature of glass and the glass transition” [2]. Most experimental, numerical and theoretical work in the subsequent two decades has focused on dense, disordered packings of repulsive particles [36, 62]. Far less is known about the structural and vibrational properties of disordered packings of particles with attractive interactions. Broadly, packings of particles with short-ranged attractions are described by two classes of dynamically arrested states [160, 181, 182]. The terms “attractive glass” and “bonded repulsive

glass” are used to denote a dense packing of attractively-interacting particles with uniform structure, and the term “gel” is used for a class of more dilute, yet still dynamically arrested, packings. These two “states” of matter are typically distinguished by a qualitative description of their structure and dynamics. Though some work has been done to try to characterize the crossover between attractive glasses and gels [34, 86, 182, 183], to date no precise (i.e., universal) microstructural or dynamical signature of the gel-to-glass crossover had been identified.

In this chapter, we investigate this packing-fraction driven crossover. In particular, we study the vibrational modes of quasi-2D dynamically arrested samples of thermal colloidal particles with attractive inter-particle interactions. We find that a crossover from glassy to gel-like states is indicated by a significant increase in low-frequency vibrational modes at sufficiently low packing fraction. These modes appear to be highly localized to regions of the sample with low local coordination. Though these modes do not obviously correlate to a specific feature, the distinctness in the change in vibrational modes suggests a significant structural change which might serve as a signature of gel-like and glassy packings of attractive particles.

## **3.2 Contextual and Theoretical Background**

### **3.2.1 Attractive Glasses**

The so-called attractive glass (or bonded repulsive glass, to use a recent parlance [182]) is a disordered state of matter with high density and spatially uniform structure. Its dense structure is thus similar to the (non-bonded) repulsive glass, though the attractive glass is also characterized by strong inter-particle attractions. Note, herein, we use the term attractive (repulsive) glass or colloid to denote an ensemble wherein interparticle attractions are attractive (repulsive). A

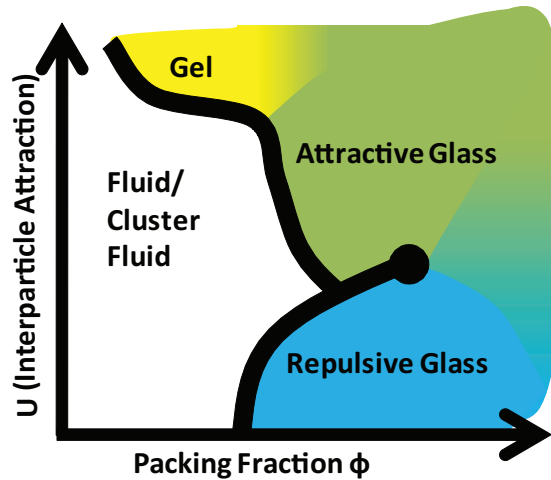


Figure 3.1: Qualitative phase diagram of disordered packings as a function of packing fraction  $\phi$  and inter-particle attraction strength  $U$ .

distinct transition between repulsive and attractive glasses as a function of increasing attraction strength has been predicted by mode coupling theory (MCT) [7,39]. In less dense, but still glassy packings, changes in inter-particle attraction can even produce re-entrant melting phenomena. For example, adding interparticle attractions to a purely repulsive glass causes particles to cluster together and thereby frees up more room for particle rearrangements; as a result, the glass melts into a fluid phase. A continued increase in interparticle attraction, however, can drive the fluid into dynamic arrest again, i.e., it drives formation of the attractive glass phase. This re-entrant phenomena has been observed in several experiments [35, 89, 130].

Additional phenomenological differences in repulsive and attractive glasses arise as a result of slightly different dynamical arrest mechanisms. In a repulsive glass, for example, particle dynamics slows due to local crowding, and in the attractive glass, there is an additional slowing of dynamics caused by strong inter-particle attractive bonds. These effects give rise to differences in bulk rheological properties, specifically, two-step yielding in attractive glasses [86, 128, 129].

### 3.2.2 Gels

Though gels are a common component of consumer products and biological systems, they are a poorly defined “state” of matter from a physics perspective [182]. The term “gel” can be used to describe any low-density, spatially heterogeneous material with solid-like properties. Such materials can form from any collection of particles with sufficiently strong attraction, be they colloidal particles in a polymer solution aggregating from depletion forces [96], clay disks with anisotropic electrostatic interactions [88], or carbon nanotubes in solution interacting through nonspecific bonding interactions [59].

As a consequence, so-called gel structures can vary significantly depending on inter-particle interactions and assembly dynamics [182]. In the limit of strong inter-particle attraction, particles will stick and freeze in place as soon as they come into contact. The resulting states, called irreversible or “chemical” gels, are well described by percolation theory. Such structures, formed by a rapid quench, are described by diffusion-limited cluster aggregation (DLCA, fractal dimension  $d_f \approx 1.8$ ); similar structures, which are formed more slowly, are described by reaction-limited cluster aggregation (RLCA,  $d_f \approx 2.3$ ). If, on the other hand, inter-particle attraction is on the order of the thermal energy  $k_B T$ , then a more compact “physical” gel with frequent bond relaxations and rearrangements will form. Additionally, there is a significant structural difference between systems with only short-range attraction versus systems stabilized at lower densities by repulsive barriers or by limited attractive valences. The former systems typically phase separate into locally dense clusters; the latter systems typically approach percolation through well-dispersed equilibrium fluid states [182].

### 3.2.3 Differences between Gels and Attractive Glasses

Gels and attractive glassy phases are quite difficult to distinguish in systems with strong inter-particle attraction and intermediate densities. Gels are typically qualitatively distinguished from glasses by obvious structural inhomogeneities, but this approach is a difficult task in packings that are dense enough to be nearly, but not entirely, uniform. Additionally, gels share quite a few of the dynamical traits of glassy materials. For example, dynamical heterogeneity is observed in both glasses and gels [24], though its presence in gels can sometimes be attributed to structural heterogeneity, depending on gel morphology [30, 31]. Also, as in glasses, the relaxation dynamics of gels are often well described by stretched exponential decays [181]. Finally, as will be discussed in a later section, both glasses and gels exhibit an excess of low-frequency vibrational modes compared to predictions for ordered solids [18, 139].

This is not to say that there have been no previous attempts to find a hallmark of the gel-to-glass transition. Simulations of attractive systems have found differences in gels and attractive glasses in their relaxation dynamics, e.g., evident in an upturn in the gel mean-squared displacement (MSD) at long timescales [182]. A simplified theoretical model has predicted that the elastic modulus of a glass should be dominated by inter-*particle* elasticity, while the structural inhomogeneities in a gel will cause the elastic modulus to be dominated by inter-*cluster* elasticity [183]. Further, rheological experiments on attractive colloidal suspensions have observed a transition from two-step yielding in attractive glasses to one-step yielding in *very sparse gels* [86]. Other recent experiments combined light scattering and rheology to determine a dynamic arrest transition line in ensembles of thermally tunable attractive nanoparticles [34]. These experiments found that this line deviates from a percolation-based prediction at the low-attraction

border of the gel-to-glass transition.

Nevertheless, despite the breadth and rigor of this preceding work, a specific microstructural or dynamical signature of the gel-to-glass crossover in a static experimental sample with strong attractions has yet to be determined. In addition, a fair amount of this previous work relies on rheological properties to distinguish phases. Though rheology is useful for probing the bulk properties of materials, the identification of phase behavior in an *unperturbed* or “static” sample (that is, a dynamically arrested structure not under shear) would enable categorization without significantly changing the morphology of the structured material (e.g., as shearing has been shown to do in marginally sparse attractive packings) [90].

### 3.2.4 Phonons in Disordered Solids

In recent years, experimental calculations of the vibrational modes of colloidal materials have become a useful tool for investigating phase behavior, bulk properties and local structure in ordered and disordered packings [18–20, 42, 43, 47, 54, 72, 101, 147, 179, 180]. We discuss the details of this technique in Section 3.3.2. Here, we briefly touch on the motivations for applying this analysis to attractive disordered packings.

#### 3.2.4.1 Conventional Low-Frequency Phonon Behavior: The Debye Model

A traditional theory for describing vibrational modes in a solid material is the so-called Debye model. This model assumes a continuous elastic medium, where vibrational modes at low frequencies are described as plane waves with a dispersion relation  $\omega = c|\vec{k}|$ ; here  $\omega$  is the frequency of a given mode,  $\vec{k}$  is its wavevector, and  $c$  is the speed of sound at that particular frequency. In a  $d$ -dimensional system, one can determine the vibrational density of states

(vDOS) by calculating the number of vibrational modes in an infinitesimal frequency interval  $[\omega, \omega + d\omega]$ . For example, given a periodic array of constituent particles, the Debye model assumes an even distribution of modes in  $k$ -space. Then, for a given frequency  $\omega = c|\vec{k}|$ , there exists a degeneracy of modes proportional to the area of a surface with constant  $|\vec{k}|$ . For a  $d$ -dimensional system, this yields a density of states  $\propto \omega^{d-1}$ . This prediction turns out to be an accurate descriptor for many solid materials at low frequencies, and it is typically used to model the temperature dependence of specific heat ( $C_V$ ) in crystalline solids at low temperature (i.e.,  $C_V \propto T^3$ ).

#### 3.2.4.2 Low-Frequency Phonons in Disordered Solids

A puzzling property of amorphous solids is that the density of low-frequency vibrational modes can significantly exceed the Debye prediction. When a vDOS (or  $D(\omega)$ ) curve is normalized by the expected Debye behavior, i.e.  $D(\omega)/\omega^{d-1}$ , this excess is apparent as a “bump” commonly referred to as the “Boson peak.” Though the height and position of this Boson peak has been used as an indicator of the glass transition in disordered materials [18, 169], the exact nature of this excess of low-frequency modes remains a current topic of theoretical and experimental investigation. Besides being observed in dense glassy systems, for example, features resembling the Boson peak have been observed in sparser gel-like systems [139], as well as structural crystals with bond-strength disorder [47, 48]. Recent studies have made progress in clarifying properties of this Boson peak, if not a universal mechanism behind it. It appears that many modes near and below this frequency tend to be quasilocalized [18, 170]. Additionally, the Boson peak has been observed to evolve into the Van Hove singularity of crystals in disordered packings that are

evolving into a more ordered configuration [22]. Several recent studies have come to the conclusion that that Boson peak frequency represents the high-frequency limit of transverse modes propagating in a disordered material [143, 153].

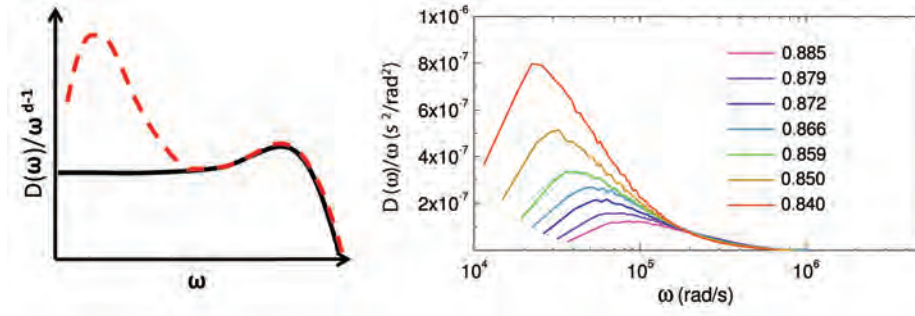


Figure 3.2: (Left) Illustration of the difference in low-frequency density of states  $D(\omega)$  in an ordered Debye solid (black solid line) and a disordered glassy solid (dashed red line) with  $d$  dimensions. Note the boson peak exhibited at low frequencies exhibited by the disordered solid. (Right) vDOS calculated from particle trajectories in quasi-2D disordered packings of thermal colloidal microgel spheres with soft repulsive interactions at various area fractions  $0.840 < \phi < 0.885$ , adapted from [18]. Note low-frequency peak which changes height and frequency location with area fraction.

Low-frequency modes in disordered packings also highlight otherwise unobservable structural features. Specifically, experimental [19, 42] and numerical [12, 13, 101, 165] studies have observed that quasi-localized low-frequency modes show enhanced participation in areas that are particularly prone to irreversible rearrangements with the application of shear. These areas, termed “soft spots”, are thus considered the amorphous equivalent of dislocation or grain boundary defects in ordered media which (in polycrystalline materials) move in response to mechanical forces. Though the exact structural properties of these “soft spots” are not entirely clear, previous work has observed that particles in “soft spot” regions exhibit increased local motion and are to some degree associated with local structural order and free volume [71].

While an excess of low-frequency vibrational modes have been observed in gel-like materials, the nature of these modes is complicated by the heterogeneous structure of the gel. Recent simulations of sparse, stringy gels of patchy particles observe an excess of low-frequency modes which are tentatively labeled a “boson peak” and are associated with long-wavelength transverse modes of long linear particle chains and related rotational/translational mode coupling [139]. Direct acoustic measurements of ultrasonic vibrational modes in particle gels predict non-Debye behavior in a “diffusive” regime where plane mode wavelengths exist on the size scale of structural heterogeneities and thus scatter diffusively [25, 186]. Additionally, it has been shown that structural heterogeneity in gels has varying correlations to dynamic heterogeneity depending on its overall morphology [30, 31]. One such specific effect is that particles at surfaces in sparse gels will exhibit enhanced motion compared to more closely packed regions. One could imagine that such relationships between structure and dynamics would be reflected in vibrational modes.

Our experimental work is motivated, in large part, by an effort to make connections (or distinctions) between the low-frequency vibrational behavior observed in dense glassy phases, i.e., boson peaks and soft spots, and the structure-induced prevalence of low-frequency modes observed in sparse gels. If the low-frequency behavior were to change continuously from attractive glasses to gels, then perhaps an obvious structural feature of low-frequency modes in gels could be extrapolated to denser packings and could further elucidate the structural nature of soft spots or the boson peak. If, on the other hand, one were to observe very different low-frequency behavior in sparse and dense colloidal packings, then one might surmise that there exists a distinction between the low-frequency effects caused by structural heterogeneities and those caused by local disorder. In this case, one might become disinclined to apply the broad term of “boson peak” to

any deviations from Debye behavior.

### **3.3 Experimental and Analytical Methods**

#### **3.3.1 Sample Preparation**

We create attractive colloidal monolayers in a manner that ensures observable Brownian motion in dense, attractive packings. Bidisperse suspensions of carboxyl-modified polystyrene (PS) colloidal spheres (1  $\mu\text{m}$  and 1.4  $\mu\text{m}$ , Invitrogen) in a 1:1 number ratio are suspended in a mixture of water and 2, 6 lutidine near its critical composition, i.e., with a lutidine mass fraction of 0.28. At a critical temperature of 306.5 K, this solvent mixture induces a wetting-mediated short-range attractive interaction between particles with a strength of  $\approx 4k_B T$  [8, 179, 180, 185]. We place dilute suspensions of these particles (1 % wt/wt) between two hexamethyldisilazane (HMDS) functionalized glass coverslips separated by a 25  $\mu\text{m}$  spacer, and we then place the sample on an inverted microscope with an oil-immersion objective, and finally we heat the sample to the colloidal aggregation temperature using a high-stability objective heater (Bioscience Tools).

##### **3.3.1.1 Issues Forming Quasi-2D Thermal Attractive Monolayers**

Though the described method might appear fairly straightforward, many subtleties arise and need to be considered in order to create a dynamically arrested, stable, thermal, attractive, dense, and quasi-2D packing. One might, for example, question the use of a binary solvent as a means of inducing attraction between particles, especially since depletion-induced aggregation is simpler

to understand and more straightforward to prepare experimentally. However, by using water-lutidine based wetting instead of a depletion-induced attraction, we are able to keep the viscosity of the solvent low, which minimizes dampening of vibrations in the packings (as noted by [185]). Additionally, a thermally tunable attraction is an important experimental feature for creating very dense, attractive colloidal packings, since one can easily create a dense packing with low attraction and then “turn on” attractive interactions. By contrast, a sample with a constant, strong attraction would dynamically arrest into a gel-like phase at low packing fractions, making attractive glasses difficult to realize experimentally. Further, though temperature-tunable depletants exist, it is difficult to make them tunable from a range of zero attraction to a strong enough attraction to stabilize sparse packings at low densities. Lastly, depletion-based attraction becomes less predictable (and is less well understood) in dense suspensions of particles with little free volume and many-body interactions.

This is not to say that use of the water-lutidine based attraction is entirely straightforward. Our initial experiments in a quasi-2D cell (i.e., two glass slides separated by a space slightly larger than the particle diameter) showed damped motion of particles due to confinement, frequent sticking of particles to surfaces, and huge random particle flows due to water-lutidine phase separation outside the field of view. To prevent irreversible aggregation of colloids onto the surfaces, we silanized the surfaces with a coating of hexamethyldisilazane (HMDS). HMDS has been also been shown to modify the attraction of colloids to surfaces in these binary systems [55]. We do this by placing glass coverslips cleaned with methanol in a closed container with a shallow, open vial of 750  $\mu\text{L}$  of HMDS overnight. Unfortunately, though this coating

procedure prevents particle sticking, the increased hydrophobicity of the slides from this treatment made it more difficult to create sufficiently thin chambers for creating quasi-2D colloidal packings.

### 3.3.1.2 Novel Monolayer Spreading From Lutidine Wetting

We averted several of these aforementioned problems by making our packings on a single surface of a three dimensional cell. This scheme used a previously unrealized phenomenon in the water-lutidine system. At certain concentrations near the critical lutidine mass fraction, raising the temperature of the suspension slightly into the water-lutidine phase separation regime results in a thin layer of lutidine covering the top and bottom surfaces of the cell. If colloids are near the surface, they are pulled into a quasi-2D monolayer by the lutidine layer. Upon cooling back to the colloidal aggregation regime, attraction to the surface keeps the colloids in a surface monolayer as they aggregate into a quasi-2D, dynamically arrested packing.

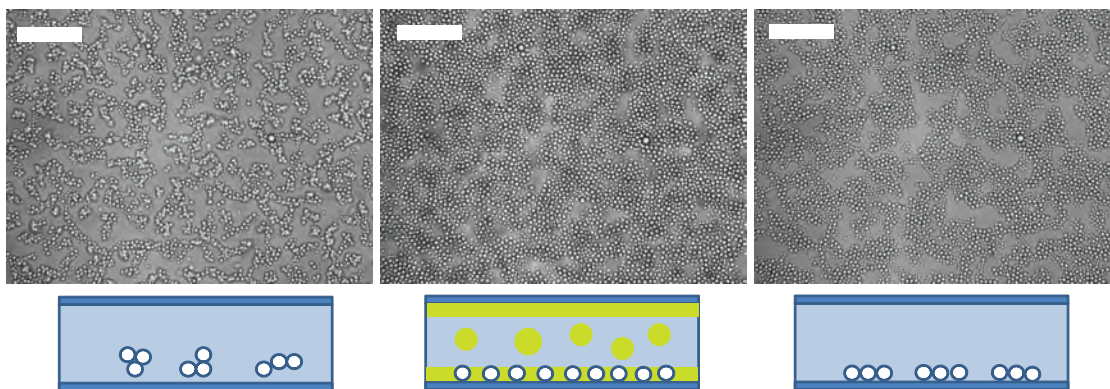


Figure 3.3: Formation of PS monolayers using water-lutidine phase separation, viewed under bright-field microscopy, with accompanying illustrations below. (Left) Three dimensional clusters form and sediment to the bottom of the sample cell at the aggregation temperature. (Middle) Heating sample above the aggregation regime causes phase separation of water and lutidine, pulling PS spheres into a monolayer of repulsive particles at the bottom surface. (Right) Lowering the temperature back to the aggregation regime pins particles to the surface, allowing them to aggregate from short-range attraction to a stable, percolating monolayer. Scale bars =  $20\mu\text{m}$ .

This technique, though useful for creating dense attractive packings with undamped thermal motion, is very sensitive to preparation. In order to observe this effect, the water and lutidine mixture needs to be made the day of the experiment. Also, the ratio of solvent volume to colloidal and cell surface area seemed to significantly affect whether a stable wetting layer of lutidine forms in the phase separation regime. For example, a given suspension might exhibit this wetting effect in a 20  $\mu\text{m}$  thick chamber, but would not show monolayer formation in a 10  $\mu\text{m}$  or 50  $\mu\text{m}$  chamber. Likewise, suspensions with the same ratio of water-to-lutidine and slightly different colloidal densities in identically thick chambers would show different propensities for forming a colloidal monolayer upon water-lutidine phase separation.

We address the sensitivity of this technique by using a repeatable sample preparation procedure with room for slight variations in composition. We first centrifuge a dilute suspension of bidisperse PS spheres ( $\approx 10\%$  wt/wt) and remove supernatant to create a more concentrated suspension (to  $\approx 45\%$  wt/wt). We then separately prepare a mixture of Millipore-filtered water and lutidine at a volume ratio of 2:1 (31.6 % wt/wt lutidine). We mix 100  $\mu\text{L}$  of the water-lutidine mixture with 5-10  $\mu\text{L}$  of the dense colloidal suspension (resulting in a lutidine weight fraction of 28.7 - 30.1 %, close to the critical fraction of 28%). Then, 10-15  $\mu\text{L}$  of suspension is sandwiched between two HMDS coated slides with a single 25  $\mu\text{m}$  spacer on one edge of the cell. The edges are immediately sealed with UV epoxy. While the epoxy is cured under a UV lamp, a small piece of cardboard is used to cover the center of the sample (as it appears intense UV absorption can affect the water-lutidine monolayer formation phenomenon). Variation of the concentration of colloids in suspension and the volume of suspension in the cell (which effects the thickness) changes the area fraction of the resulting attractive monolayer. With each sample

preparation, each factor (including the water/lutidine ratio) must be carefully tuned through trial and error to observe appropriate monolayer formation.

### **3.3.1.3 Temperature Stability**

Once a suitable sample is prepared, it is placed on an inverted microscope stage on a 100x oil-immersion objective. The temperature is controlled through a collar that heats the objective, which is in thermal contact with the sample through immersion oil. Initial experiments used an objective heater with  $\pm 0.1^\circ\text{C}$  stability (Bioptechs). Though this level of temperature control offers sufficient stability for many temperature-dependent colloid experiments, the current set-up can cause significant fluctuations in interaction strength and film stability. This results in particle rearrangements with a period of approximately 60 seconds, the same period of fluctuations seen in the objective heater readout.

To resolve these temperature sensitivity issues, we obtained and utilized a high-temperature stability objective heater (Bioscience Tools). In addition to having a temperature sensor in the heating collar, this heating system includes an external temperature probe, which we place in the immersion oil that is in contact with the objective. With proper adjustment of background heating and feedback sensitivity, this objective heater showed a temperature stability of  $\pm 0.03^\circ\text{C}$  (though we found that the temperature fluctuates slightly during the 60 seconds following a temperature change). Though the advertised stability was  $\pm 0.01^\circ\text{C}$ , the measured  $\pm 0.03^\circ\text{C}$  was sufficient to prevent fluctuations in particle interaction and resulting rearrangements.

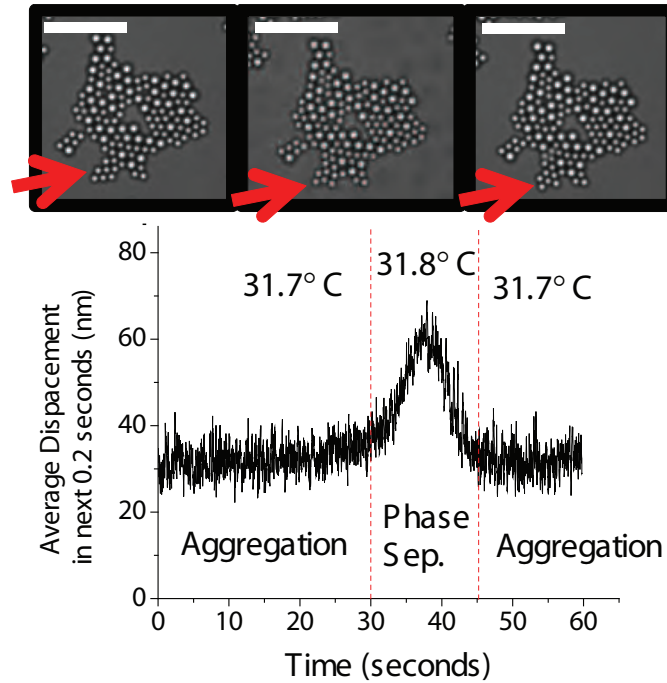


Figure 3.4: Effect of temperature fluctuations in a lower stability objective heater (Bioprotechs). (Bottom) Average particle displacement in a PS monolayer aggregate over the next 0.2 seconds during a temperature fluctuation of 0.1 °C, taking the sample out of the aggregation regime. (Top) Bright field microscope images of an attractive monolayer cluster during the temperature fluctuation. Red arrow indicates a sub-cluster of particles that undergoes an irreversible rearrangement during the temperature fluctuation. Scale bar = 10 $\mu$ m.

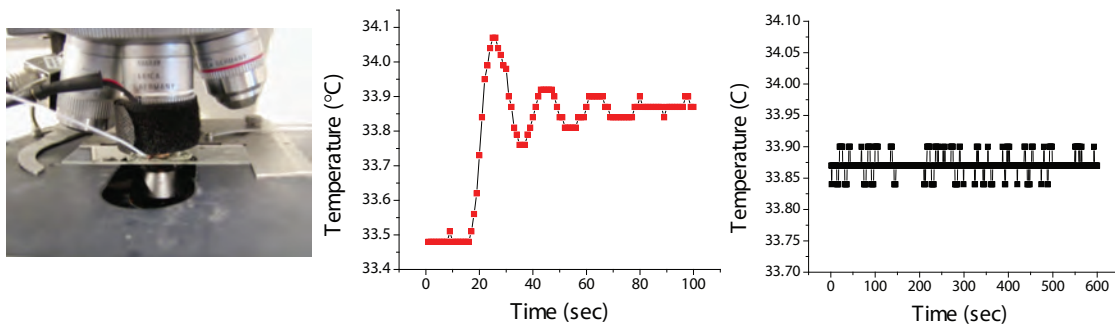


Figure 3.5: Higher stability objective heater setup (Bioscience Tools). (Left) Configuration of Biosciencetools heating objective collar and external temperature probe placed in sample immersion oil on an upright microscope setup (in experiments, an inverted microscope is used). (Middle) Temperature readout from external temperature probe immediately after an increase in set temperature from 33.4 °C to 33.8 °C. Temperature fluctuations stabilize after about 60 seconds from the start of the temperature change. (Left) Temperature readout from external temperature probe several minutes after a temperature change. Note fluctuations of  $\pm 0.03^{\circ}\text{C}$ .

#### 3.3.1.4 Monolayer Formation

With temperature fluctuations and formulation issues resolved, we were able to develop a consistent method for creating the samples (Fig. 3.3). After a sample was placed on the inverted microscope objective, the sample was heated to a temperature corresponding to the aggregation regime. We then allow at least 10 minutes for 3D particle aggregates to form and sediment to the bottom surface of the objective. The sample is then heated to  $0.1^{\circ}\text{C}$  above the water-lutidine phase separation temperature for just enough time for a monolayer to spread on the bottom surface (typically 3-10 seconds). The system is then cooled back to the original aggregation temperature, forming an attractive monolayer of particles. Depending on the initial concentration of colloids in suspension, the resulting monolayer packing can resemble a sparse, barely percolating structure with area fraction  $\phi = 0.50 \pm 0.01$  or a homogeneous, dense packing with area fraction  $\phi = 0.84 \pm 0.01$

#### 3.3.2 vDOS Calculation from Particle Trajectories

In contrast to previous studies which calculate the vDOS of crystalline packings by assuming plane-wave behavior [74] or calculate vDOS from particle velocity autocorrelations which lose all spatial information [163, 166], we calculate vibrational modes directly from correlations of particle displacements with respect to their equilibrium positions [18, 43, 54, 72].

To gain a fundamental understanding of this method, first imagine a single thermal particle in  $N$ -dimensional space with coordinates  $x_1, x_2, \dots, x_N$  sitting in a potential  $V(x_1, x_2, \dots, x_N)$ . As this particle explores  $N$ -dimensional space, its likelihood of being at any position will be related to the underlying potential. By analyzing the statistics of particle positions in  $N$ -dimensional

space over a long enough time, we can derive the shape of the underlying potential in the  $N$ -dimensional space.

The physics of  $N$  particles in  $d$  dimensions interacting via multiple inter-particle potentials can be derived in a similar manner by understanding the system as a single “configuration particle” exploring  $N \times d$  dimensional space. Say, for example, we have a system of three particles confined to a single dimension at positions  $x_i$  and interacting via inter-particle potentials between particles  $i$  and  $j$ ,  $V_{ij}(x_i, x_j)$ . We can re-interpret the entire system as a “kind of” single particle moving in three dimensions  $x_1, x_2, x_3$  in a three-dimensional potential  $V(x_1, x_2, x_3) = V_{12} + V_{23} + V_{13}$ . By observing sufficient numbers of configurations of the three particles over time, we can thus map out the three-dimensional potential  $V(x_1, x_2, x_3)$  which describes the entire system.

Likewise, by observing the positions of particles in an  $N$ -particle packing at many different times, we can map out a  $N \times d$  - dimensional potential which describes the system. From this, we can calculate the vibrational modes of our system. This approach offers us an advantage over some other methods for calculating vibrational modes. For example, we do not require the high frame-rates and the tracking precision necessary for determination of instantaneous particle velocities. Additionally, we can extract vibrational information about our packings without knowing the exact details of the inter-particle potentials *a priori*.

We follow previous experimental work calculating vibrational modes from particle trajectories [18, 43, 54, 72]. Given a 2D colloidal system of  $N$  particles in thermal equilibrium, we define a displacement vector  $\mathbf{u}$  for the system such that  $\mathbf{u} = [dx_1, dx_2, \dots, dx_N, dy_1, dy_2, \dots, dy_N]$ , where  $dx_1$  and  $dy_1$  are particle 1’s  $x$  and  $y$  displacements from its average/equilibrium position,

$dx_2$  and  $dy_2$  are particle 2's  $x$  and  $y$  displacements from its average/equilibrium position, *etc.* We then calculate a time-averaged covariance matrix of these displacements  $C_{ij} = \langle u_i(t)u_j(t) \rangle_t$ . In the harmonic approximation, the  $2N$ -dimensional inter-particle potential  $V$  is given by the relation

$$V = \frac{1}{2} \mathbf{u}^T \mathbf{K} \mathbf{u}, \quad (3.1)$$

where  $K$  is the  $2N$  by  $2N$  matrix of effective spring constants between all pairs of particles, with elements defined as:

$$K_{ij} = \frac{\partial^2 V}{\partial u_i \partial u_j}. \quad (3.2)$$

This form of the  $2N$ -dimensional potential  $V$  yields a partition function of

$$Z \propto \int d\mathbf{u} e^{-\beta(\frac{1}{2} \mathbf{u}^T \mathbf{K} \mathbf{u})}, \quad (3.3)$$

where  $\beta = 1/k_B T$ . Calculating the correlation function from this partition function yields  $C_{ij} = k_B T (K^{-1})_{ij}$ , or equivalently,  $K_{ij} = \beta (C^{-1})_{ij}$ . Thus, in the harmonic approximation, the equation of motion for a “shadow system” of particles with the same interactions as our system, but without damping, is

$$\ddot{\mathbf{u}} + \mathbf{D} \mathbf{u} = \mathbf{0}. \quad (3.4)$$

Here  $D_{ij} = K_{ij}/m_{ij}$  is the  $2N$  by  $2N$  dynamical matrix of the system, and  $m_{ij} = \sqrt{m_i m_j}$ , where  $m_i$  is the mass of particle  $i$ . We thus find the  $i^{\text{th}}$  vibrational mode of this shadow system by solving for the eigenvectors of  $D_{ij}$ :  $\mathbf{D} \mathbf{e} = \lambda \mathbf{e}$ , with the frequencies of these modes given by  $\omega_i = \sqrt{\lambda_i}$ . The components of the eigenvector of mode  $i$ ,  $e(\omega_i)_{jx}$ , represent the relative

participation of particle  $j$  moving along the  $x$  direction in mode  $i$  with frequency  $\omega_i$ .

After calculating the  $\omega$  values, we derive the vibrational density of states by creating a histogram of these modes as a function of  $\omega$ . In order to compensate for varying statistics at different frequencies, we calculate each point on the vDOS curve from  $M$  consecutive modes (typically). For a set of  $M$  modes of consecutive frequency  $[\omega_i, \omega_{i+M}]$ , we define  $\omega_{avg,i} = (1/M)\sum_j = i^i + M\omega_j$ . We then define the corresponding vDOS value at frequency  $\omega_{avg,i}$  as  $M/(\omega_{i+M} - \omega_i)$ .

### 3.3.3 Analytical Considerations for vDOS calculations

After acquiring bright-field microscopy video of the 2D samples, i.e., images of a  $60 \mu\text{m} \times 80 \mu\text{m}$  section of the packing (1500-3000 particles, depending on  $\phi$ ) at 60 frames per second, we use sub-pixel particle tracking algorithms to calculate each particle's trajectory [26]. To negate any drift in the sample and to study the collective motion of areas smaller than the full field-of-view, we subtract the average motion of all particles between time frames.

Though there are no obvious particle displacements greater than a fraction of a particle diameter in these tracks, there may be collective "irreversible" particle rearrangements wherein particles shift position. These motions are not equilibrium vibrations of the system; rather, they are rearrangements which evolve the system to an entirely new packing. In fact, the vDOS analysis we have described above will, strictly speaking, only work if there are no internal rearrangements during the measurement time. Even though there might not seem to be any noticeable change in the structure of the packing, these rearrangements will be interpreted by the vDOS analysis (described above) as low-frequency modes. Since low-frequency modes are important features for characterizing glassy and disordered packings, it is important that such errors in the

mode calculation are minimized. This minimization of error entails careful selection of regions of particle tracks without observable rearrangements.

Our primary data includes tracks of 30,000 - 100,000 time frames at 60 fps (8 - 28 minutes). For processing, we typically select only the 10,000 frame region of the track with the slowest, most consistent average motion. While this data selection effectively decreases the statistics for our vDOS calculation, it gives us confidence in the low-frequency shape of the vDOS curves, etc. Previous work has shown that vDOS curves will deviate from their ideal shape if the number of frames used to calculate modes,  $N_f$ , is less than  $5N_p$ , where  $N_p$  is the number of particles in the system [43]. Though shortening the number of frames affects the higher frequency modes (which, as stated in the previous paragraph, are not quite as important in our analysis as the low-frequency modes), we can readily perform a fit that compensates for low statistics by linearly extrapolating eigenfrequencies to their expected values, i.e., which would be derived from an infinitely long time-track [20, 47, 141, 147]. Specifically, we calculate the vibrational modes for several different numbers of time frames  $N_f$  (ranging from 6,000 to 10,000). As can be seen from Fig. 3.6,  $1/\omega$  exhibits a linear trend with  $1/N_f$ , with larger slopes at high frequencies. By fitting a line to each trend and extracting the infinite frame limit, i.e., the predicted  $\omega(1/N_f = 0)$  value for each mode, then we can estimate an adjustment to derive the infinite time-frame limit frequency for each mode. Data post-processed with this procedure results in sharper, higher frequency peaks in the vDOS, while the low-frequency tail of the vDOS, though slightly improved, remains largely unchanged.

A preliminary observation of vDOS curves (normalized by the total number of modes in the system) reveals high-frequency peaks occurring at different frequencies (Fig. 3.7). These shifts

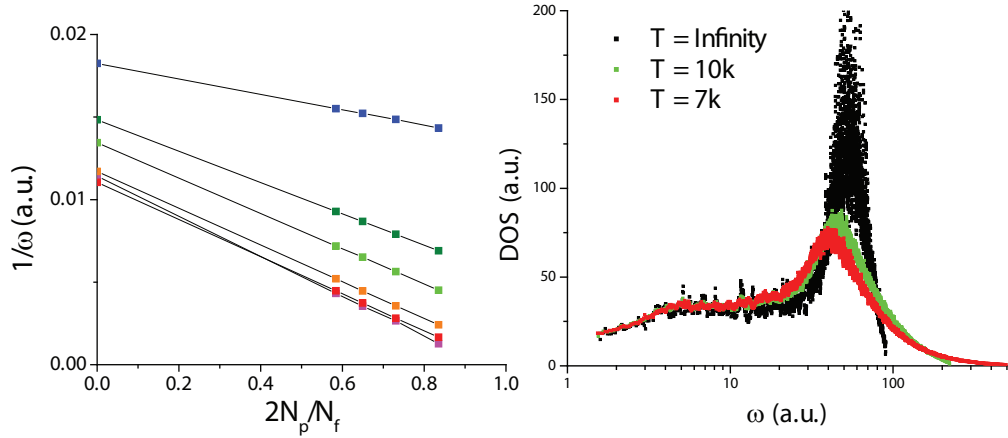


Figure 3.6: Extrapolation of modes to compensate for low statistics in a packing with area fraction  $\phi = 0.84$ . (Left)  $1/\omega$  of several modes calculated for several ratios of  $N_p/N_f$ , with linear fits extrapolating these modes to the limit of  $N_p/N_f = 0$ . (Right) vDOS calculated for  $N_f = 7000$  (red points),  $N_f = 10000$  (green points), and extrapolation  $N_f \rightarrow \infty$  (black points). Note the increasingly better statistics do not significantly influence the vDOS curve shape at low frequencies.

are most likely due to slight changes in the ratio of large to small particles in each packing. Though initial mixtures of colloids were made to have an equal number of large ( $d = 1.4 \mu\text{m}$ ) and small ( $d = 1.0 \mu\text{m}$ ) particles, the exact ratio varies significantly from sample to sample. To enable optimal comparison between packings, we normalize phonon frequencies by the mean frequency of that particular packing  $\bar{\omega}$ . After this normalization, the vDOS peaks overlap nicely at  $\omega/\bar{\omega} = 1.0$  (as can be seen in Fig. 3.12). A similar re-scaling is performed in [48] to account for changes in local packing fraction.

## 3.4 Results and Discussion

### 3.4.1 Conventional Structural Characteristics of Attractive Monolayers

We examine 13 different packings with area-fractions ranging from  $\phi = 0.50$  to  $\phi = 0.84$  (specifically,  $\phi = 0.50 \pm 0.1, 0.55 \pm 0.1, 0.56 \pm 0.1, 0.62 \pm 0.1, 0.64 \pm 0.1, 0.65 \pm 0.1, 0.69 \pm 0.1, 0.74 \pm$

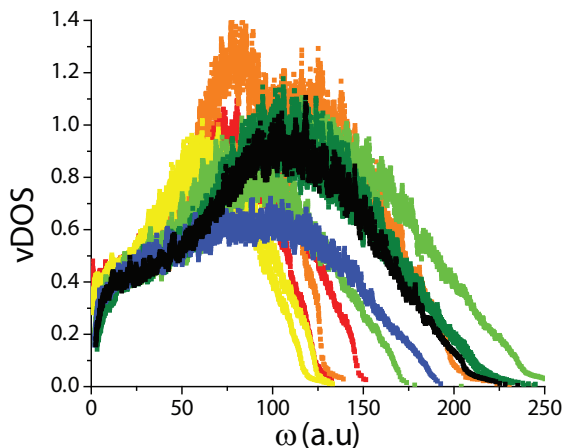


Figure 3.7: vDOS curves of observed packings against unnormalized frequencies on a linear scale. Notice shifts in the location of the high-frequency peak from packing to packing. (Red,  $\phi = 0.50 - 0.55$ ; Orange,  $\phi = 0.56 - 0.62$ ; Yellow,  $\phi = 0.64 - 0.65$ ; Green,  $\phi = 0.69 - 0.74$ ; Olive,  $\phi = 0.80$ ; Blue,  $\phi = 0.81 - 0.82$ ; Black,  $\phi = 0.84$ ).

0.1,  $0.80 \pm 0.1$ ,  $0.80 \pm 0.1$ ,  $0.81 \pm 0.1$ ,  $0.82 \pm 0.1$ , and  $0.84 \pm 0.1$ ). By analyzing the equilibrium positions of particles with common structural parameters, a discontinuous change in structure with area fraction is not immediately apparent. For example, as packings become continuously more spatially heterogeneous with decreasing  $\phi$ , the pair correlation functions  $g(r)$  remain qualitatively similar (see Fig. 3.10).

Additionally, we find that the average coordination of particles in these packings decreases fairly linearly with volume fraction (Fig. 3.11). We determine nearest neighbors by identifying those particles whose equilibrium positions are closer than the “dip” after the first  $g(r)$  peak associated with that particular particle pair. This linear change in coordination number with volume fraction can be modeled by the removal of particle clusters from a dense packing. Indeed, if we start with our densest observed packing ( $\phi = 0.84 \pm 0.1$ ) and randomly remove adjacent particle clusters of 5 particles, and then re-calculate the average coordination number, we observe a trend very similar to what we observe in experiment. Thus, though each experimental sample is

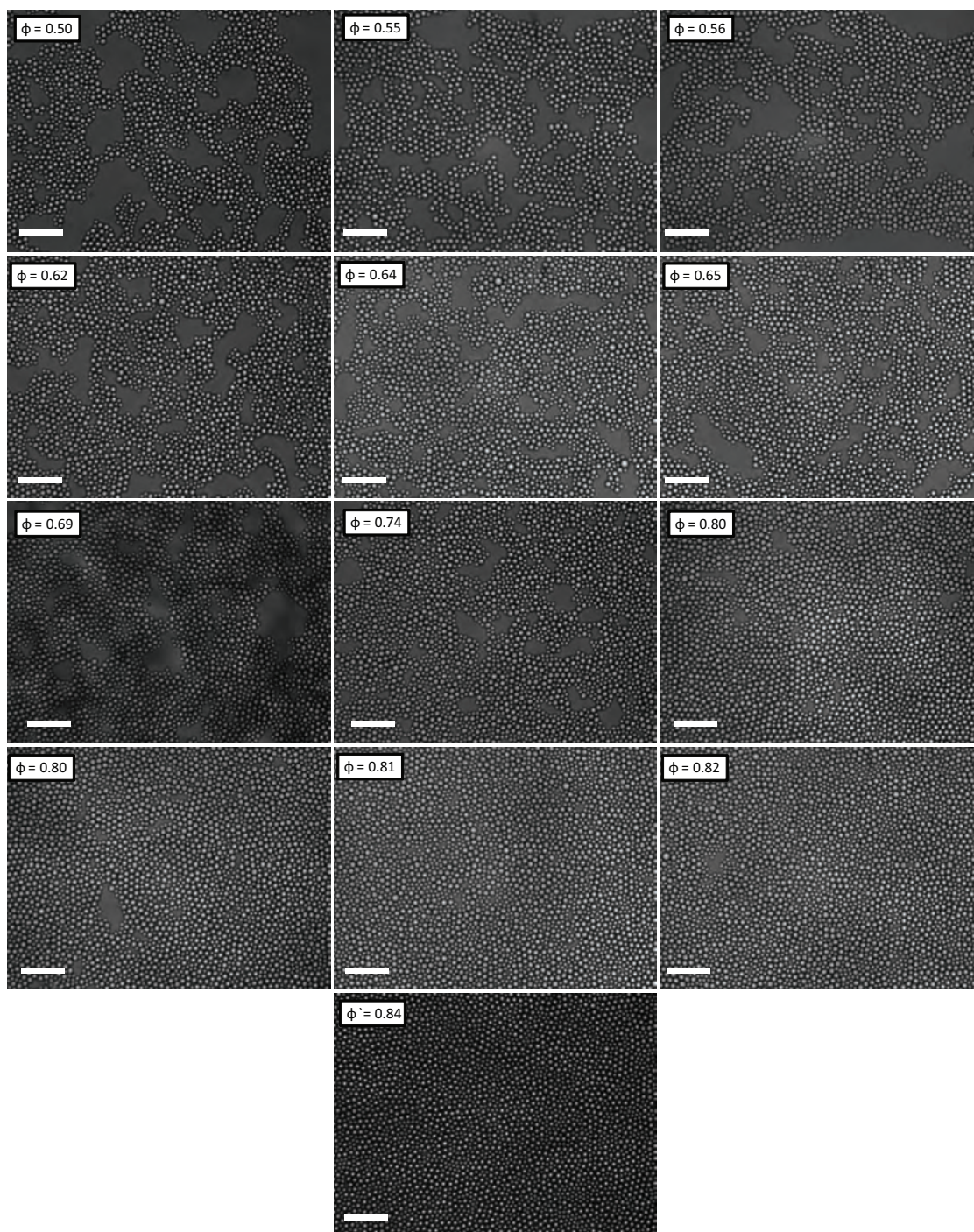


Figure 3.8: Unprocessed bright-field microscopy images of investigated bidisperse attractive PS monolayer packings at various densities. Approximate area fraction  $\phi$  indicated by inset. Scale bar =  $10\mu\text{m}$ .

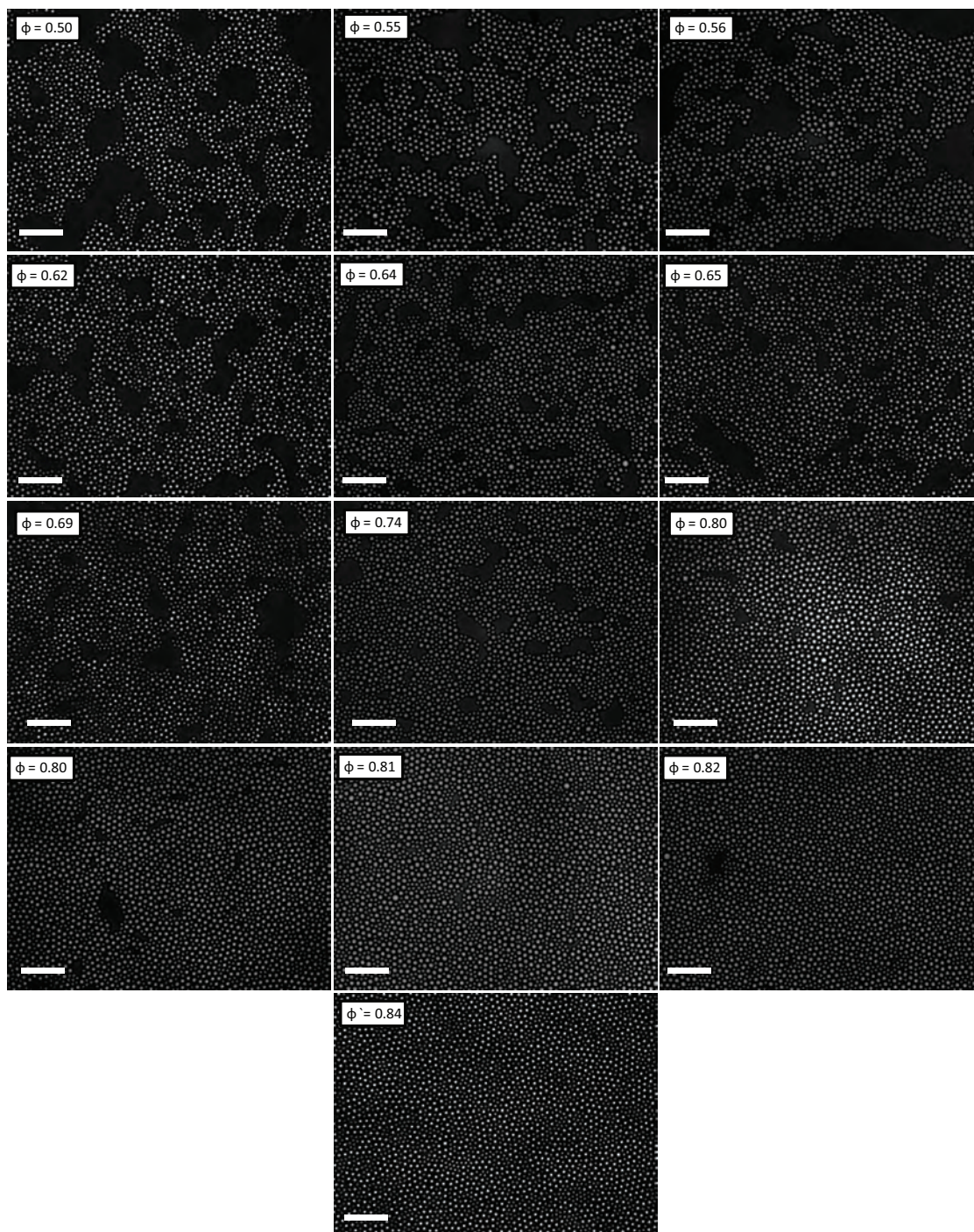


Figure 3.9: Bright-field microscopy images of investigated bidisperse attractive PS monolayer packings at various densities, with contrast and brightness enhanced for clarity. Approximate area fraction  $\phi$  indicated by inset. Scale bar =  $10\mu\text{m}$ .

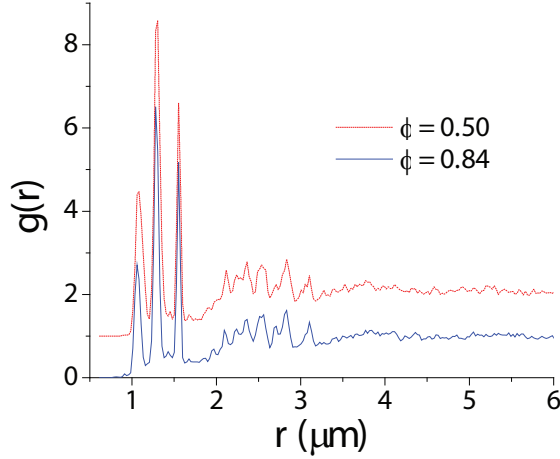


Figure 3.10: Pair correlation function  $g(r)$  of densest ( $\phi = 0.84$ , blue solid line) and sparsest ( $\phi = 0.50$ , red dotted line) observed packings. Sparse packing  $g(r)$  shifted vertically by  $+1.0$  for clarity.

prepared separately through a non-equilibrium process, the morphology across samples appears consistent enough to merit comparison.

### 3.4.2 vDOS Shape as a Signature of Structural Transition

The resulting vibrational densities of states (vDOS) for the observed packings demonstrates a pronounced variation in the distribution of low-frequency modes with respect to changes in packing concentration (Fig. 3.12). Specifically, a drastic increase in the presence of low-frequency modes in the sparser packings ( $\phi < 0.67$ ) indicates a crossover from a glassy to a gel-like state.

Though all vDOS plots show a peak at the mean frequency  $\bar{\omega}$  and a plateau at slightly lower frequencies ( $0.1 < \omega/\bar{\omega} < 0.4$ ), one of two behaviors is seen at the lowest observed frequencies ( $\omega/\bar{\omega} < 0.1$ ). For all packings with  $\phi > 0.67$ , the density of states decreases with decreasing frequency, while for all packings with  $\phi < 0.67$ , the density of states increases with decreasing frequency. The general shape of the vDOS curve for denser packings qualitatively resembles

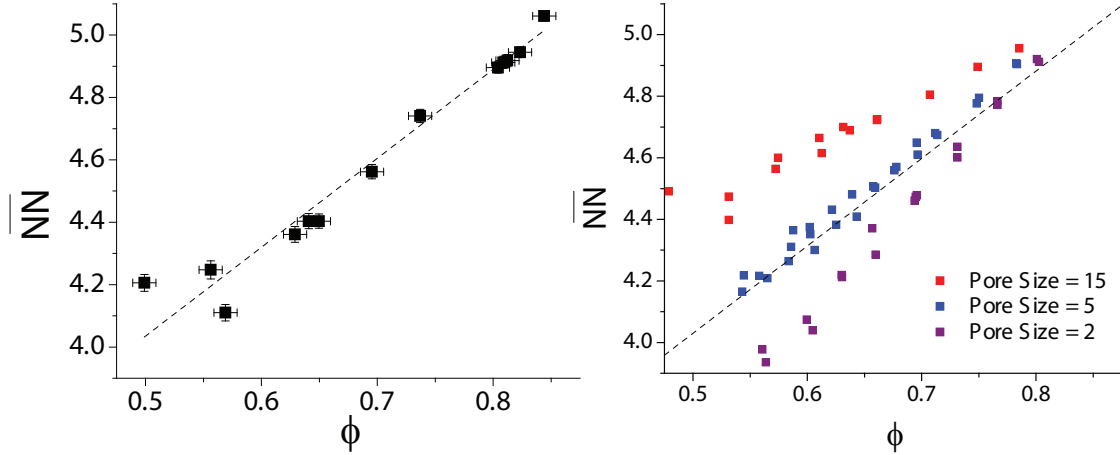


Figure 3.11: (Left) Average number of nearest neighbors as a function of  $\phi$  for experimentally observed packings, with a linear fit. (Right) Nearest neighbors vs.  $\phi$  calculated for the particle positions of the observed  $\phi = 0.84$  packing, with clusters of 2, 5 or 15 particles randomly removed. The dashed line is from the fit of experimental data on the left.

the vDOS for a model packing slightly above the jamming transition [118, 169]; it has a high-frequency peak, a plateau, and a drop off below a characteristic frequency. While this result might be expected for the densest, spatially uniform (but disordered) packings, it is surprising that this result extends to samples with observable gaps, holes and spatial heterogeneity larger than a single particle diameter (see packing structures at  $0.69 < \phi < 0.80$  in Fig. 3.8).

Indeed, the vDOS of sparser packings does not closely resemble a conventional dynamically arrested packing mode distribution. The vDOS increases for  $\omega/\bar{\omega} < 0.1$ . In simulations of uniform glassy packings in stable “lowest density” configurations, a dropoff at low frequencies is not always observed [118, 169]. However, in these simulations, the vDOS remains at the same plateau value observed at intermediate frequencies (for our experiments, this range of frequencies is for  $0.1 < \omega/\bar{\omega} < 0.4$ ). An increase in vDOS above this plateau value is thus not previously observed, nor easily understood, in the context of uniform packings.

Additionally, the low-frequency vDOS curves have similar slopes for all sparse ( $\phi < 0.67$ )

and dense ( $\phi > 0.67$ ) packings, with no apparent monotonic changes in slope as a function of  $\phi$ . This property indicates that this appearance of additional low-frequency modes is likely not directly related to continuous changes in density, coordination number, and/or spatial heterogeneity.

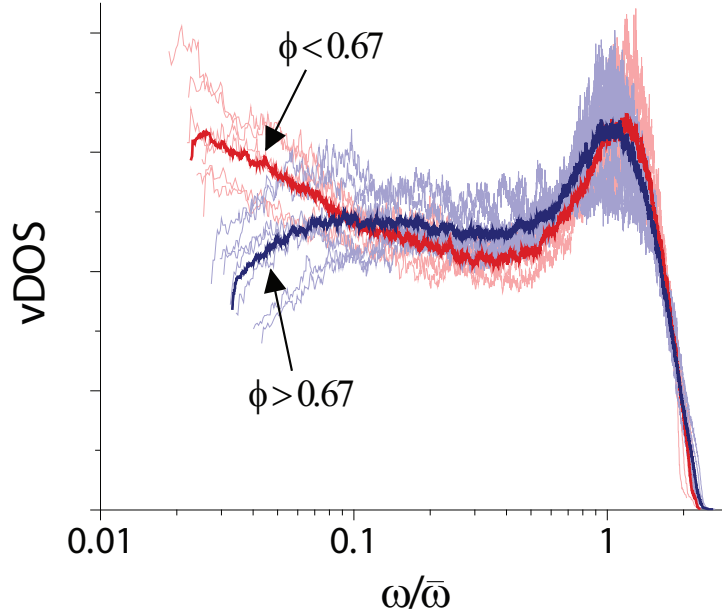


Figure 3.12: Vibrational density of states as a function of frequency  $\omega$  calculated from eigenmode distributions in packings with  $\phi < 0.67$  (i.e., six packings with  $\phi = 0.50, 0.55, 0.56, 0.62, 0.64,$  and  $0.65,$  each  $\pm 0.1$ ) (red lines) and  $\phi > 0.67$  (i.e., seven packings with  $\phi = 0.69, 0.74, 0.80, 0.80, 0.81, 0.82,$  and  $0.84,$  each  $\pm 0.1$ ) (blue lines). Thin, faded lines indicate vDOS for individual packings; thicker lines are the average vDOS for all packings in the sparse ( $\phi < 0.67,$  red) and dense ( $\phi > 0.67,$  blue) regimes.

### 3.4.2.1 Comparison of vDOS in Dense Packing to Simulations

In this subsection, we compare the observed vDOS with the vibrational modes calculated from simulations of dense, short-range repulsive hard sphere packings, following methods similar to [45]. We find that the resulting simulated vDOS curves resemble the shape of the experimental vDOS curves calculated from dense packings. This correspondence confirms the validity of

our analytical methods for capturing the qualitative vDOS for the better-understood, spatially uniform packings.

The simulated packings are created by randomly placing 3000 bidisperse disks in a box with periodic boundary conditions and evolving their positions to minimize the total interaction energy of the system. Inter-particle bonds and interactions are then defined by the overlap of particles. All “floppy” particles with insufficient bonds to create local stability are removed from the packing; this removal ensures an entirely rigid packing is produced without zero-frequency modes. From the remaining particle overlaps, one creates a interaction matrix  $K_{ij}$  from which the vibrational modes can be calculated according to the method outlined in Section 3.3.2.

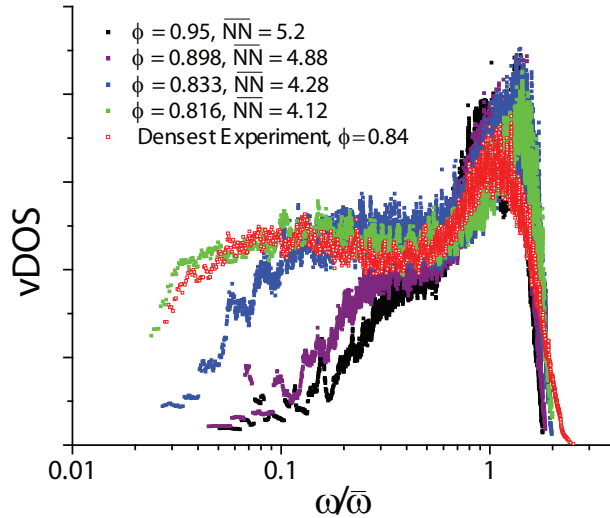


Figure 3.13: vDOS curves from simulated dense, uniform bidisperse packings ( $\phi = 0.95$ , black;  $\phi = 0.898$ , purple;  $\phi = 0.833$ , blue;  $\phi = 0.816$ , green), along with an experimentally calculated vDOS curve from the densest observed packing ( $\phi = 0.84$ , red curve). Nearest neighbors determined by particle overlap in simulation indicated in the legend.

As noted in previous work, all simulated packings show a vDOS peak at high-frequency, a plateau at intermediate frequencies, and a drop off below a characteristic  $\omega^*$ , which scales with the “distance” of the packing from isostaticity (in 2D hard sphere packings,  $Z_c = 4$ ) [118,

169]. In Fig. 3.13, we compare simulated vDOS curves at different densities to the most dense packing observed in experiment. A relatively sparse (though still uniform) simulated packing with average coordination number of  $\overline{NN} = 4.12$  yields the most similar vDOS curve to the most spatially uniform packing from experiment ( $\phi = 0.84$ ). The average nearest neighbor coordination calculated from  $g(r)$  peaks for the densest experimental packing is  $\overline{NN} \approx 5.0$ . It is surprising that though these curves have very similar vDOS curves, since they have a very different number of bonds per particle. This difference could be due to the  $g(r)$  method for calculating bonds overestimating the bond density in our experiments.

It is worth noting that, though changing the average coordination number has a dramatic effect on the shape of the vDOS curves in simulations, this effect is not observed in spatially heterogeneous attractive-colloid experimental samples with  $\phi > 0.67$ . These differences could also be due to the definition of “bonds” used in our experimental analysis. While the  $g(r)$  method for defining bonds yields expected results in the analysis of modes in small clusters [179, 180], this “effective” bond definition may not be sufficient for comparison with larger, denser simulated packings. Additionally, the interactions in simulations are short-range repulsive, instead of short-range attractive; these differences could cause significant changes in the predicted vDOS as well.

In short, well-used simulation techniques for studying dense glassy packings qualitatively reproduce the vDOS curves we calculate in our densest experimental sample. Though there are some noticeable differences between these simulations and our experiments, this finding gives us confidence that our method for calculating vDOS produces reasonable results.

### 3.4.3 Localization of Low-Frequency Modes

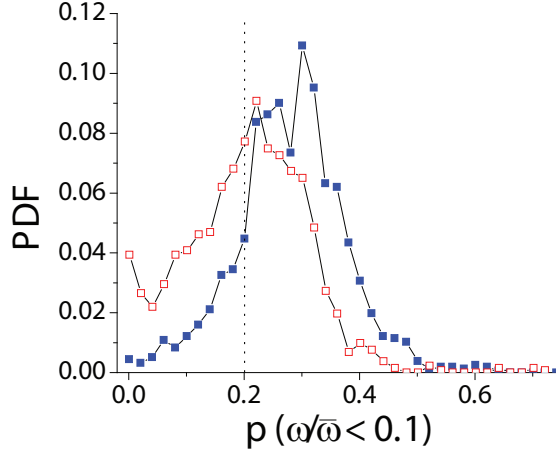


Figure 3.14: Histogram of participation ratio  $p(\omega)$  for low-frequency modes ( $\omega/\bar{\omega} < 0.1$ ) for packings with  $\phi < 0.67$  (open red squares) and  $\phi > 0.67$  (closed blue squares). Dashed line indicates  $p = 0.2$  cutoff for vDOS re-calculations.

Quantification of the spatial distribution of low-frequency modes provides insight into the structural nature of the  $\phi$ -mediated change in the vDOS curve. Specifically, we find that the increase in low-frequency modes in sparse packings can be attributed to the appearance of highly localized modes. These modes appear to be highly localized to individual or small clusters of particles which have only a few nearest neighbors.

We find the relative localization of each mode by calculating its participation ratio  $p(\omega_n) = (\sum_i |\vec{e}_i(\omega)|^2)^2 / (\sum_i |\vec{e}_i(\omega)|^4)$ . This parameter has a value close to 1 for extended modes, and lower values when modes are localized. When we compare the distributions of  $p$  in low-frequency modes ( $\omega/\bar{\omega} < 0.1$ ) for different packings, it is apparent that sparser packings have more modes with lower  $p$  (Fig. 3.14). Equivalently, these sparser packings have more highly localized low-frequency modes than their denser counterparts. To determine how these highly localized modes contribute to the shape of the vDOS curves, we re-calculate the density of states

for both sparse and dense packings, but this time we neglect all modes with a  $p < 0.2$  (Fig. 3.15). While the shape of the vDOS curves for dense packings remains largely unchanged, the low-frequency vDOS increase observed in sparse packings disappears, yielding curves similar in shape to those of the denser packings. This observation implies that the excess of low-frequency modes seen in sparse packings arises exclusively from the prevalence of highly localized vibrational modes.

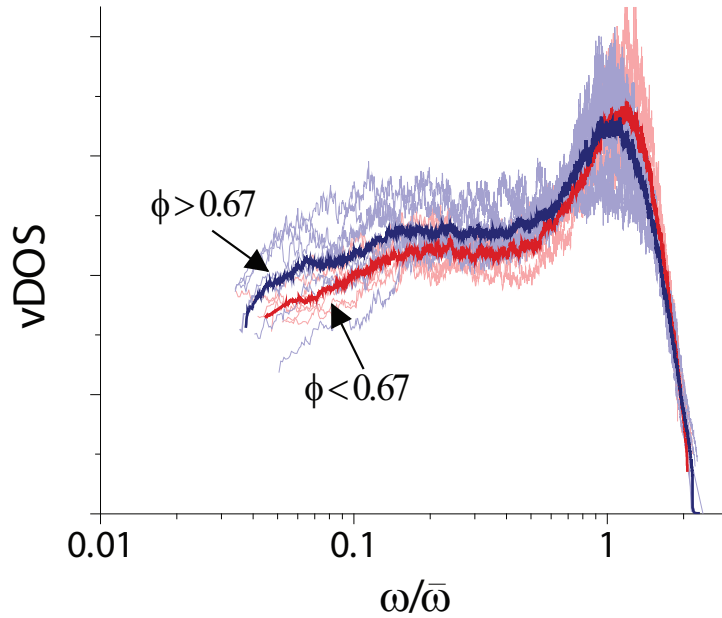


Figure 3.15: Vibrational density of states re-calculated discounting highly localized modes ( $p < 0.2$ ) as a function of frequency  $\omega$  calculated from eigenmode distributions in packings with  $\phi < 0.67$  (i.e., six packings with  $\phi = 0.50, 0.55, 0.56, 0.62, 0.64,$  and  $0.65$ , each  $\pm 0.1$ ) (red lines) and  $\phi > 0.67$  (i.e., seven packings with  $\phi = 0.69, 0.74, 0.80, 0.80, 0.81, 0.82,$  and  $0.84$ , each  $\pm 0.1$ ) (blue lines). Thin, faded lines indicate vDOS for individual packings; thicker lines are the average vDOS for all packings in the sparse ( $\phi < 0.67$ , red) and dense ( $\phi > 0.67$ , blue) regimes.

By closely examining the distribution and placement of the localized vibrations in the sparse packings, we gain insight into the structural features associated with these modes. We observe a qualitative difference in mode distributions in the same packing with similar frequencies, but

with significantly different participation ratio (Fig. 3.16). Specifically, a mode with lower  $p$  appears concentrated to fewer particles with greater local participation. In other words, low  $p$  vibrations appear to be localized to small clusters of particles.

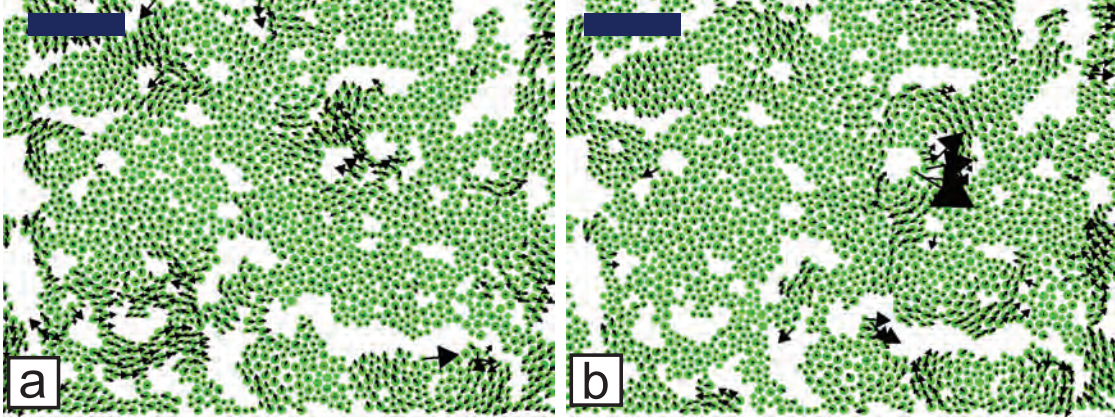


Figure 3.16: Plots of particle locations from a sparser packing ( $\phi = 0.64 \pm 0.01$ ) overlaid with polarization eigenvector components corresponding to two modes with similar frequency ( $\omega/\bar{\omega} = 0.019$  (a) and  $0.021$  (b)) and significantly different localization ( $p(\omega) = 0.32$  (i.e., a more extended mode) (a), and  $p(\omega) = 0.069$  (i.e., a more localized mode) (b)). Scale bar =  $10\mu\text{m}$ .

We observe this degree of localization more quantitatively by looking at the distribution of single-particle eigenvector component magnitudes,  $|\vec{e}_i(\omega)|$ . These distributions for extended ( $p > 0.2$ ) and localized ( $p < 0.2$ ) modes at low frequencies ( $\omega/\bar{\omega} < 0.1$ ) are plotted in Fig. 3.17. It can be seen that the peak  $|\vec{e}_i(\omega)|$  value does not change much between extended and localized modes. The major difference is seen in component values an order of magnitude greater than this peak value. Modes with  $p > 0.2$  show a probability distribution function (PDF) that drops off with a nearly exponential tail. Modes with  $p < 0.2$ , however, show a significant increase in the presence of high-participation particles above a value of  $|\vec{e}_i(\omega)| = 0.1$ .

By identifying particles which “dominate” in spatially localized, low-frequency modes, we identify geometries and structures which influence the low-frequency vDOS. In Fig. 3.18, we

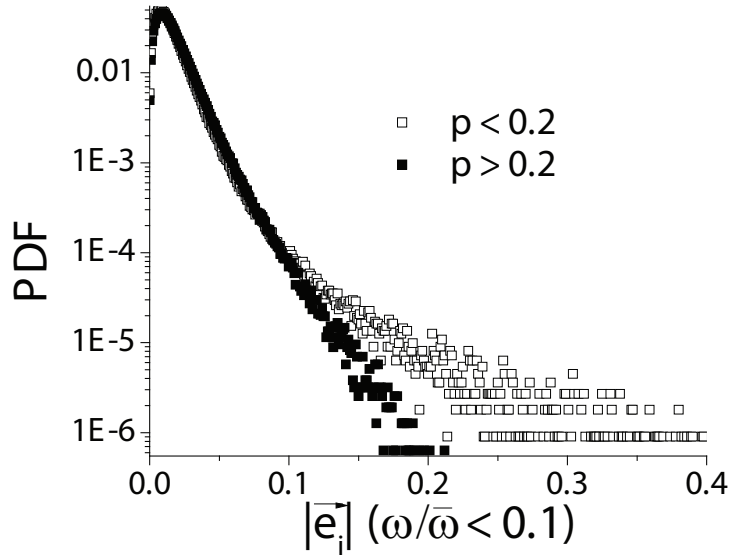


Figure 3.17: Histograms of  $|e_i(\omega)|$  for all modes with  $\omega/\bar{\omega} < 0.1$  in all observed packings with  $\phi < 0.67$  for extended ( $p > 0.2$ , solid squares) and localized ( $p < 0.2$ , empty squares) modes.

plot the distribution of cluster sizes of these particles. For the most part, it appears these “dominating” modes are centered around single particles, or around and within clusters smaller than a few particles. A telling feature of the structure surrounding these particles is each particle’s local bond number. A histogram in Fig. 3.18 compares the number of nearest neighbors of all particles in sparse packings to those of particles which dominate the localized, low-frequency modes. This comparison shows that these “dominating” particles have relatively low-coordination, with a peak at  $NN = 2$ .

### 3.4.4 Qualitative Description of Structural Correlations to Localized Low-Frequency Modes

After deriving a correlation between particles with few nearest neighbors and those in localized, low-frequency modes appearing in the sparse packings, we attempt to explain the correlation and clarify the precise geometries surrounding these particles. We hypothesize and give a qualitative

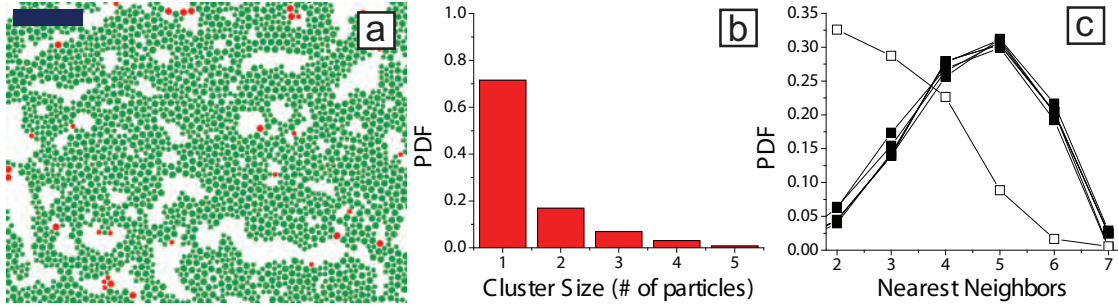


Figure 3.18: (a) Plot of particle locations in a  $\phi = 0.64 \pm 0.01$  packing, with particles which have  $|e_i(\omega)| > 0.2$  for any mode where  $\omega/\bar{\omega} < 0.1$  highlighted in red. Scale bar =  $10 \mu\text{m}$ . (b) Histogram of size of clusters of particles which dominate a low-frequency mode in sparse packings ( $|e_i(\omega)| > 0.2$ ,  $\omega_n/\bar{\omega} < 0.1$ ,  $\phi < 0.67$ ). (c) Histogram of nearest neighbors per particle of each packing with  $\phi < 0.67$  (black points) and for particles in all sparse packings which dominate a low-frequency mode (empty squares,  $|e_i(\omega)| > 0.2$ ,  $\omega_n/\bar{\omega} < 0.1$ ).

explanation for why particles in “bridging” structures could give rise to such modes. However, quantification of such structures does not yield a one-to-one correlation with particles dominating localized low-frequency modes. The structural nature of these vibrations is more complicated than they initially appear.

The localization of low energy vibrational modes at particles with low-coordination is a result consistent with basic intuition, as well as with recent work studying vibrational modes in related systems [28, 139, 179, 180]. Fewer constraining bonds on a particle leads to lower confining energies, which would logically result in lower-frequency localized modes. Additionally, experimental work has shown that the mean frequency of modes in small colloidal clusters scales with their average coordination number [179]. Similarly, recent simulations of sparse gels of “patchy” particles demonstrate an increase in low-frequency modes in packings with increasing sparsity, which is related to the appearance of low-energy transverse vibrations in linear particle chains [139].

By highlighting particles which dominate localized low-frequency modes in sparse packings

(as in Fig. 3.18), we obtain an indication that low-frequency modes are often localized to linear structures susceptible to such low-energy transverse vibrations. Such an observation is consistent with work that characterizes the boson peak frequency in glassy packings as an upper limit of transverse modes [143, 153]. Under this assumption, the low-area fraction emergence of poorly coordinated structures susceptible to localized transverse vibrational modes would only effect the shape of the vDOS curve below a characteristic frequency, as seen in Fig. 3.12.

A specific recurring structure of these “dominators” is a single particle bridging two non-adjacent particles. Qualitative observations of eigenmodes localized at such particles reveal large-amplitude fluctuations perpendicular to the local bonding of particles. A qualitative understanding of localized low-frequency modes emerging from such “bridge” structures can be gleaned from a comparison of longitudinal and transverse modes in such a geometry. Given a line of three particles along the  $x$  direction with harmonic spring interactions of strength  $k$ , and with an inter-particle spacing  $r$  (as depicted in Fig. 3.19), the energy cost of a longitudinal displacement of the center particle from its equilibrium position,  $\delta x$ , is given as

$$U(\delta x) = k(\delta x)^2. \tag{3.5}$$

A significantly small transverse deformation of the same magnitude,  $\delta y \ll r$  will have a significantly lower energy cost,

$$\begin{aligned}
 U(\delta y) &= 2 \left( \frac{1}{2} k \sqrt{r^2 + (\delta y)^2} - r \right)^2 \\
 &= k \left( -r + r \left( 1 + \frac{1}{2} \left( \frac{\delta y}{r} \right)^2 - \frac{1}{8} \left( \frac{\delta y}{r} \right)^4 \right) \right)^2 \\
 &= \frac{k}{4} \frac{(\delta y)^4}{r^2} + O(\delta y)^6.
 \end{aligned} \tag{3.6}$$

The resulting energy cost of a transverse deformation is not only drastically lower than that of the longitudinal deformation; in fact, the energy cost is negligible in the harmonic approximation! Thus, it makes sense that such structures would create low-frequency (that is, low energy) transverse vibrations that do not necessitate movement of adjacent particles.

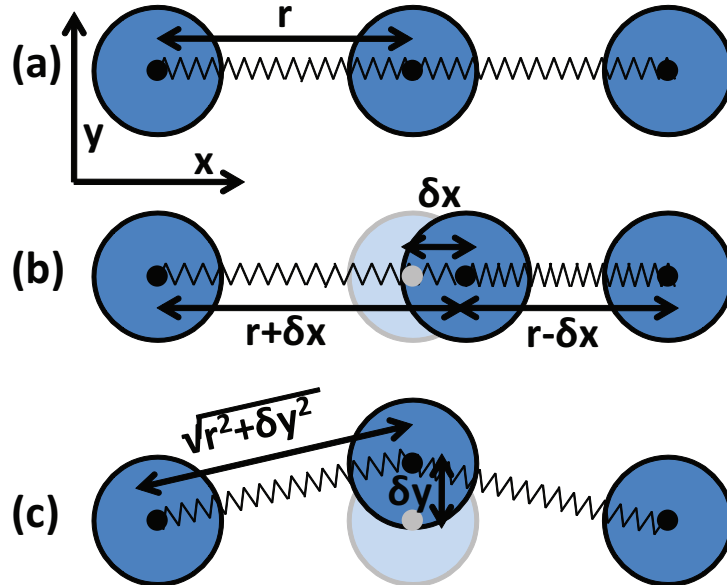


Figure 3.19: Illustration of single-particle deformations in a linear chain of particles, showing a particle with two neighbors in a line connected by springs (a) at its equilibrium position, with inter-particle spacing  $r$ , (b) under a longitudinal deformation of size  $\delta x$ , and (c) under a transverse deformation of size  $\delta y$ .

However, such low-coordination, “dangling” structures do not account for all highly localized modes in these packings. As can be seen in Fig. 3.18, locally rigid particles with up to 4 nearest neighbors can exhibit highly localized low-frequency modes. Additionally, not all particles with a locally linear structure contribute to highly localized, low-frequency modes. We can identify such locally linear structures using a local linear order parameter  $\psi_{2i} = \frac{1}{NN} \sum_{j=NN} \exp(-i2\theta_{ij})$ , where  $\theta_{ij}$  is the angle between a given direction and the bond between particles  $i$  and  $j$ . Particles with a high  $|\psi_{2i}|$  exist in locally linear structures, with the local linear orientation of neighbors given by the complex phase of  $\psi_{2i}$ . As can be seen by comparing Fig. 3.20 to Fig. 3.18, not all particles with local linear structure necessarily exhibit highly localized, low-frequency vibrational modes.

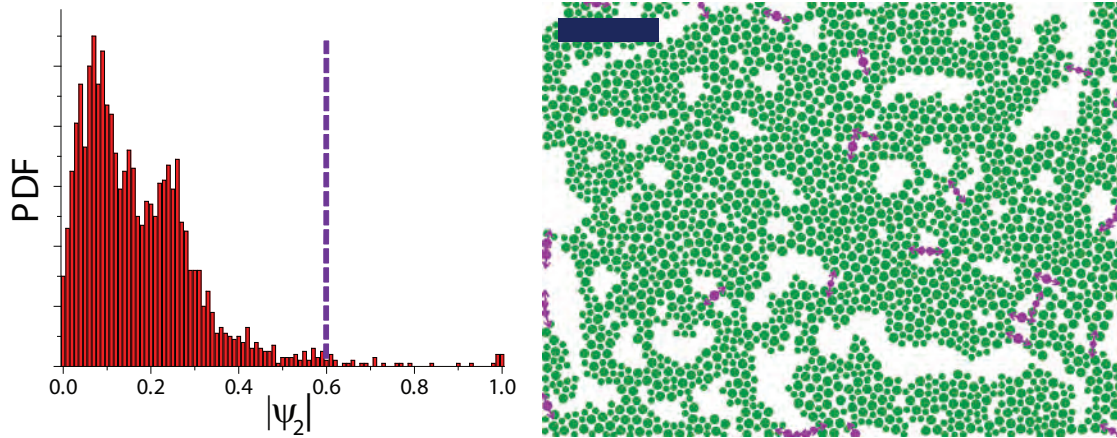


Figure 3.20: Characterization of linear structure distribution in a packing with area fraction  $\phi = 0.64$ . (Left) Histogram of  $|\psi_{2i}|$  for particles in the packing. (Right) Particle positions for  $\phi = 0.64$  packing, with particles with  $|\psi_{2i}| > 0.6$  highlighted in purple. Arrows indicate angle given by the complex phase of  $\psi_{2i}$ . Scale bar =  $10\mu\text{m}$ .

### 3.5 Conclusion

It appears that decreasing the area fraction of a quasi-2D packing of attractive colloidal particles below a certain threshold results in a distinct crossover into a new structural state characterized by additional low-frequency vibrational modes. These additional modes are associated with motions that are highly localized to particles with low-coordination. The change in the shape of the low-frequency tail of the vDOS of these packings due to the addition of these localized modes provides a straightforward method of distinguishing similar looking attractive packings. Once the underlying mechanisms of this crossover are better understood, this change might even be used as a method for distinguishing glass and gel states in attractive packings of intermediate density. Since previous work has correlated spatially localized modes to rearrangement-prone regions in disordered packings [12, 13, 19, 42, 101, 165], this increase of localized low-frequency modes could correlate with variation in macroscopic rheological properties of the system. Further experiments combining the vDOS analysis described above with rheological techniques could directly observe such correlations.

Additionally, though particles with low-coordination appear to be dominate these characteristic low-frequency modes, further study is required to identify the exact microstructures which permit these modes to arise. Thus far, these experiments have been performed in a specific class of quasi-2D packings with short-range attractions and fairly consistent topology (as discussed in section 3.2.2). The precise packing fraction at which these modes (and their correlated microstructures) arise, however, is sure to depend strongly on the dimensionality and morphology of the system. It should be interesting to investigate this same low-frequency behavior in various types of attractive colloidal systems, i.e., 2D and 3D particle gels formed at different rates

under different strength potentials, or under anisotropic or long-range repulsive potentials. Such studies will facilitate investigation of the generality of the gel-glass crossover we have observed.

## **Chapter 4**

# **Elasticity-Dependent Self-assembly of Micro-Templated Chromonic Liquid Crystal Films**

### **4.1 Introduction**

The engineering of novel metamaterials and biomimetic structures demands increasingly creative methods for shaping materials at the microscale. In recent years, self-assembly has been explored as a route to the creation of complex structure in various soft materials. Promising methods of self-assembly include programmed assembly of colloidal particles with designed interactions [40, 103] and controlled buckling in thin films due to competing stresses [11, 76, 172]. In the latter case, the interplay of bulk elastic properties guided by structured templates can give rise to varied and complex microstructures [11].

In a similar vein, self-assembly via templating of elastically anisotropic media has recently been demonstrated in liquid crystal films confined by micropillar arrays. Some such experiments employed microstructured templates to create arrays of defects in liquid crystal films. [15,57,58] These kinds of structures have been shown to be useful for the nucleation of novel bulk (3D) LC phases [57, 58] and for manipulation of colloidal configurations at surfaces. [15] Related work has induced bistable local director alignment in liquid crystals, yielding applications for low-energy display technologies. [77–79] However, to date such methods have only been applied to *thermotropic* nematic and smectic liquid crystals.

Lyotropic chromonic liquid crystals (LCLCs) are an important and relatively unexplored class of anisotropic fluids conducive to microscale self-assembly and compatible with aqueous media. As opposed to thermotropic liquid crystals (TLCs), which are fluids composed of a single species of anisotropic molecule, lyotropic liquid crystals form from anisotropic molecules or particles suspended in a solvent. Lyotropic *chromonic* liquid crystals are composed of plank-like aromatic molecules which, in turn, act as primary mesogens that stack into multi-molecular linear aggregates which form liquid crystal phases.

Patterned films of LCLCs have a wide variety of emerging applications distinct from other types of liquid crystals, including inexpensive polarizing films, [32,98,99] holographic displays, [102,151] organic electronics and solar cells, [115,119] biosensors, [144,168], aqueous colloidal, nanotube and bacterial assembly, [38, 113, 120, 146, 188] and precursors to structured graphene-based materials. [49,110] Besides these potential applications, LCLCs also offer useful attributes for fundamental investigation of the effects of elasticity on self-assembly behavior since their elastic properties can be tuned via control of mesogen concentration, [189] and via depletants

and ions. [121] Indeed, studies have demonstrated that LCLCs in micro-scale confinement form unique, elastic-property-dependent configurations. [64, 158]

In this chapter, we describe the patterning of LCLC films within micropost arrays. The patterns are formed via modulation of the LCLC mesophases and LCLC elastic properties by concentration changes during drying. We discover a preferred alignment in nematic films governed by elastic interactions with post-placement geometry, and we observe multiple patterned states of the columnar phase. This templating scheme has not been applied previously to lyotropic LC systems, and this contribution provides a first example of quasi-2D micropatterning of columnar LC films. We develop a numerical model to understand observed differences in patterning, and this model suggests that such effects are due to the inherent anisotropic elastic properties of films that evolve during a slow “concentrating” process. Thus, the multiple configurations that form are based on changes in bulk elastic properties, rather than changes in applied fields [77, 79] or changes in confinement geometry [78].

## **4.2 Contextual and Theoretical Background**

### **4.2.1 Lyotropic Chromonic Liquid Crystals**

Liquid crystals (LC’s) are fluid materials of anisotropic components (or *mesogens*) which lack sufficient translational order to form a true solid, but still retain some degree of orientational order. Most commonly, the mesogens are rod-like or plate-like in shape. Nematics, which are composed of mesogens oriented along the same direction but with no additional structuring, are arguably the prototypical example of a liquid crystal phase. Other common mesophases include smectic phases, wherein the orientationally aligned molecules also have translational order in a

single dimension and form layers, as well as columnar phases, wherein mesogens form “stacks” which acquire translational order in two dimensions.

Liquid crystal mesophases occur in a broad spectrum of materials. *Thermotropic* LC's are fluids composed of a single anisotropic molecular mesogen, whose phase behavior depends primarily on temperature. Liquid crystal phases can also occur in suspensions of anisotropic mesogens in a solvent. These are referred to as *lyotropic* liquid crystals. Lyotropic LC phases can be formed from suspensions of sufficiently small and anisotropic colloids or molecules, (i.e. nanotubes [63], viruses [164], and polymers [164]), but the term “lyotropic liquid crystal” is typically associated with suspensions of amphiphilic molecules. Amphiphiles have especially rich phase behavior, since they can self-assemble into structured micelles and vesicles even at low concentrations. At higher concentrations, they form nematic phases of distorted micelles, cylinders assembled in columnar phases, lamellar phases of bilayer sheets, and complicated gyroid or “plumbers nightmare” phases [14, 145].

Lyotropic chromonic liquid crystals (LCLCs), are a subset of lyotropic LC's with unique structure and phase behavior [98, 99, 150]. LCLCs are typically composed of plank-like polyaromatic compounds with ionic side-groups. When suspended in water (or in similar polar solvents), these molecules stack to form linear aggregates. Conventional knowledge indicates that in most LCLC suspensions, these molecules aggregate face-to-face, via interactions facilitated by pi-pi interactions between benzene groups and the relative hydrophilicity of ionic side groups. This broad explanation is not necessarily true for all LCLC forming molecules, and debate and research into the mechanisms and dynamics of aggregate formation, as well as their most basic structure, is still ongoing [98,99,150]. Unlike the formation of micelles in amphiphile

suspensions, the aggregation of molecules in LCLC systems is isodesmic, meaning the energy cost of adding molecules to an aggregate is constant and independent of aggregate size. Consequently, there exists no Krafft point, or point equivalent to the critical micelle concentration, in these suspensions. As a result, aggregates form even in very dilute suspensions.

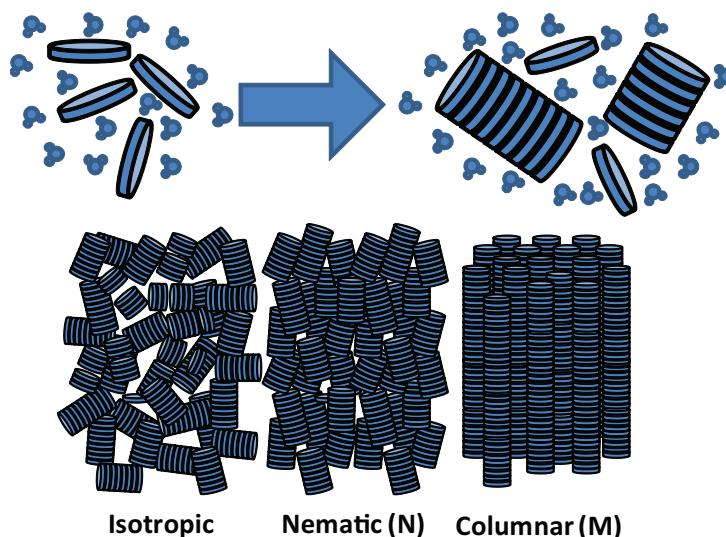


Figure 4.1: Illustration of the mesogen structure in lyotropic chromonic liquid crystals. (Top) Plank-like LCLC-forming molecules, when suspended in water, form linear aggregates, which act as mesogens for liquid crystal phases. (Bottom) The common liquid crystal phases of aggregates in chromonic liquid crystals are nematic (N) at intermediate concentrations and columnar (M) at higher concentrations.

As the suspended LCLC-forming molecules become more concentrated, the length and concentration of molecular aggregates grows to a point where the aggregates act as the mesogens of liquid crystal phases. Most LCLC's exhibit qualitatively similar phase behavior. At a high enough concentration, there is a transition to a nematic phase of aggregates (denoted as N on phase diagrams). At still higher concentrations, the aggregates will grow long enough and crowded enough to form “columns” ordered in two dimensions in a so-called columnar phase (denoted as C or M on phase diagrams). Additionally, there will typically be coexistence of

I-N and N-M phases over some concentration range. Raising the temperature of these systems will cause the average aggregate size to decrease, and it can cause the N or M phases to “melt” into the isotropic phase (at sufficiently high temperatures). Though the average aggregate size in these suspensions plays a major role in governing the liquid crystal phase behavior, the aggregate size at a given concentration and temperature is significantly polydisperse, making it difficult to form certain common liquid crystal mesophases (e.g., smectics).

#### **4.2.2 History of Chromonics**

LCLCs have been observed and studied continuously over the past century [98,99,150]. The first reported observation of a LCLC phase is given by Sandquist in 1915, when a nematic texture was observed in an aqueous suspension of phenanthrene sulfonic acid. Similar phases, with their accompanying structure of “stacked” molecular aggregates, were observed in a variety of dye-based suspensions over the next several decades. A significant leap in understanding of these materials was reached with the discovery of LCLC phases in the asthma drug disodium cromoglycate (DSCG, marketed as Cromolyn) in the early 1970's , and subsequent studies into its molecular and mesophase structure. The term “chromonic” was coined shortly thereafter by John Lydon and co-workers to describe this class of liquid crystals. This descriptor originated as a reference to the bis-chromone structure of DSCG (in a similar manner to how “cholesteric” is used to describe a broad class of chiral nematic phases first observed in cholesterol). However, this term ended up being a coincidentally appropriate term, as it also described similar phases discovered in aqueous suspensions of various dyes (*chromo-* being a common prefix referring to color) and nucleic acids (e.g., *chromosomes*).

Over the past several decades, dozens of molecules have been discovered which form chromonic

liquid crystal phases. The past decade in particular has seen a significant spike in interest in the phase behavior and structural properties of this class of materials. As can be seen from the plot in Fig. 4.2, there has been a drastic increase in the number of scientific publications referencing LCLCs since the turn of the millennium.

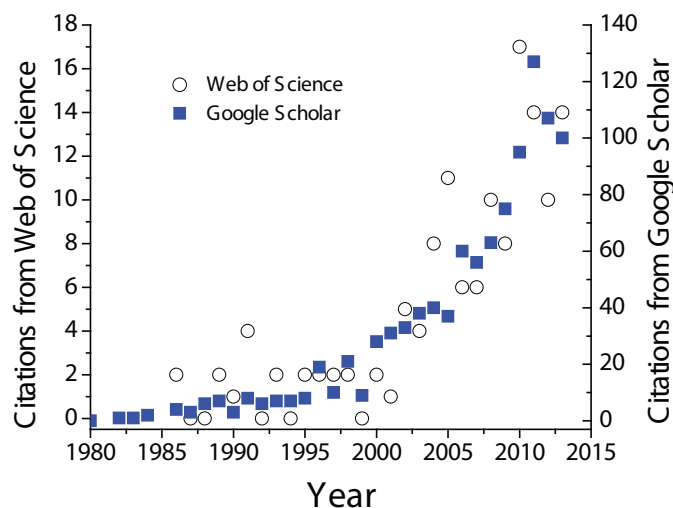


Figure 4.2: Number of academic articles containing the keyword “chromonic” from Web of Science (open circles) and Google Scholar (filled squares) per year from the past few decades.

### 4.2.3 Emerging Applications of LCLCs

The aforementioned spike in interest in LCLC’s may have to do with emerging ideas for unique applications for these materials. Since these molecules form lyotropic LC’s at relatively low weight concentrations, and since they are fairly easy to work with, many potential applications have to do with creating simple optically patterned materials. One of the oldest and most popular ideas is the fabrication of polarizing films. Since a film of a well-aligned LCLC nematic or columnar retains its birefringence when dried, researchers have proposed using it as a replacement for more costly methods for producing polarizing films, e.g. Polaroid, which involves the

inclusion of birefringent iodine crystals in an aligned polymer matrix [98, 99, 123]. This idea dates back at least to the 1940's, when John Dreyer submitted a patent for creating polarizers from dried aligned dye films [32], i.e., well before the details of LCLC phases were well understood. Additionally, studies which have created micropatterns of LCLC's have posited that such optically micropatterned materials would be useful in holographic displays [102, 151].

The multi-molecular stack structure of mesogens in LCLC's gives them unique optical, electrical and structural properties. Since the mesogens in LCLC's are stacked aggregates of plank-like molecules, the optically anisotropic molecules are aligned perpendicular to the local LC director field. This gives LCLC's negative birefringence, a property of the index of refraction of a material for light polarized along a material's extraordinary axis (in the case of liquid crystals, along the director); in this case, the index along the extraordinary direction,  $n_e$ , is lower than the index observed for light polarized along the ordinary axis (perpendicular to the director),  $n_o$ . Materials with negative birefringence are useful for making compensators for wide-angle viewing aberrations in liquid crystal displays [98]. Additionally, the pi-pi stacking of molecules within aligned molecular aggregates in LCLCs gives them some anisotropic conductivity, which has been studied for potential application in organic electronics and solar cells [115, 119]. These molecular stacks are similar enough in structure to graphitic phases of carbon that aligned LCLC films can be chemically treated so that the LCLC-forming molecules transform into vertically aligned graphene layers. These surfaces have potential applications as conductive transparent films, superhydrophilic surfaces, and high speed, high storage lithium battery electrodes [49, 110].

Though both amphiphilic and chromonic lyotropic liquid crystals can be made in aqueous

suspensions, LCLCs have been shown to have significantly lower toxicity to micro-organisms [168]. As a result, patents have been written for using LCLCs as components in devices for optical detection of biological impurities in solution [144]. Additionally, since bacteria can survive safely in these materials, LCLCs can be potentially used to manipulate and order suspensions of micro-organisms [113, 146, 188]. It has been shown that LCLCs are also effective for the alignment of other hydrophilic colloidal materials, e.g., gold nanoplates [38] and carbon nanotubes [120], which could lead to the production of unique, water-based meta-materials.

#### **4.2.4 Barriers to Practical Application of LCLCs**

In order for LCLCs to be realized in the applications described in the previous section, there are significant engineering issues that must first be overcome. Two of the most prominent obstacles are the lack of consistent alignment methods and instabilities during the drying process.

Though alignment of thermotropic LCs has been mastered for decades, the alignment of LCLCs by adjacent surfaces is significantly more difficult, in part because LCLC mesogens are large multi-molecular aggregates instead of single molecules. Creating a surface that induces strong planar alignment of TLCs is as easy as rubbing a polymer film with a fine fabric. Such a technique, however, has only been successfully deployed to induce strong planar alignment in LCLC suspensions using a certain polyimide polymer, SE-7511 (Nissan Chemical, Japan), whose manufacture has been discontinued [144]. A planar alignment method for LCLCs implemented recently covers a glass surface in nano-grooves by rubbing it with

a fine abrasive [104, 189]. However, this method has been shown to induce planar anchoring energies on the order of  $W = 3 \times 10^{-7} J/m^2$ , which are weak compared to the alignment energies necessary for practical applications (in typical applications utilizing thermotropics,  $W = 10^{-6} - 10^{-5} J/m^2$ ) [104]. Studies have shown that silanization of a glass surface using octadecyldimethyl(3-trimethoxysilylpropyl) ammonium chloride (DMOAP), a molecule which induces strong homeotropic (perpendicular) anchoring in many TLC's, can only induce transient homeotropic alignment in LCLCs at best [116]. Only very recently has it been shown that homeotropic alignment of LCLCs can be induced by noncovalent interactions with surfaces containing molecules with similar polyaromatic structure, i.e., graphene, parylene films, poly(methyl methacrylate) films, and fluoropolymer films [65], as well as polybutadiene and polydimethylsiloxane [156, 157].

In a related vein, many potential applications of LCLCs involve drying these films, which can cause the random formation of defects throughout the sample. Fig. 4.3 shows a nematic DSCG suspension placed between glass slides rubbed with an abrasive, creating an aligned film approximately  $10 \mu\text{m}$  thick. Then, as water evaporates from the open edges of the cell, the suspension becomes more concentrated and enters the columnar phase. Rather than remaining consistently aligned, the director in the columnar phase buckles throughout the sample, forming what is commonly called a “herringbone” texture when viewed under crossed polarizers. This behavior is a common phenomenon in LCLCs, as well as in other liquid crystals transitioning to the columnar phase. As solvent leaves the system and the individual aggregates grow in length in a confined geometry, a buildup of stress causes the columns to buckle. If aligned films are prepared through a “doctor blade” spreading method, where a nematic drop of LCLC is slowly

scraped along a surface with a narrow blade, this effect can be minimized, as the shear from the movement of the blade serves to align the film as it evaporates. However, even carefully prepared LCLC films stabilized by polymer additives can show some evidence of director buckling at the microscale [123].

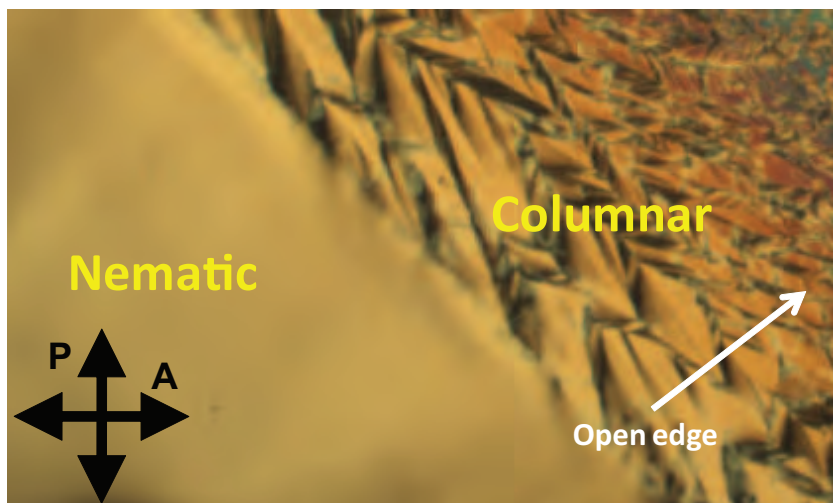


Figure 4.3: Nematic DSCG suspension placed between glass slides rubbed with an abrasive, creating an aligned film approximately  $10 \mu\text{m}$  thick, viewed under crossed-polarizers. Evaporation proceeds from an open edge beyond the upper right corner of the image, causing drying into the columnar phase. Though drying is slow, herringbone textures can be seen in the columnar phase.

The work described in this chapter is partially motivated by the desire to control the aforementioned issues in LCLCs using micro-templating. As mentioned in the introduction to this chapter, work on TLCs in square micropost arrays has induced bistable local director alignment in liquid crystals, yielding applications for low-energy display technologies [77–79]. Microposts may then be an effective method for inducing strong in-plane alignment in LCLC films. Additionally, several recent experiments at the University of Pennsylvania have employed microstructured templates to create arrays of defects in TLC films [15,57,58]. Though our scheme

may not serve as a method to completely eliminate defect formation in columnar films, we believe it may (at least) be an effective method for controlling the placement and topology of these defects, i.e., rather than allowing them to nucleate randomly throughout the sample.

#### 4.2.5 Elastic Deformations in LCLCs

The free energy cost of deformations in a nematic can be stated in a very general form as

$$F = \frac{1}{2} K_{ijkl} \nabla_i n_j \nabla_k n_l, \quad (4.1)$$

where  $n$  is a unit vector representing the local director [16]. Under several geometrical assumptions, including the mesogens being nonpolar (or,  $n \rightarrow -n$ ) and the mesogens not having chirality and thus being invariant under reflections ( $x \rightarrow -x$ ), this reduces to the well-known elastic energy of deformations in a nematic liquid crystal, the so-called Frank free energy:

$$F_{\text{Frank}} = \frac{K_1}{2} (\nabla \cdot \mathbf{n})^2 + \frac{K_2}{2} (\mathbf{n} \cdot \nabla \times \mathbf{n})^2 + \frac{K_3}{2} ((\mathbf{n} \cdot \nabla) \mathbf{n})^2. \quad (4.2)$$

This equation breaks down elastic deformations of a director field in a nematic LC into three fundamental geometrical distortions depicted qualitatively in Fig. 4.4, namely, *splay* ( $\nabla \cdot \mathbf{n}$ ), *twist* ( $\mathbf{n} \cdot \nabla \times \mathbf{n}$ ), and *bend* ( $(\mathbf{n} \cdot \nabla) \mathbf{n}$ ). The elastic constants  $K_1$ ,  $K_2$  and  $K_3$  are thus spring-constant-like parameters associated with the free energy cost of each of these deformations, respectively.

Experimental observations of thermotropic nematic liquid crystals show that many of them tend to have Frank elastic constants of the same order of magnitude. Thus, theoretical and

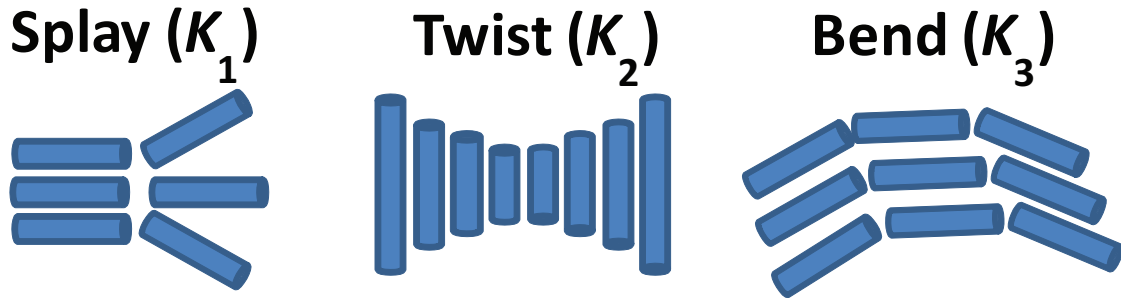


Figure 4.4: Qualitative illustration of the director deformations contributing the splay ( $K_1$ ), twist ( $K_2$ ) and bend ( $K_3$ ) deformations.

numerical models of director configurations of nematic liquid crystals often use the assumption that  $K_1 = K_2 = K_3$ , such that the Frank free energy reduces to:

$$F_{\text{Frank}} = \frac{K}{2}((\nabla \cdot \mathbf{n})^2 + (\nabla \times \mathbf{n})^2). \quad (4.3)$$

Lyotropic chromonic liquid crystals in the nematic phase, as well as polymer-based liquid crystals, are not well modeled by this assumption. Though  $K_1$  and  $K_3$  typically have similar values, they are an order of magnitude larger than  $K_2$  in these materials. A consequence of this relative ease of twist deformation is that confined droplets of LCLC's form stable director configurations which break chiral symmetry [64, 158].

The Frank elastic constants in LCLCs can be modified by formulation of the suspension. The overall and relative magnitude of these  $K$ 's varies with temperature and solute concentration [114, 189]. It has also been shown that adding a non-adsorbing polymer, (e.g., PEG) to a LCLC suspension in isotropic-nematic coexistence will locally concentrate nematic tactoids, and will induce crowding and lengthening of linear aggregate mesogens which, in turn, raises the ratio of  $K_1/K_2$  [121, 158]. Also, the addition of salt can effect the phase behavior and elastic constants of LCLCs, generally increasing  $K_1$  and decreasing  $K_3$  [121].

The effects of formulation on elastic behavior of LCLCs can be explained by the relationship between lyotropic mesogens and bulk elastic liquid crystal properties. According to [23], in a lyotropic liquid crystal,  $K_1 \propto L$ , where  $L = L_0 e^{\frac{E_a}{k_B T}}$  is the average aggregate length, and  $E_a$  is the energy needed to split an aggregate in two. As a LCLC becomes more concentrated,  $L$  will increase (as discussed in Section 4.2.1), as will  $K_1$ . Addition of salt will screen charges between individual molecules, making them more likely to aggregate (or, equivalently, increasing  $E_a$ ). This will also increase  $L$  and consequently increase  $K_1$ . LCLCs have been seen to fit well to theories for nematics of semi-flexible rods, and in this case,  $K_3 \propto P$ , where  $P$  is the persistence length of a linear aggregate. As  $P$  is independent of  $L$ , concentration does not have as drastic an effect on  $K_3$  as it does on  $K_1$ . However, additional salt serves to screen the aggregate chains from themselves, giving them additional flexibility, decreasing  $P$ , and consequently decreasing  $K_3$ .

#### 4.2.6 Defects in Columnar LCLCs

Defects in columnar liquid crystals are distinct from their counterparts in nematics due to very different costs of certain elastic deformations. Specifically, bend deformations of the director become much less energetically costly than splay or twist, since they best preserve columnar order. From another point of view, as a nematic transitions into the columnar phase, there is a necessary coupling between the density and the director [67, 69, 154] that results in a lengthscale dependence of  $K_1$ , as well as a coupling between the crystalline order and the director, resulting in a lengthscale dependence of  $K_2$  [68]. In both cases these elastic constants diverge for distortions at long wavelengths. Moreover, even in the nematic phase, fluctuations near the nematic to columnar transition strongly renormalize the elastic constants. [149] Without implementing the

full theory of the columnar phases, we can view columnar liquid crystals as a limit of nematics where  $K_1$  and  $K_2$  grow in comparison to  $K_3$ .

Qualitatively, this idea implies that splay and twist deformations in columnar LC's are extremely energetically costly compared to bend deformations. This would also be expected from the two-dimensional translational order in columnar systems; splay or twist deformations change the inter-pillar spacing in these packings, bend deformations preserve the two-dimensional lattice. As a result, the only defects observed in columnar liquid crystals are entirely bend-dominated. The defects in columnar liquid crystals consequently form *developable* domains, or rather, domains surrounded by surfaces with zero Gaussian curvature.

In quasi-two dimensional geometries, such as liquid crystal films, defect walls (DWs) separate adjacent columnar regions by a discontinuous bend in director field [82]. These defect walls can be seen in the “herringbone” textures of drying LCLC films. However, LCLCs can also exhibit high-bend, less discontinuous boundaries between aligned columnar domains (though these are not observed in the following experiments). Curvature walls (CWs), for example, exhibit a continuous, low-angle bend in the columnar director localized to a line of relatively small width. Developable domain walls (DDWs) facilitate a bend of intermediate angle through a pattern of continuously curved regions and short bend defect walls. Following [82], one can estimate the linear free energy density of these three species of domain boundaries:

$$F_{CW} = \frac{1}{12} \sqrt{K_3 B_1} \theta_0^2, \quad (4.4)$$

$$F_{DDW} = \frac{\theta_0}{2} K_3 \ln \left( \frac{R}{r} \right) + E_d \sin \left( \frac{\theta_0}{2} \right), \quad (4.5)$$

$$F_{DW} = E_d, \quad (4.6)$$

where  $\theta_0$  is the total director angle change across the domain boundary,  $B_1$  is the free energy cost of a lattice spacing deformation in the columnar liquid crystal, and  $R$  and  $r$  are the spacing and width of defect walls in DDWs, respectively. By setting these free energy densities equal at specific  $\theta_0$  values, one can estimate the domain bend angle at which the boundary transitions from a CW to a DDW( $\theta_1$ ) and a DDW to a DW ( $\theta_2$ ) as

$$\theta_1 = \sqrt{12 E_d \frac{\lambda}{K_3}}, \quad (4.7)$$

$$\theta_2 = \pi/3, \quad (4.8)$$

given several assumptions about the boundary geometries and elastic constants.

### 4.3 Experimental and Numerical Methods

In these experiments, we create microscopically thin films of chromonic liquid crystals in arrays of microscopic posts, and we model their structure using numerical free energy minimizations. We thus make unique progress by combining previous knowledge of the formulation of

chromonic liquid crystal suspensions, photolithographic synthesis of micropost arrays, polarizing microscopy of liquid crystals and numerical modeling of liquid crystals. Some of these techniques were used in previous work, though we push the limits of their applicability.

### **4.3.1 Choice of LCLC Suspensions**

We choose to utilize aqueous suspensions of two well-studied chromonic liquid crystal forming molecules in our experiments. The first, disodium cromoglycate (DSCG, also known as Cromolyn, also known as cromoglicic acid) is used as an active ingredient in various drugs that treat asthma and allergies (e.g., Intal, an inhaler-based preventative asthma treatment, and Opticrom, eye drops for alleviation of allergic conjunctivitis). The second is Sunset Yellow FCF (SSY, also known as FD & C Yellow 6, also known as Orange Yellow S), a food dye with a deep reddish-orange hue. SSY is one of the most commonly used food dyes in the United States, lending its distinctive coloring to Doritos, Cheetos, Dayquil, and many other consumables.

We use these two particular molecules, rather than any of the dozens of other known LCLC-formers, not because of their applicability in consumer goods, but rather because of the existing in-depth of understanding of their phase behavior and elastic properties. DSCG was one of the first seriously studied LCLCs, and it has been characterized extensively since the early 1970's [98, 99, 114]. The LCLC-forming properties of SSY have not been studied for quite as long as DSCG, but within the past decade liquid crystal suspensions of this dye have been well characterized and implemented in many experiments probing the phase behavior and self-assembly of LCLC's in confined geometries [64, 121–123].

Most importantly, DSCG and SSY are two of the only LCLCs whose elastic properties in the nematic phase have been quantified and characterized [114, 189]. The Frank elastic constants

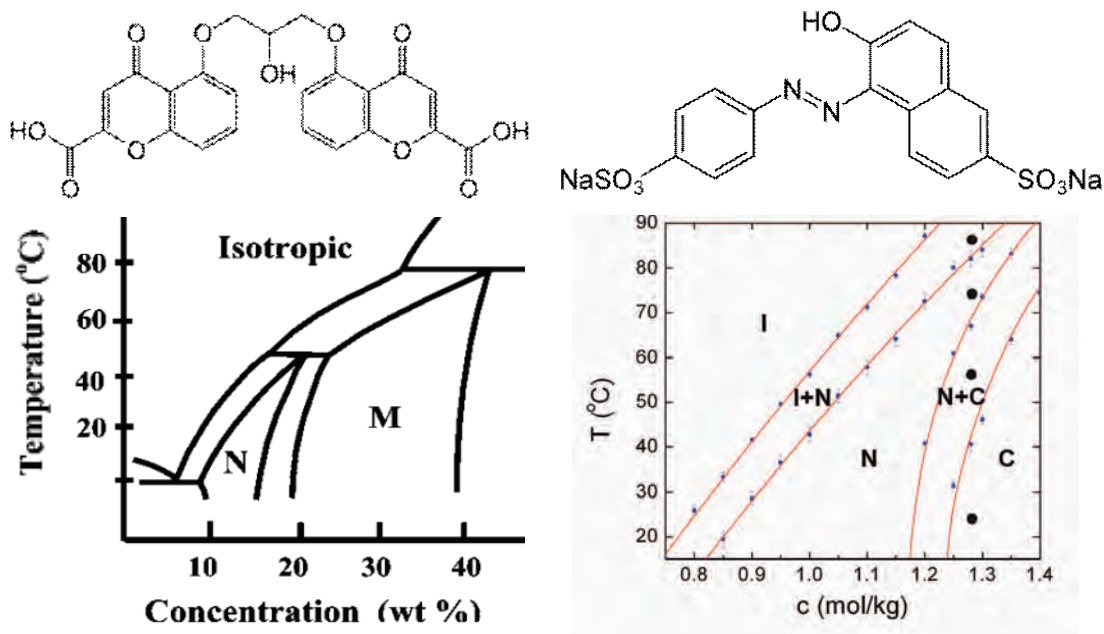


Figure 4.5: Molecular structure and aqueous suspension phase diagram of disodium cromoglycate (left) and Sunset Yellow (right). Phase diagram of DSCG from [98]; phase diagram of SSY from [122]; molecule images from Wikipedia.

have been measured at several temperatures for a single concentration of DSCG (14% by weight, or wt/wt) and for three concentrations of SSY (29.5%, 30%, and 31.5%); this previous work thus allows us to make some qualitative comparisons between films composed of these materials. The suspensions have elastic constants of a similar order and relative proportion (i.e.  $K_1, K_3 \approx 10K_2$ ), though there are some slight differences in elastic properties which, as we will see in our experiments and numerical models, play an important role in the formation of micropatterned configurations.

Although we have just pointed out that SSY and DSCG are fairly well characterized LCLC suspensions, most experiments to date investigate the behavior of either one suspension or the other; the two are never compared in the same work. This situation is mostly likely due to several key differences between these LCLC suspensions. DSCG does not absorb much light in

the optical spectrum, making it more ideal for optical imaging than SSY, which, as a dye, absorbs heavily. Also, qualitative rheological differences in the behavior of these suspensions are evident from their preparation. A nematic DSCG suspension close to the isotropic-nematic phase border (10 % wt/wt) is significantly more viscous than a more concentrated nematic SSY suspension (> 28 % wt/wt). When observed under the microscope, SSY mesogens appear to relax much faster than their DSCG counterparts. Also, while defects in the nematic director field are not often visible / easily distinguishable in DSCG suspensions, they are readily observed as optical aberrations in SSY. The nematic phases of DSCG and SSY separate when the two are mixed in solution together, implying basic chemical incompatibility. This effect is evident not just from the differences in molecular structure, but from some known differences in the assembly of multi-molecular aggregates (SSY molecules supposedly stack in a staggered pattern). Thus, though they are both LCLC suspensions with similar elastic constants, comparisons between these materials must be taken with a grain of salt.

### **4.3.2 Synthesis and Loading of Micropost Arrays**

We create chromonic liquid crystal films in photolithographically printed arrays of cylindrical microposts (Fig. 4.6). Photolithographic techniques are used to make cylindrical microposts of negative tone epoxy-based photoresist, SU-8 2000 series (Microchem Inc.) on a glass substrate. We employ cylindrical posts in order to separate the effects of micropost placement from micropost shape, since previous studies show that anisotropic or sharp-featured post shapes can dominate alignment and organization of liquid crystals. [77,155] Micropost cylinders with height  $h = 5 \mu\text{m}$ , and diameter  $d = 7 \mu\text{m}$ , are arranged in a square lattice with center-to-center pitch of  $a = 14 \mu\text{m}$ .

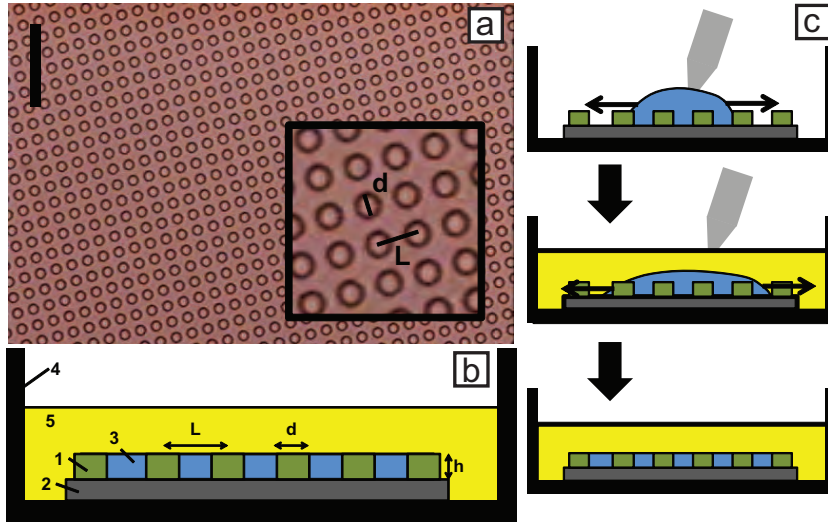


Figure 4.6: Configuration of micropost arrays loaded with liquid crystals. a) Bright-field microscopy image of an empty SU-8 micropillar array with post center spacing  $L = 14\mu\text{m}$ , diameter  $d = L/2 = 7\mu\text{m}$ , and height  $h = 5\mu\text{m}$ . Scalebar =  $50\mu\text{m}$ . Inset: close-up of microposts, indicating  $d$  and  $L$ . b) Schematic of micropost array configuration after loading with LCLC film. SU-8 microposts (1) sit atop a glass wafer (2). After being loaded with a LCLC (3), the wafer is placed in a glass petri dish (4) and immersed in hexadecane(5). c) Schematic of LCLC film loading procedure. A droplet of heated LCLC suspension is placed in a droplet onto a cleaned and heated micropost array where it begins to spread due to capillary forces (top); immediately afterward, hexadecane is placed to completely cover the sample, and LCLC droplet continues to spread (middle); after several minutes, the LCLC film has spread to cover the entire micropost array, leaving a level film at the post height (bottom).

After the micropost arrays are thoroughly rinsed and plasma-cleaned, they are filled with one of the two LCLC-forming molecules mentioned in the previous section (DSCG and SSY) suspended in Millipore filtered water at various concentrations. DSCG is sufficiently pure to be used as-is; SSY, by contrast, is purified by re-suspension in water, precipitation through the addition of ethanol, and centrifugation several times in order to reach a purity of  $> 99\%$ .

The procedure for filling the micropost array with LCLC is illustrated in Fig. 4.6. Micropost-covered glass slides are placed in a petri dish and heated to  $60\text{ }^{\circ}\text{C}$ . At the same time, the LCLC suspension (which is in the isotropic phase at this temperature) is also heated to  $60\text{ }^{\circ}\text{C}$ . A droplet of  $2\text{-}3\text{ }\mu\text{L}$  of LCLC solution is placed on the substrate and then spreads rapidly due to capillary interactions with the microposts. Several mL of hexadecane are then immediately placed over the LCLC and substrate in order to prevent rapid evaporation of the aqueous suspension. The entire system is left at  $60\text{ }^{\circ}\text{C}$  for several minutes, until the LCLC droplet has ceased spreading. The petri dish is then placed on a microscope stage at  $25\text{ }^{\circ}\text{C}$  and allowed to cool to ambient temperature, at which time the LCLC film re-enters the nematic mesophase. The LCLC-hexadecane surface tension is large enough to insure that the aqueous film spreads evenly through the micropost array, eventually resting at the high-edge of the micropillars with an undeformed, flat interface. Under these conditions, all surfaces in contact with the aqueous phase (glass substrate, pillar sides, and hexadecane interface) induce degenerate planar anchoring of the LCLC mesogens.

### **4.3.3 Polarizing Imaging and Director Field Analysis**

One significant technical innovation of this thesis concerns a means to carry out high-fidelity liquid crystal director analysis using polarization video microscopy. Birefringent lyotropic chromonic

liquid crystal (LCLC) films in micropost arrays are placed on a rotating stage of a Leica DM IRB microscope under a 63x air objective between crossed polarizers. Once the stage is centered to ensure that the center of rotation lies in the microscope field of view, the stage is rotated by hand a total of  $360^\circ$  while video is acquired at 10 frames per second on an UNIQ UP 680-CL digital camera. The resulting images have a resolution of 312 nm/pixel. The polarizer and analyzer direction in the resulting video are fixed on the image's vertical and horizontal axes.

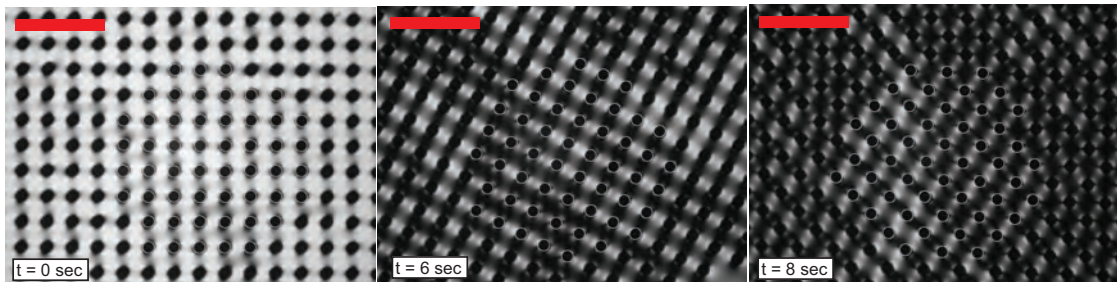


Figure 4.7: Crossed-polarizer images from a movie of a rotating 30% wt/wt Sunset Yellow aqueous nematic film in an array of cylindrical microposts of diameter  $7 \mu\text{m}$  and height  $5 \mu\text{m}$ , overlaid with bright circles centered at tracked post centers. Polarizer and analyzer oriented along the vertical and horizontal of images. Scale bars =  $50 \mu\text{m}$ .

To obtain the translation and rotation of the sample, we process the images, and in this process, render the post locations trackable via well-used particle tracking algorithms. Specifically, we invert the image (by subtracting the current pixel values from the maximum value), increase the image contrast by raising the pixel intensity to the eighth power, and then convolute the resulting image with the image of a bright disk whose radius equals the observed post radius in the images (Fig. 4.8). After setting all pixels below an arbitrary threshold to zero, the resulting “processed” image gives us a set of bright intensity peaks located at the centers of each post. We then track these bright intensity peaks using a commonly used sub-pixel tracking algorithm [26]. The tracked post locations compare well with the original unprocessed image (Fig. 4.7).

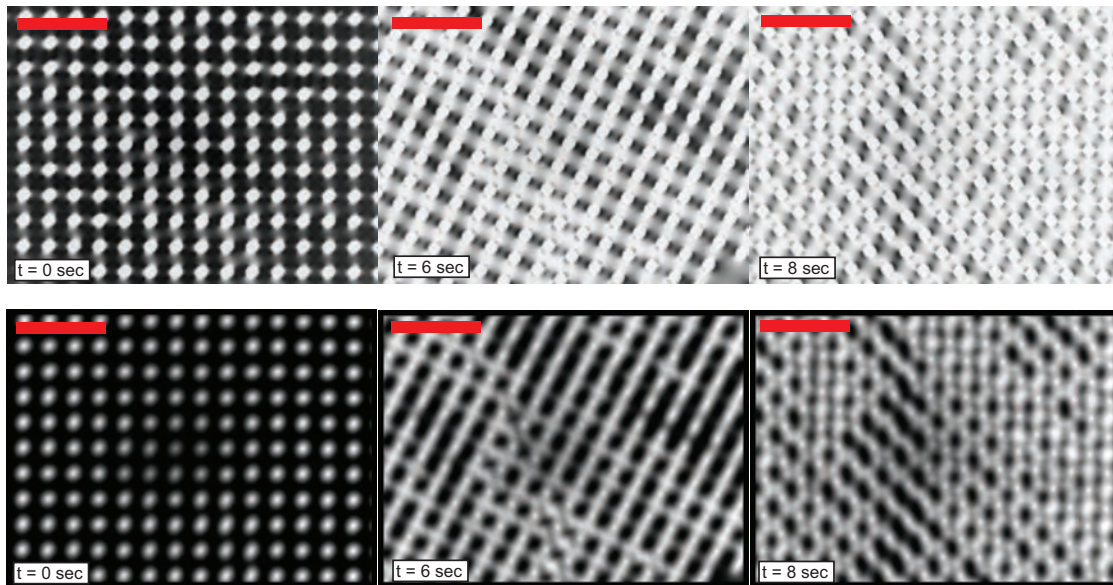


Figure 4.8: Intermediate post-processing steps for post tracking a rotating 30 percent Sunset Yellow aqueous nematic film in an array of cylindrical microposts of diameter  $7 \mu\text{m}$  and height  $5 \mu\text{m}$ . (Top) Inverted cross-polarizer images, calculated from subtracting original image pixel values from the maximum pixel brightness. (Bottom) Inverted images convoluted with a uniformly bright disk of diameter equal to the post diameter, yielding near-gaussian peaks centered at the post centroids. Scale bar =  $50 \mu\text{m}$ .

Importantly, the resulting tracks of the post centers yield useful information about the motion of the sample during its rotation between the crossed-polarizers. We first calculate the average motion of all tracked posts from frame-to-frame; this yields the translational motion of the sample, e.g., due to slight shifts of the stage during manual rotation. We then remove this frame-to-frame translational motion from the video using a cubic convolution interpolation method. This procedure yields a video with pure rotational motion (Fig. 4.9).

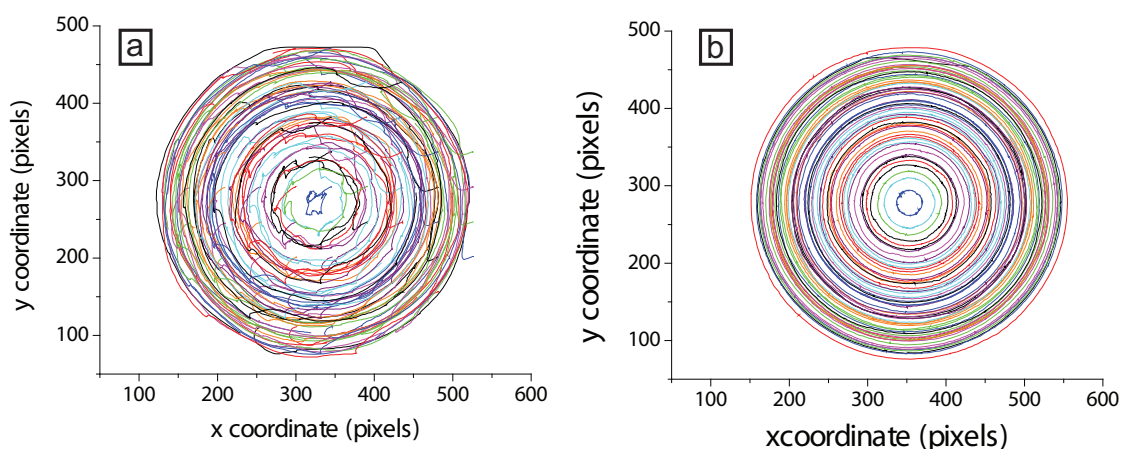


Figure 4.9: (a) Trajectories of 59 posts tracked through a  $360^\circ$  sample rotation. (b) Trajectories with average translational motion per frame removed.

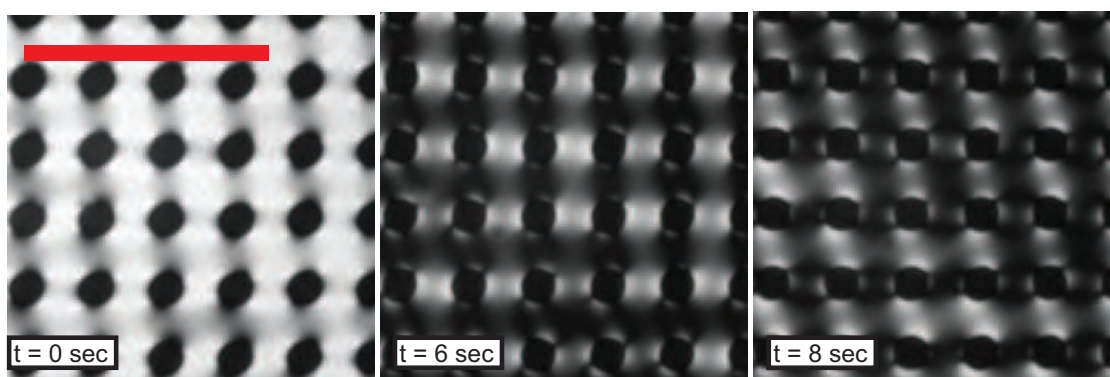


Figure 4.10: Selections of images of the SSY film from Figure 1, with net sample rotation and translation removed. Polarizer/analyzer are oriented at angles of  $0^\circ$  ( $t = 0$  sec),  $37^\circ$  ( $t = 6$  sec), and  $55^\circ$  ( $t = 8$  sec) with respect to the vertical/horizontal of images.

The rotation of the system from frame  $t$  to  $t + 1$  is calculated as the average rotation angle  $\theta_i(t)$  of each post position  $(x_i, y_i)$  around the mean post position  $(x_0, y_0)$ . This is calculated using the approximation  $\theta_i = dr_{perp}/r$ , where  $\mathbf{dr}_i(\mathbf{t}) = [\mathbf{x}_i(\mathbf{t} + \mathbf{1}) - \mathbf{x}_i(\mathbf{t}), \mathbf{y}_i(\mathbf{t} + \mathbf{1}) - \mathbf{y}_i(\mathbf{t})]$  is the motion of a post,  $r_i(t) = [x_i(t) - x_0, y_i(t) - y_0]$  is the distance between the post and the center of rotation, and  $dr_{perp}$  is the component of  $dr$  perpendicular to  $r$ . We expect this approximation to be valid, since the rotation of the system over a single time frame is no greater than  $3^\circ$ . The rotation  $\theta(t)$  is then removed from the original, unprocessed images using a cubic convolution interpolation. The resulting video shows stationary posts as the polarizer and analyzer are rotated at an angle  $\theta_{pol} = -\theta_{sample}$  to the vertical/horizontal directions in the images (Fig. 4.10).

The equation for transmitted light intensity through a birefringent liquid crystal sample between crossed-polarizers is given by

$$I_t = I_i \sin^2(\phi/2) \sin^2(2\theta), \quad (4.9)$$

where  $\theta$  is the angle between the optical axis of the liquid crystal (director) and the polarizer/analyzer. The retardation  $\phi$  depends on the sample thickness, birefringence, and out-of-plane tilt angle. Assuming the director is purely in-plane, then the term containing  $\phi$  will not vary spatially, and the relative intensity should depend only on the term containing  $\theta$ . Thus, we consider the intensity variations per pixel as the polarizer and analyzer are rotated with respect to the LCLC film:

$$I_t = I_0 \sin^2(2(\theta_{dir} - \theta_{pol})), \quad (4.10)$$

where  $I_0$  is a qualitative measure of the in-plane director order (note, a small value indicates local

disorder due to a defect or a director oriented slightly out-of-plane. Large out-of-plane directors will cause changes in  $\phi$  which can decrease *or* increase  $I_0$ ). Indeed, by looking at representative pixels intensities in a motion-removed image, we see this functional form fits quite well (Fig. 4.11). By fitting curves to Equation 4.10, with  $I_0$  set as the amplitude of intensity fluctuations, we find the average in-plane director angle  $\theta_{dir}$  at each pixel in the image.

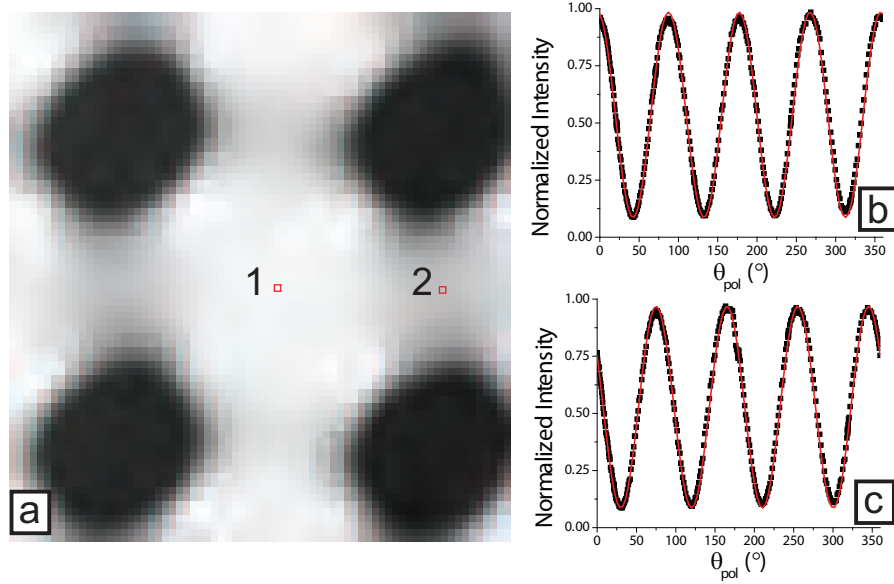


Figure 4.11: (a) Selection of unprocessed video of SSY film under crossed-polarizers, when the polarizer/analyzer is oriented at an angle of  $0^\circ$  ( $t = 0$  sec) with respect to the vertical/horizontal of the image. (b-c) Image brightness / transmitted light intensity at pixels 1 and 2, respectively, as a function of the angle of polarizer/analyzer to image horizontal/vertical,  $\theta_{dir}$ . Red lines indicate fits to the function  $I = I_0 \sin^2(2(\theta_{dir} - \theta_{pol})) + B$ , where  $I_0$  is the difference in maximum and minimum intensity, and  $B$  is the minimum intensity value. For (a),  $\theta_{dir} = 42.3^\circ$ , and (b),  $\theta_{dir} = 30.15^\circ$ .

We note that there exists a degeneracy in this fitting method for finding  $\theta_{dir}$ , since  $I_0 \sin^2(2(\theta_{dir} - \theta_{pol})) = I_0 \sin^2(2((\theta_{dir} + \pi/2) - \theta_{pol}))$ . However, we can determine whether local director orientation follows  $\theta_{dir}$  or  $\theta_{dir} \pm \pi/2$  by comparing images with full-waveplate retardation crossed-polarizer images (which distinguishes local directors under  $\pi/2$  rotations), by observing local post boundary conditions (directors should lie parallel to post surfaces in minimum-energy

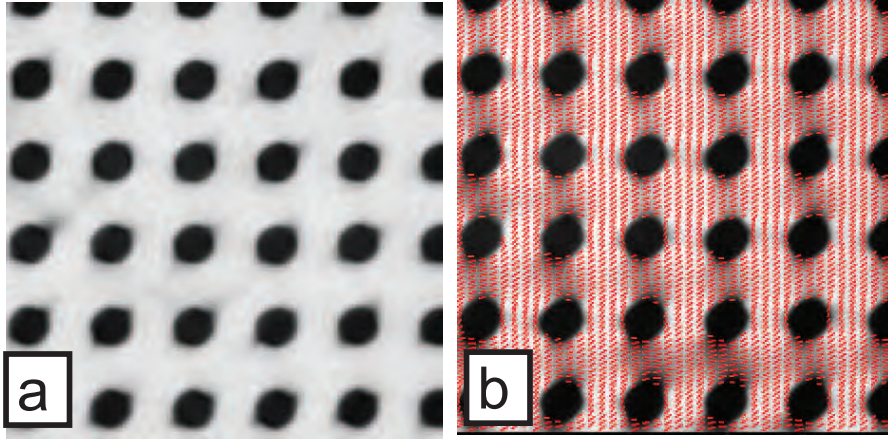


Figure 4.12: (a) Relative in-plane director magnitude,  $I_0$ . Indications of defects at the edges of posts are shown as small dark spots. (b) In-plane director orientation (red lines) plotted over grayscale image of in-plane director magnitude  $I_0$ . For the sake of clarity, only every 10th pixel is represented in this image.

configurations), and by minimizing obvious director discontinuities.

#### 4.3.4 Numerical Modeling of Liquid Crystals in Micropost Arrays

To supplement and verify our experimental observations of liquid crystal configurations in micropost arrays, we perform numerical minimizations of a phenomenological Landau de-Gennes (LdG) free energy for a nematic director field under similar confinement conditions [15, 138]. The free energy is minimized in a finite difference scheme on a regular cubic mesh, using a conjugate gradient minimization routine from the ALGLIB package. Specifically, we simulate a box of  $50 \times 50 \times 15$  points, with a 24-point diameter cylindrical pillar in the center, tangential boundary conditions at the top, bottom and post surface, and periodic boundary conditions at the edges. In the uniaxial limit, the LdG free energy is written in terms of the tensor  $Q_{ij} = \frac{3}{2}S(n_i n_j - \frac{1}{3}\delta_{ij})$ , where  $n_i$  is the  $i$ th component of the nematic director,  $\delta_{ij}$  is the Kronecker delta, and  $S$  is the nematic degree of order. The free energy density (per unit area) is a

sum of two components: a phase free energy density

$$f_{\text{phase}} = \int dV \left( \frac{1}{2} A \text{Tr}(\mathbf{Q}^2) + \frac{1}{3} B \text{Tr}(\mathbf{Q}^3) + \frac{1}{4} C (\text{Tr}(\mathbf{Q}^2))^2 \right) \quad (4.11)$$

and a gradient free energy density, which, for a generic nematic LC with equal elastic constants reads

$$f_d = \frac{1}{2} L \int dV (\nabla \mathbf{Q})^2. \quad (4.12)$$

For lack of better information about elastic properties of LCLCs, we used values for A, B and C consistent with a commonly studied thermotropic nematic liquid crystal, 4-cyano-4'-pentylbiphenyl (5CB).

Though the above free energy suffices for qualitative modeling of generic nematic liquid crystals, applying these same numerical methods for understanding columnar configurations requires care. The distortion free energy,  $f_d$ , shown in Equation 2 is a valid approximation for modeling a generic thermotropic nematic like 5CB. This can be re-stated as a Frank free energy,

$$f_{\text{Frank}} = \frac{K_1}{2} (\nabla \cdot \mathbf{n})^2 + \frac{K_2}{2} (\mathbf{n} \cdot \nabla \times \mathbf{n})^2 + \frac{K_3}{2} ((\mathbf{n} \cdot \nabla) \mathbf{n})^2, \quad (4.13)$$

where  $K_1$ ,  $K_2$ , and  $K_3$ , the splay, twist, and bend elastic constants, respectively, are similar in magnitude. However, as a nematic transitions into the columnar phase, there is a necessary coupling between the density and the director [67,69,154] that produces a lengthscale dependence of  $K_1$ , as well as a coupling between the crystalline order and the director, resulting in a lengthscale

dependence of  $K_2$ . [68] In both cases these elastic constants diverge at long wavelengths. Moreover, even in the nematic phase, fluctuations near the nematic to columnar transition strongly renormalize the elastic constants. [149] In this thesis, we do not implement the full theory of columnar phases; rather, we consider the nematic theory with differing elastic constants, and we consider the limits wherein  $K_1$  and  $K_2$  grow in comparison to  $K_3$ . The above form of the LdG free energy cannot model this system, as it assumes equal  $K$ 's. However, if we use an expanded form of the LdG free energy [138],

$$f_d = \frac{1}{2} \left( L_1 \frac{\partial Q_{ij}}{\partial x_k} \frac{\partial Q_{ij}}{\partial x_k} + L_2 \frac{\partial Q_{ij}}{\partial x_j} \frac{\partial Q_{ik}}{\partial x_k} + L_3 Q_{ij} \frac{\partial Q_{kl}}{\partial x_i} \frac{\partial Q_{kl}}{\partial x_j} \right), \quad (4.14)$$

then, following previous numerical work [138], we find the following relationships between  $L$  and  $K$  terms:

$$K_1 = \frac{9}{4} S^2 (2L_1 + L_2 - SL_3) \quad (4.15)$$

$$K_2 = \frac{9}{4} S^2 (2L_1 - SL_3) \quad (4.16)$$

$$K_3 = \frac{9}{4} S^2 (2L_1 + L_2 + SL_3). \quad (4.17)$$

Therefore, to model columnar configurations, we run the LdG free energy minimizations under the same conditions as for the nematic case, except we employ the expanded form of the LdG free energy of Equation 4.14, along with values of  $L_i$  such that  $K_3$  is decreased by at least an order of magnitude compared to  $K_1$  and  $K_2$ . Thus, even though the LdG free energy models a nematic LC, by using the aforementioned limit of elastic constants, we can approximate an expected director field as a nematic approaches the columnar phase. As discussed in section 4.2.6,

this is reasonable because splay and twist deformations become far more energetically costly compared to bend deformations in columnar phases, as only bend deformations preserve columnar spacing. Further, instead of initializing the director configuration randomly (which leads to random defect nucleation and frustrated high energy states), we start with a bulk director field uniformly oriented in the plane of the post array. As major out-of-plane director deformations would include large splay and twist components, which are difficult in columnar LCs, and since the in-plane director component measured in experiments is constant (away from defect walls), assuming in-plane director orientation is a reasonable assumption to make.

## **4.4 Results and Discussion**

### **4.4.1 Nematic Configurations**

Observations and simulations of nematic LCLC films in micropost arrays demonstrate that such films have a tendency to align along either diagonal of the square lattice of cylindrical posts. To create larger, well-ordered films, weak alignment along one direction is necessary to break the degeneracy along the two diagonals. Competition between this preferred alignment and surface rubbing demonstrate that the alignment effects of post geometry are comparable to the most effective surface anchoring methods available at present.

Initial observations of the nematic LCLC films under crossed-polarizers do not indicate any obvious consistent director patterning on a scale larger than a single pillar spacing (though the director orientation appears to lie predominantly in-plane). Considering that there may exist multiple metastable local director configurations for a nematic under such confinement, we sought to create a more consistently ordered film by introducing a weak directional bias into the film.

To achieve this goal, we form the micropillar arrays on glass surfaces that are first rubbed with a fine abrasive pad (3M Trizact Foam Disc P3000). This rubbing creates nano-sized grooves in the bottom glass surface which, in turn, induce a weak, oriented planar alignment on the overlying chromonic liquid crystal [104, 189].

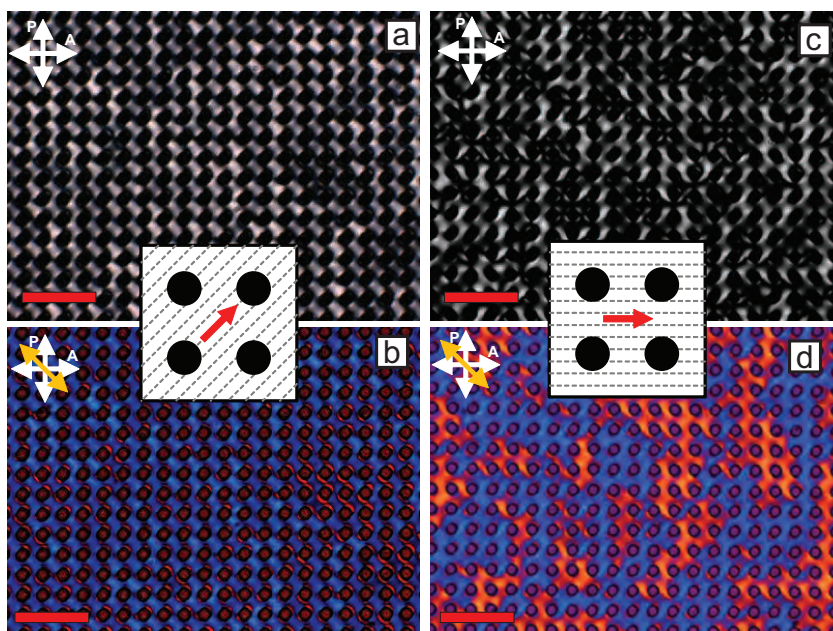


Figure 4.13: Micropost arrays filled with nematic DSCG (14% wt/wt) at room temperature. Crossed-polarizer (a & c) and crossed-polarizer with full wave retardation plate (b & d) images shown with bottom surfaces rubbed along a lattice diagonal (a & b) or a post lattice direction (c & d), as illustrated in the insets. Scale bar = 50  $\mu\text{m}$ . The slow axis of the retardation plate is given by the orange arrow in (b & d).

As can be seen in Fig. 4.13, the consistency of director patterning in the final film is dependent on the rubbing direction on the bottom surface. For example, a surface rubbing along a diagonal of the post lattice produces a consistent nematic texture under crossed-polarizers. The same degree of rubbing along a post lattice direction, however, did not produce coherent patterning over multiple post spacings. This observation implies a preferred director orientation along a diagonal of the post lattice, with the symmetry of the bistability broken by the weak oriented

anchoring potential provided by the rubbing.

We model a generic nematic film in such a post array using numerical LdG free energy minimization, and we find that the minimum energy configuration does indeed demonstrate average alignment along a diagonal of the micropost lattice, skewing slightly off-diagonal between adjacent posts (Figure LC13). Two vertically aligned  $-1/2$  topological disclinations per post are also observed, separated from the micropost centers along a diagonal of the square lattice, which is parallel to the average director alignment. This alignment configuration implies a bistable preferred director orientation along either diagonal of the micropost lattice. We did not observe this configuration in our initial experiments, because of the random nucleation of diagonally aligned domains that arises during the isotropic-nematic cooling of the film, thereby creating an “overall disordered” director pattern. The anchoring strength of this rubbing technique, though not strong enough to induce an arbitrary overall alignment, for example, along a lattice direction, is sufficient to break the two-diagonal degeneracy of the system.

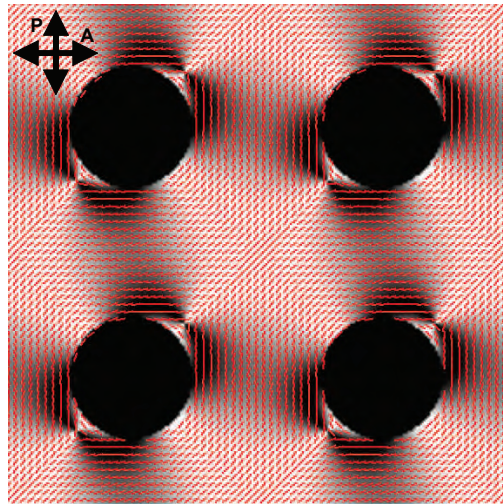


Figure 4.14: Average in-plane director orientation (red lines) from a minimization of the LdG free energy for a generic nematic in cylindrical micropost confinement, overlaid by the schlieren texture expected when viewed between crossed-polarizers.

Quantification of the LC director orientations in the aligned nematic films demonstrates that both DSCG and SSY nematic films have director configurations consistent with our expectations based on the LdG free energy minimizations for a generic nematic LC (Fig. 4.15). Additionally, the degree of in-plane director order is observed to decrease close to the microposts, suggesting the presence of defects or a slight out-of-plane director at locations wherein one would expect  $-1/2$  disclinations in the LdG free energy minimizations.

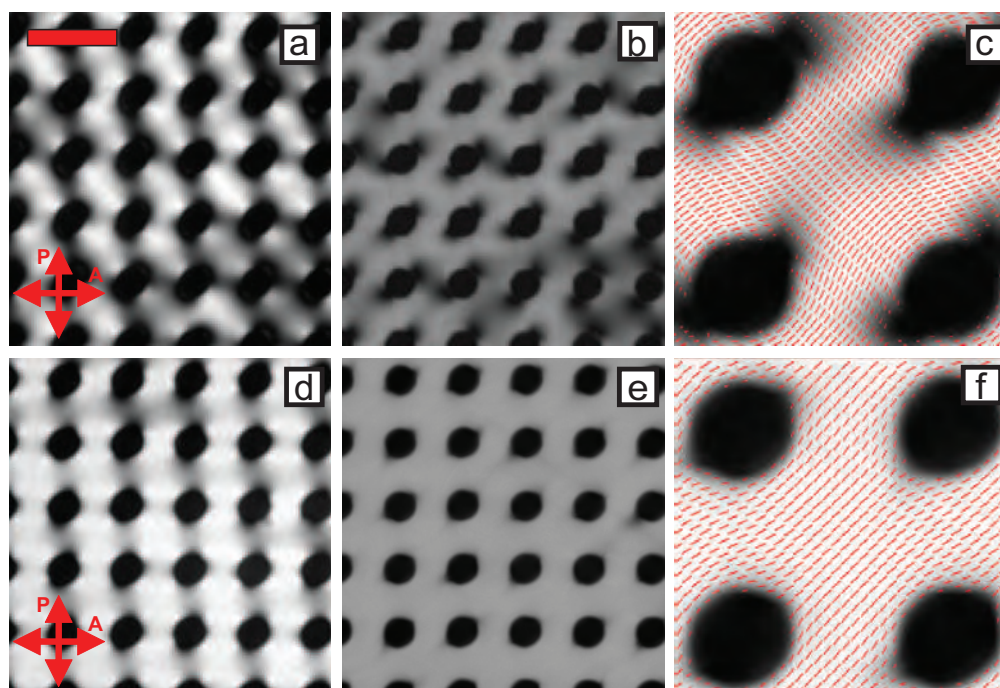


Figure 4.15: Nematic films of 14% wt/wt DSCG (a-c) and 30% wt/wt SSY (d-f) in micropost arrays. Images show schlieren textures under crossed-polarizers (a & d), average in-plane director magnitude (b & e), and average in-plane director orientation for a selected region of 4 posts (c & f). Scale bar =  $20 \mu\text{m}$ .

#### 4.4.1.1 Estimation of Anchoring Strength of Rubbing Alignment

Based on the fact that rubbing the bottom surface parallel to the lattice direction does not produce a single aligned domain, the anchoring from the rubbed surface is not strong enough to

overwhelm the alignment preferred by the micropost geometry. Combined with the LdG numerical modeling of the director field outlined in section 4.3.4, we use this experimental result to estimate an upper bound  $W_{max}$  on the anchoring strength of the abrasively rubbed surface  $W$ . In the Rapini-Papoular approximation [137] for uniform planar anchoring at an angle  $\theta_0 = 0^\circ$  from the  $x$ -axis of the post lattice, a director field  $\mathbf{n} = (\cos \theta(x, y), \sin \theta(x, y))$  at an aligned surface incurs a free energy penalty per unit area of

$$f_{\text{anchor}} = \frac{1}{2}W \sin^2(\theta(x, y)). \quad (4.18)$$

We can make an estimate of  $W_{max}$  by including the above free energy penalty in the LdG free energy minimizations described in Section 4.3.4, varying  $W$ , and observing the change in stable director configurations. In terms of  $Q_{ij}$ , Equation 4.18 is

$$f_{\text{anchor}} = W/(16S_0^2)(\mathbf{Q} - \mathbf{Q}_0)^2, \quad (4.19)$$

where  $(Q_0)_{ij} \equiv 2S(\nu_i\nu_j - \frac{1}{2}\delta_{ij})$ ,  $\vec{\nu} = (1, 0)$ . Equation 4.19 is added to the Landau-de Gennes free energy densities. As in Section 4.3.4, we minimize the LdG free energy from random initial conditions, and we observe a pair of  $-1/2$ -index disclinations positioned along a line making an angle  $-45^\circ < \phi_d < 45^\circ$  to the rubbing direction (i.e., the  $x$  axis of the micropost lattice). Since  $0^\circ < \phi_d < 45^\circ$  and  $-45^\circ < \phi_d < 0^\circ$  are geometrically equivalent, we consider  $|\phi_d|$  as a function of  $W$  in Fig. 4.16. In this plot,  $|\phi_d|$  decreases monotonically from  $|\phi_d| = 45^\circ$ , the defect configuration preferred by the lattice geometry, to  $|\phi_d| = 0^\circ$ , the defect configuration preferred by the bottom surface anchoring condition, with increasing  $W$ .

The fact that our abrasive rubbing procedure does not obviously bias the orientations of defect pairs away from  $|\phi_d| \approx 45^\circ$  in experiment suggests that  $|\phi_d| \geq \phi_{\min} = 0.9 \times 45^\circ = 40.5^\circ$  (assuming difficulty in distinguishing between  $\phi_{\max} = 45^\circ$  and  $\phi_{\min} = 0.9 \times \phi_{\max}$  by the naked eye). This provides an upper bound on the rubbing anchoring strength  $W_{\max} = W(\phi_{\min})$ . From Fig. 4.16,  $W_{\max} \approx 1 \times 10^{-7} \text{ J/m}^2$ . This value is similar to the anchoring strength of this technique experimentally measured in a separate study,  $W = 3 \times 10^{-7} \text{ J/m}^2$ , which is still an order of magnitude lower than the anchoring strengths of conventional alignment techniques for thermotropic liquid crystals ( $W = 10^{-6} - 10^{-5} \text{ J/m}^2$ ) [104].

## 4.4.2 Columnar Configurations

Observations of columnar films in LCLC experiments and numerical models of columnar LCs demonstrate two possible alignment and defect wall configurations of columnar films in the observed micropost arrays. The stability of these configurations appears to be related to the elastic properties of the film during the columnar structure formation. Specifically, films with a higher ratio of splay to bend free energy cost ( $K_1/K_3$ ) will form an array of defect wall “squares,” while films with a lower  $K_1/K_3$  ratio form an array of zig-zagging defect walls. In experiment, these elastic properties can be controlled by the type and initial concentration of LCLC forming material in the film.

### 4.4.2.1 Experimentally Observed Columnar Patterns

During the slow drying of these films from the nematic state, water is lost to the overlying hexadecane, and the LCLC nematic film transforms into a high-concentration columnar mesophase. Interestingly, this phase transition is accompanied not only by significant changes in the local

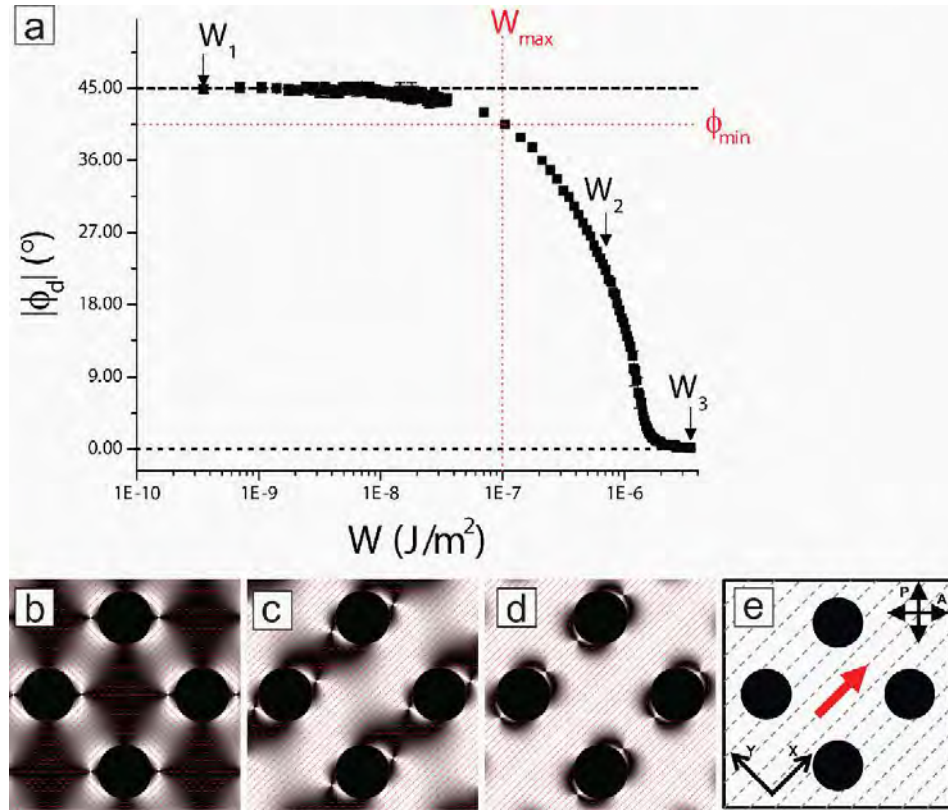


Figure 4.16: Results of LdG numerical modeling with varying planar oriented anchoring strength along the bottom of the cell. The planar anchoring is parallel to one of the lattice axes (in this case along the  $x$  direction) and has a strength  $W$ . a) Absolute value of the angle of the stable defect orientation with respect to the bottom surface anchoring direction  $|\phi_d|$ , as a function of anchoring strength  $W$ . Each point is averaged over 10 random initial configurations.  $W_{max} = 1.0 \times 10^{-7} \text{ J/m}^2$  is set at the value of  $W$  resulting in  $|\phi_d| = \phi_{min} = 40.5^\circ$ . Bottom: simulation results for local director orientation (red lines) and corresponding schlieren textures given polarizer, analyzer, lattice axes and rubbing direction (dashed lines / red arrow) given in schematic (e) for (b)  $W_1 = 3.52 \times 10^{-10} \text{ J/m}^2$ , (c)  $W_2 = 7.04 \times 10^{-7} \text{ J/m}^2$  and (d)  $W_3 = 3.48 \times 10^{-6} \text{ J/m}^2$ .

director configuration, but also by the appearance of dark lines in bright-field microscope images (Fig. 4.17 and Fig. 4.18). The resulting columnar liquid crystal film thus forms two very different director configurations dependent on type (i.e., DSCG or SSY) and on the concentration of the chromonic liquid crystal used to make the initial nematic film.

For columnar DSCG films, which cross over from an initial nematic phase with concentration  $< 17.5\%$  wt/wt, we observe configurations containing pairs of defect lines running between adjacent posts, and forming local squares or rhombuses with posts at the vertices (Fig. 4.17). By quantifying the director orientation and magnitude, we see that the defect lines in the bright field images correspond to areas with low in-plane director magnitude,  $I_0$ . Additionally, these lines appear to divide the space into regions with distinct (i.e., locally uniform) director orientations. This observation suggests that the lines are defect walls, i.e., plane-like defects in columnar liquid crystals that occur in regions across which there exists a discontinuous bend in director orientation. [83] In these samples, the area between four posts is populated by a director oriented close to a diagonal of a lattice, and the regions between adjacent posts contain directors oriented close to a lattice direction. Notice that these patterns of alignment are similar to the director configuration found in the nematic films, albeit with a much sharper off-diagonal director bend between adjacent posts.

A different defect placement and local director distribution arises in columnar DSCG films with an initial pre-drying concentration  $> 18\%$  wt/wt and in all columnar SSY films (Fig. 4.18). The defect walls, indicated by dark lines in bright-field and low in-plane director magnitude, run between adjacent posts in a single lattice direction, as well as between posts on a lattice diagonal perpendicular to the initial nematic director alignment, forming zig-zags of defect walls. These

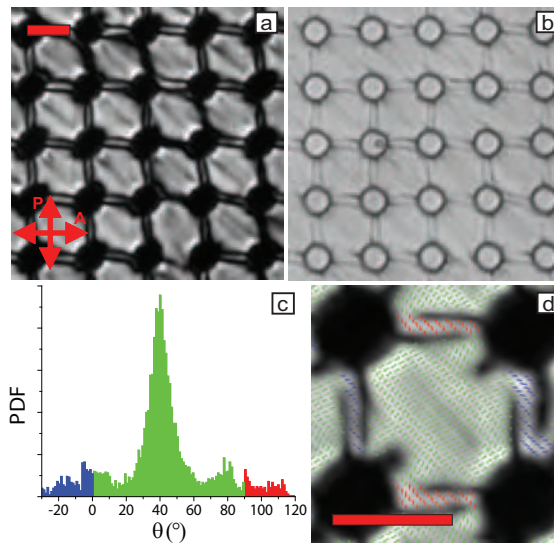


Figure 4.17: Columnar film of DSCG dried from a nematic DSCG film of initial concentration 17% wt/wt. Images show (a) crossed-polarizer image of the film; (b) bright field image of the film (where defects are visible as dark lines); (c) probability distribution of in-plane director orientations with respect to the horizontal post lattice spacing direction; (d) average in-plane director orientation for four posts, colored by angle using the same scheme as (c) and plotted over the average in-plane director magnitude (bright=in-plane, dark=out-of-plane/disordered). Scale bar = 10  $\mu\text{m}$ .

defect walls divide the director configurations into three distinct regions. Between diagonal posts, the director is aligned within  $5^\circ$  of a lattice diagonal; between adjacent posts, the director lies on (or slightly tilted past) a lattice direction; and the remaining rhombus-like region contains a director oriented between these directions, typically  $20\text{-}30^\circ$  off the lattice direction. Unlike the “square” configuration, the average director field in this case appears to lie significantly off the diagonal of the micropost lattice.

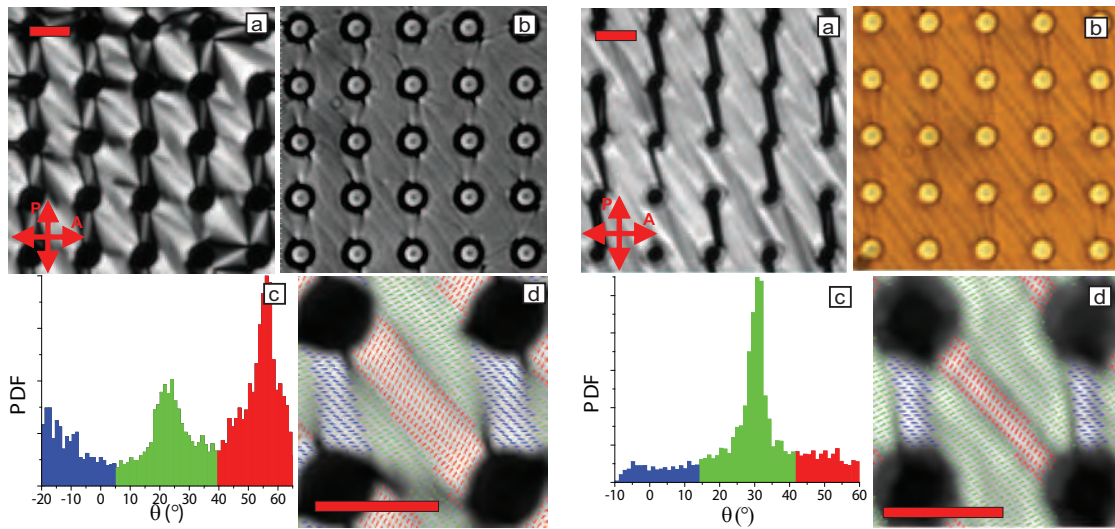


Figure 4.18: Columnar films dried from (left) nematic DSCG film of initial concentration 18% wt/wt and (right) SSY. Images show (a) crossed-polarizer image of the film; (b) bright field image of the film (where defects are visible as dark lines); (c) probability distribution of in-plane director orientations with respect to the horizontal post lattice spacing direction; (d) average in-plane director orientation for four posts, colored by angle using the same scheme as (c) and plotted over the average in-plane director magnitude (bright=in-plane, dark=out-of-plane/disordered). Scale bar =  $10\ \mu\text{m}$ .

#### 4.4.2.2 Numerical Reproduction of Columnar Patterns

Numerical modeling of the columnar phase is performed in the low  $K_3/K_1$  limit of the LdG system described previously. The results indicate that the tendency of different LCLCs at different initial concentrations to form different local patterns is tied to the elastic properties of the LCLCs

during the drying process. The free energy minimizations qualitatively reproduce the director fields exhibited by the columnar LCLC films (Fig. 4.19). Interestingly, the initialization angle of the director field with respect to the post lattice determines whether the resultant director configuration matches the “square” or “zigzag” configurations seen in experiment. If the initialization angle for the free energy minimization lies on the lattice diagonal, then a director configuration very similar to the “square” configuration is seen; additionally, though no obviously disordered “defect”-like regions are seen, the areas with highest local bend  $b = ((\mathbf{n} \cdot \nabla)\mathbf{n})^2$ , i.e., where a defect wall would most likely occur in a columnar liquid crystal, match qualitatively with the placement of the defect walls seen in experiment. If the director angle is initialized at  $30^\circ$  from the post lattice spacing direction ( $15^\circ$  degrees off-diagonal), then a director configuration similar to the “zigzag” region is reproduced, with defect walls again predicted by high-bend regions.

We note that variation of the ratio of splay and bend elastic constants  $K_1$  and  $K_3$ , respectively, can change the relative stability of these configurations. As can be seen in Fig. 4.19, an initialization angle of  $\alpha = 40^\circ$  with a  $K_3/K_1$  ratio of 0.09 results in a “square” configuration, while the same initialization angle evolving under a  $K_3/K_1$  ratio of 0.03 produces a “zigzag” configuration. The preferred configuration is described in Figure 9 as a function of the deviation of the initialization angle with respect to the lattice diagonal. For  $K_3/K_1 = 0.09$ , the “square” configuration is stable up to an initialization angle deviation of up to  $10^\circ$  off-diagonal; for  $K_3/K_1 = 0.03$ , this configuration is stable up to a deviation of only  $2.5^\circ$ . This finding implies a decreasing stability of the “square” phase and a stability preference of the “zigzag” phase as the  $K_3/K_1$  ratio decreases.

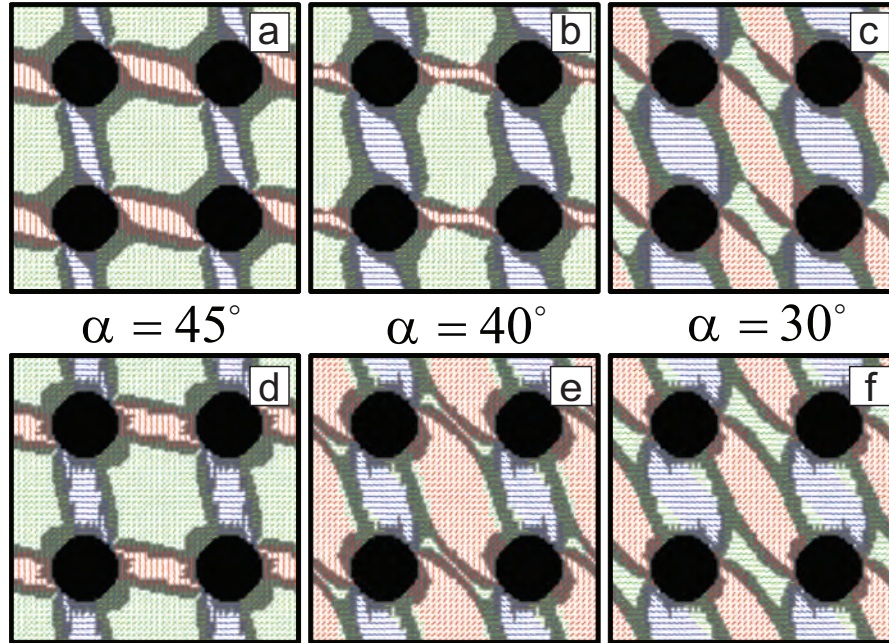


Figure 4.19: Average in-plane director orientations from expanded LdG free energy minimizations in micropillar confinement for effective Frank elastic constant ratios  $K_3/K_1 = 0.09$  (a-c) and  $K_3/K_1 = 0.03$  (d-f) for in-plane director initializations of  $45^\circ$  (a & d),  $40^\circ$  (b & e), and  $30^\circ$  (c & f) from the horizontal post lattice spacing direction. Line coloring highlights distinct regimes of director orientation (blue = close to horizontal, red = most off-horizontal, green = intermediate orientation); darker backgrounds indicate regions with the 40% greatest contribution to Frank free energy bend,  $b = ((\mathbf{n} \cdot \nabla)\mathbf{n})^2$ .

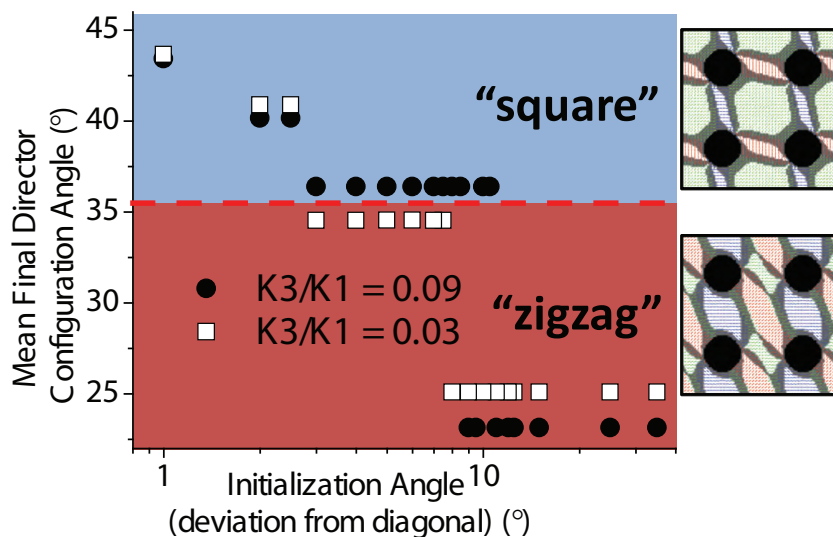


Figure 4.20: Final mean director orientation from expanded LdG free energy minimizations as a function of deviation of initialized director angle from the lattice diagonal. Mean director angles  $> 36^\circ$  correspond to “square” defect wall configurations (blue area of graph); mean director angles  $< 36^\circ$  correspond to “zigzag” defect wall configurations (mauve area of graph). Filled circles represent effective Frank free energy constants  $K_3/K_1 = 0.09$ ; open squares represent effective Frank free energy constants  $K_3/K_1 = 0.03$

This interpretation is consistent with experimental observation and the known elastic properties of the studied LCLCs (see Fig. 4.5). The  $K_3/K_1$  ratio of nematic DSCG at 14 % wt/wt is 2.5 at 25 °C [114]; for nematic SSY at 29% wt/wt, the  $K_3/K_1$  ratio is 1.4, and at 31.5%,  $K_3/K_1 = 0.95$  [189]. Though no experimental determinations of DSCG elastic constants at higher nematic concentrations exist, we expect from general expectations about the nematic-columnar transition [149] and the trends seen in SSY [189] that higher concentrations of DSCG should have a lower  $K_3/K_1$  ratio. In our experiments, systems which have a higher  $K_3/K_1$  in the initial nematic configuration (i.e., nematic DSCG at a concentration  $< 17\%$  wt/wt) form the “square” columnar state. Likewise, systems which have a lower  $K_3/K_1$  in the initial nematic configuration (i.e., nematic DSCG at a higher concentration, and nematic SSY) form the “zigzag” columnar state. Though some of the details of the route from nematic to columnar structure formation

are not worked out, both the experiments and the numerics suggest the same basic control of columnar configurations via modifications of the elastic constants.

## 4.5 Conclusion

We have demonstrated control of patterning of micro-templated aqueous LCLC films by adjusting LC elastic properties. Micropost confinement biases alignment on a preferred direction for nematic films, and columnar films adopt several distinct configurations of defect and director patterns depending on their preparation. These results demonstrate a novel method for inducing alignment of typically difficult-to-align LCLC films, as well as the first instance of two-dimensional patterning of a columnar liquid crystal film. These results serve as a prime example of configuration switching in a LC film due to changes in bulk elastic properties, rather than external boundary conditions or applied fields.

This work could easily lead to new ideas for engineering self-assembled patterned films. Though only a single micropost pattern was studied here, post shape, diameter, height, placement geometry and anchoring conditions can be used as controllable variables (along with a film's elastic properties) for creating a wide variety of novel liquid crystal micropatterns. The observed columnar LCLC films could then serve as templates for self-folding materials, since their director "tiling" resembles the patterning studied in models of such films. [107, 108] Additionally, the patterns and order induced in these LCLC films could be transferred to suspended colloids, suspended nanotubes and bacterial systems to create novel metamaterial films. [38, 113, 120, 146, 188]

## **Chapter 5**

# **Preliminary Results: Novel Microstructures in Lyotropic Chromonic Liquid Crystals**

While the contents of the preceding chapters of this thesis have been published or are about to be sent out for review, they do not summarize the entirety of the work performed in the course of the author's studies. Specifically, in an effort to identify new research directions, many exploratory experiments were performed on lyotropic chromonic liquid crystals (LCLCs). Though the results of these experiments are not quite ready for publication, they open up new and promising avenues for research for future group members.

In this chapter, we review the most promising unpublished preliminary results demonstrating novel microstructures in LCLC suspensions. First, we discuss an extension of the work

on nematic LCLC films in micropost arrays which finds novel twisted microstructures emerging from the deformations of a nematic-isotropic interface. Second, we summarize preliminary experimental results that reveal chiral symmetry breaking of nematic LCLC droplets in microcapillaries. Third, we describe initial experiments that mix LCLCs and surfactant-based liquid crystals in suspension; we find that they phase separate when mixed, and we show that they can co-organize to create interesting assemblies. Finally, we present results from some experimental attempts to suspend giant diblock copolymer vesicles in nematic LCLC suspensions.

## **5.1 Nematic LCLC's in Micropost Arrays with a Deformed Interface**

The experimental methods and motivations for preparing LCLC films in a square array of cylindrical micropillars were discussed extensively in the previous chapter. In the course of performing these experiments, several samples were prepared using a Sunset Yellow film initially in an isotropic state ( $\approx 5\%$  wt/wt). Over time, water in the LCLC film diffuses into the overlying hexadecane, and in the process it slowly drives up the LCLC concentration and causes the film to progress from an isotropic phase, to a nematic phase, and finally to a columnar state. Typically, the regions of higher-concentrations are produced at the edges of the LCLC films and then move in towards the center.

However, in a few samples, the nematic phase initially nucleates from a *surface* of the film, rather than an edge. This typically occurs at the early stages of the evaporation process. This configuration is most likely unstable, and possibly caused by an initial affinity of LCLC molecules for the glass substrate or oil. Nevertheless, a nematic film that is thinner than the full aqueous

film can be observed during the very early stages of evaporation (see Fig. 5.1). Though the surface tension between water and hexadecane is sufficient to keep that particular interface relatively flat, the isotropic-nematic interface surface tension is much lower, and this small surface tension permits significant deformations of the nematic film.

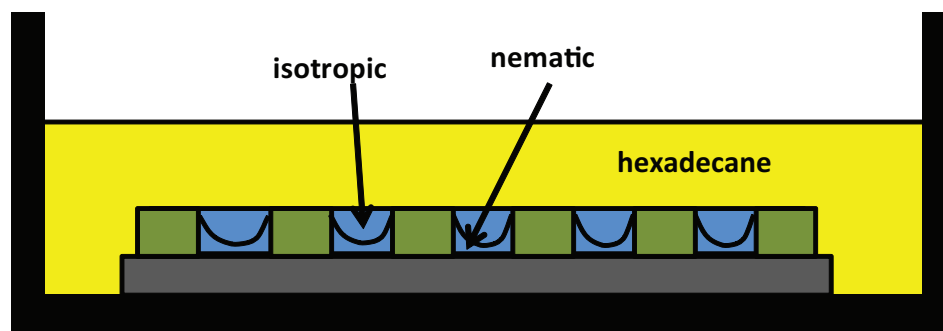


Figure 5.1: Illustration of LCLC film configuration with deformed nematic interfaces. Since the film is in nematic-isotropic coexistence, though the top of the aqueous film is level, the isotropic-nematic interface wets the microposts and deforms.

A new set of boundary conditions is apparent from the very different director configurations seen under crossed-polarizers, though interface deformations are not directly observed. Specifically, we observe two director patterns, one with “pinwheel” textures between each set of four posts, and one with lines running down rows (Fig. 5.2). Rotation of the samples between fixed cross-polarizers yields insight into the underlying director structure. In the “pinwheel” pattern, two defect species appear at the intersection of four dark fringes. Between adjacent posts, these appear to be -1 topological defects (based on the rotation of fringes with respect to the polarizers); at the center of the observed “pinwheels”, these appear to be +1 topological defects. In the line pattern, only -1 defects appear between adjacent posts in a single lattice direction. Note that these textures do not persist when the film has dried sufficiently to be entirely in the nematic phase.

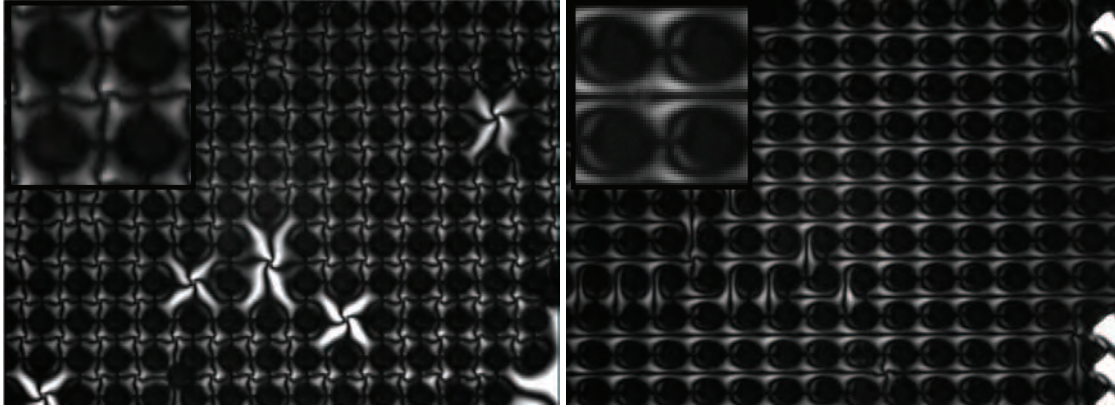


Figure 5.2: Cross-polarizing images of a nematic SSY film (polarizer and analyzer vertical and horizontal, respectively) with a deformed interface. Insets: Enlargements of cross-polarizer texture between four posts.

Though  $\pm 1$  disclinations are unstable structures [105], curved surfaces could stabilize a three dimensional structure with similar apparent topology. In fact, such defects and twisted patterns are seen in sessile droplets of achiral liquid crystals [106], as well as in liquid crystal emulsion droplets with twisted bipole configurations [64]. One might then assume that, like these droplets, the surface close to these  $+1$  defects would have a positive Gaussian curvature.

In fact, the connection between surface curvature and ordering in a liquid crystal film could be deeper than this superficial observation. In a study of sessile nematic LCLC tactoids at an interface [158], it is observed that molecular aggregates have a tendency to align perpendicular to a gradient in film thickness  $\vec{\nabla}h$ , in order to minimize elastic distortions (specifically, splay) given planar degenerate anchoring conditions at the interfaces. It follows that the local curvature of a surface would dictate the local director orientation in a sufficiently thin film.

A guess at the surface geometry of a film wetting four posts in a square lattice allows an interesting comparison to the observed defects in the “pinwheel” pattern. Though the exact wetting configuration needs to be confirmed by more rigorous means, one could assume a minimum

in the surface height between the four posts, and saddle points between the adjacent posts, as sketched in Fig. 5.3. Then, where the height of the surface forms a minimum with a positive local Gaussian curvature, a topological defect of charge +1 forms in the director field. Likewise, at saddle points the local Gaussian curvature is negative, a topological defect of charge -1 is observed. Thus, there appears to be a coupling between the sign of the local Gaussian curvature and the defect topology in the underlying liquid crystal film.

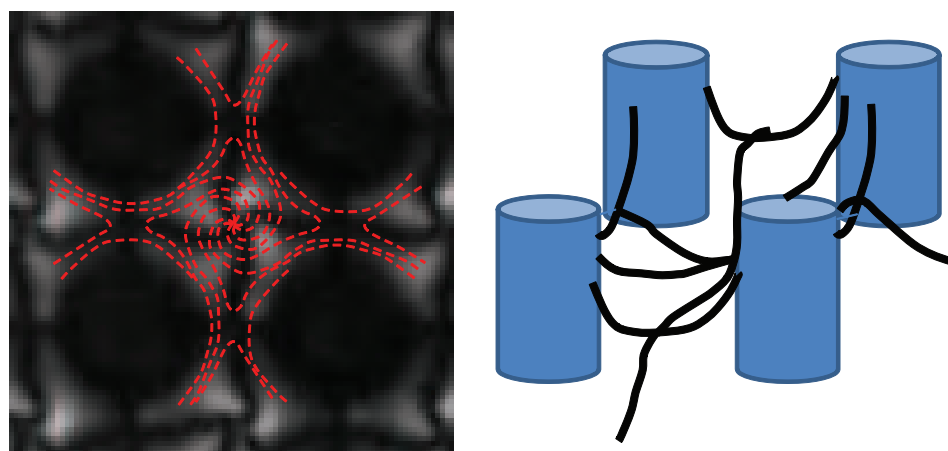


Figure 5.3: (Right) Cross-polarizer image of the “pinwheel” texture with corresponding approximated average in-plane director orientation sketched in red dotted lines. (Left) Illustration of the presumed shape of the deformed nematic-isotropic interface between four posts. Dark lines trace the surface of the interface.

For the future, stable control of the isotropic-nematic interface height and better characterization of the interface shape is necessary to make precise conclusions. Nevertheless, these preliminary results imply that microposts and surface curvature could be useful new tools for lyotropic liquid crystal director patterning. The wide range of isotropic-nematic coexistence in LCLCs (which might not be nearly as feasible in thermotropic LCs) permits relatively stable and deformable nematic interfaces to facilitate this patterning. This micropatterning technique might therefore be specific to LCLCs.

## 5.2 Observations of Chiral LCLC Configurations in Tubes

LCLCs share a common trait with polymer-based lyotropic liquid crystals; they are both more susceptible to twist deformations than splay or bend. Because of this property, nematic LCLCs have been observed to adopt twisted, chiral configurations in achiral microscale confinement. This behavior has been observed in sessile tactoids [158] and spherical emulsion droplets [64]. It follows that other achiral confining microstructures, such as cylindrical confinement, may induce new chiral LCLC structures.

To explore the configurational behavior of LCLCs under cylindrical confinement, we placed suspensions of nematic disodium cromoglycate (DSCG, 14 % wt/wt) in glass microcapillaries with inner diameters ranging from 10 to 100  $\mu\text{m}$ . The unfunctionalized glass capillaries induce planar degenerate anchoring on the LCLC mesogens. One would expect a uniform alignment of the director field along the length of the capillary, as it would result in satisfaction of boundary conditions with no necessary elastic deformations.

The first capillaries we observed, however, i.e., capillaries which had an inner diameter  $< 10 \mu\text{m}$  and which were filled entirely with a uniform nematic phase, exhibited cross-polarizer textures which violated this basic intuition (Fig. 5.4). The entire nematic region appeared bright when viewed under cross-polarizers at a diagonal, indicating average alignment of the director along the length of the tube. However, viewing the sample parallel to either the polarizer or analyzer revealed distinct regions with different brightnesses. This indicates regions with some orientation component not along the tube length. In previous work on sessile nematic tactoids [158], addition of a non-adsorbing polymer was shown to increase the relative cost of splay to twist, or  $K_1/K_2$ , increasing the likelihood of spontaneous twist of the nematic under achiral

confinement. When we add a small amount of PEG to the DSCG solution ( $\approx 1\%$  wt/wt) and again observe the sample under cross-polarizers, we see the same average alignment along the tube length, but we also observe smaller lengthscale intensity fluctuations when viewed parallel to the polarizer. Though the details of these configurations were not entirely clear, there is an implication that DSCG is forming regions with various twists and chiralities.



Figure 5.4: (Top) Nematic DSCG in a microcapillary with inner diameter  $< 10\mu\text{m}$  under cross polarizers. (Bottom) Nematic DSCG with added PEG in a microcapillary with inner diameter  $< 10\mu\text{m}$  under cross polarizers with a full wavelength retardation plate.

Though large nematic domains of DSCG did not exhibit consistent alignment in larger diameter tubes ( $> 30\mu\text{m}$ ), isolated droplets of nematic DSCG (length  $\approx 100\mu\text{m}$ ) demonstrated consistent twisted configurations. Two different types of nematic droplet were observed in these preliminary experiments. By drawing low concentration DSCG in isotropic-nematic coexistence into capillaries, we formed nematic droplets with concave ends (Fig. 5.6). Nematic DSCG

emulsions were made by vigorously shaking a small volume of DSCG suspension heated to the isotropic phase in mineral oil (without any stabilizing surfactants), and immediately vacuuming the suspension into the capillary (Fig. 5.5). This method resulted in nematic droplets with convex ends. In both cases, though droplets would show identical textures under cross-polarizers, the insertion of a full wavelength retardation plate (which distinguishes between director orientations on different diagonals) showed that droplets exhibited different coloration when aligned along a polarizer or analyzer direction. This implies that each droplet has a different chirality of the same twisted configuration.

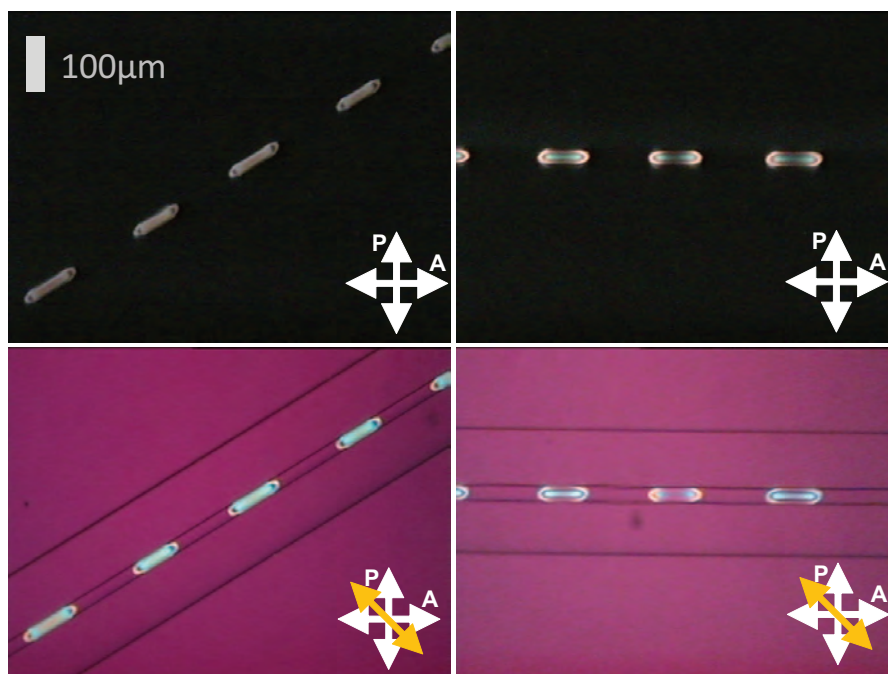


Figure 5.5: DSCG emulsion droplets at 15 % wt/wt suspended in mineral oil in glass microcapillaries, under cross-polarizers (top) and with a full-wavelength retardation plate (bottom).

A basic argument for the appearance of chirality in these droplets would be similar to the one justifying chiral nematic sessile tactoids in [158]. In short, ordering of the mesogens along the length of the tube would require a large splay to be consistent with planar degenerate anchoring at

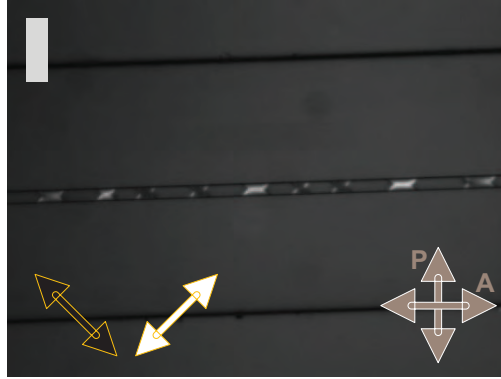


Figure 5.6: Isotropic-nematic coexistence of DSCG in a microcapillary, under cross-polarizers with a full wavelength retardation plate.

the highly curved ends of the droplet. For LCLCs, where twist is much easier than splay ( $K_2 \approx 0.1K_1$ ), this splay deformation gets relieved by adding twist to the system, which propagates along the length of the drop.

This argument does not fully explain the tendency of LCLCs to form chiral domains when surfaces are not involved (as in Fig. 5.4), or for the occasional thicker DSCG sample to form twisting disclination line pairs (as shown in Fig. 5.7). However, these preliminary observations have been followed by more careful and thorough studies of Sunset Yellow (SSY) in capillaries with similar boundary conditions by Joonwoo Jeong and Zoey Davidson. They have not only found that these twisted configurations are very robust, both in droplets and more extended nematic domains, but they have made much more precise characterizations of the twisted configurations. Additionally, in ongoing work, they have developed models which attribute the stability of this twist to higher order expansions of the free energy cost of deformations (i.e.,  $K_{24}$  free energy terms).

Current ongoing work succeeding these preliminary results has largely focused on SSY. It

would be interesting to compare nematic DSCG and SSY under the same confinement conditions, and explore whether their difference in elastic constants cause differences in configuration (as observed in micropost confinement in **Chapter 4**). Additionally, the cylinders observed in more recent experiments have been larger in diameter ( $> 30\mu\text{m}$ ), and it would be interesting to further investigate the chiral structures in micron-scale confinement (shown here in Fig. 5.4).

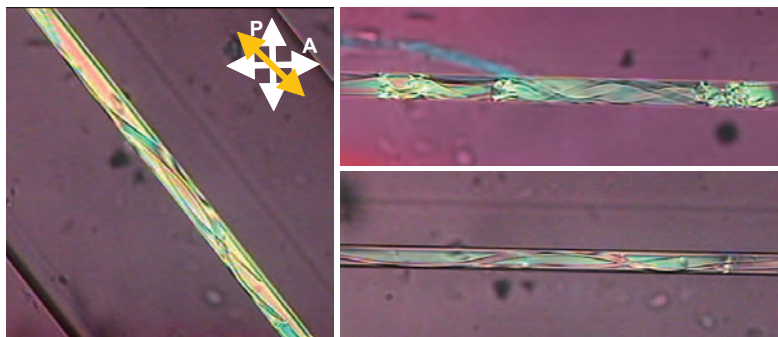


Figure 5.7: Twisted disclination lines observed in nematic DSCG filled capillaries, several days after filling. Viewed under cross-polarizer with full wavelength retarding waveplate.

### 5.3 Mixtures of CLC and Surfactant Phases

Lyotropic and amphiphile-based liquid crystals are quite different from their chromonic counterparts. In addition to having molecular components with substantially different shapes (e.g., a hydrophilic head with a hydrophobic tail, as opposed to a plank-like molecule with ionic side groups), the assembly of these molecules into higher-order structures can be quite different. While molecules in LCLCs aggregate isodesmically and form linear aggregates at all concentrations and temperatures, amphiphiles must reach a critical micelle concentration (CMC) before assembling into micelles and other structures. Additionally, the mesophases formed by amphiphiles are markedly different from the nematic and columnar phases of LCLCs. For example,

amphiphiles can assemble into anisotropic micelles which themselves form nematic calamitic ( $N_c$ ) or nematic discotic ( $N_d$ ) phases. They may also assemble into lamellar layers ( $L_\alpha$ ), hexagonally packed columns ( $H_\alpha$ ), gyroid phases, percolating networks of wormlike micelles, giant vesicles, or multi-layered micelles.

However, since they both classes of lyotropic LCs are aggregate-forming and water-based, it is natural to inquire how surfactants and LCLC-forming molecules might interact in suspension, and whether they might form new and interesting composite liquid crystal mesophases. There exists a single publication so far which attempts such a mixture, and only observes phase separation between hexagonal phases of several amphiphiles and LCLCs [5]. To investigate this possibility in a wider phase space, we mixed varying concentrations of DSCG into aqueous suspensions of sodium dodecyl sulfate (SDS) and decanol or butanol. We choose these particular surfactant / co-surfactant pairings because their phase behaviors are well studied, and because they can form a variety of amphiphilic mesophases at room temperature [14, 145].

Our preliminary experiments found phase separation of the two liquid crystal phases when mixed together in solution. Additionally, even when the surfactant is in a low-concentration isotropic micellar phase, the chromonic (LCLC) regions form phase-separated columnar domains (Fig. 5.8). This is probably driven by the crowding/depletion effect of the surfactant micelles, i.e., similar behavior to what is seen in the addition of non-adsorbing polymer to LCLC suspensions [121, 158, 159].

More uniform suspensions can be created from mixtures of high concentration surfactant phases with the addition of dilute chromonic molecules. Though the chromonic will locally concentrate (due to the crowding effects seen in [121, 158, 159]) into columnar bands, the ordering

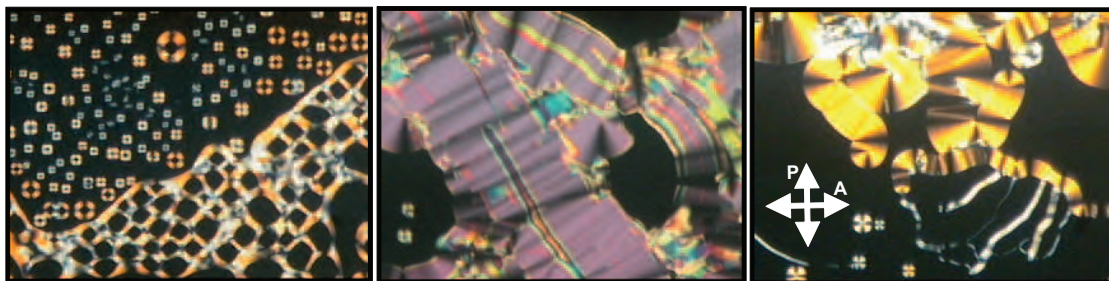


Figure 5.8: Cross-polarizing images of 15% wt/wt SDS/butanol mixture in 10% wt/wt aqueous DSCG solution. The system exhibits nematic-isotropic and/or columnar-isotropic coexistence via crowding effects.

of these bands is greatly influenced by the liquid crystal phase of the surrounding surfactant/co-surfactant mixture (Fig. 5.9). When the surfactant is in a nematic calamitic state, i.e., when the surfactant forms ellipsoidal micelles aligned in the same direction, thin chromonic columnar bands align in the same direction of the surfactant nematic director. In a lamellar surfactant state, the characteristic “oily streak” polarizing textures become more pronounced with the addition of chromonic molecules. As these “oily streaks” indicate borders between well-aligned lamellar regions, this indicates the concentration of columnar LCLC domains at the borders of ordered lamellar regions. In hexagonal columnar or nematic discotic phases, a combination of these two behaviors is seen, with chromonic bands forming both along local director orientations and at boundaries between ordered domains.

This ordering of columnar chromonic bands in surfactants could have interesting new implications. By adding a very dilute amount of chromonic additive ( $< 5\%$  wt/wt) to these surfactant suspensions, one can create percolating structures of columnar bands which drastically change the rheological and optical properties of the surfactant suspension. This effect could be utilized to modify the properties of surfactant-based rheology modifiers in products ranging from consumer products to fracking fluids for enhanced oil recovery. Additionally, these percolating columnar

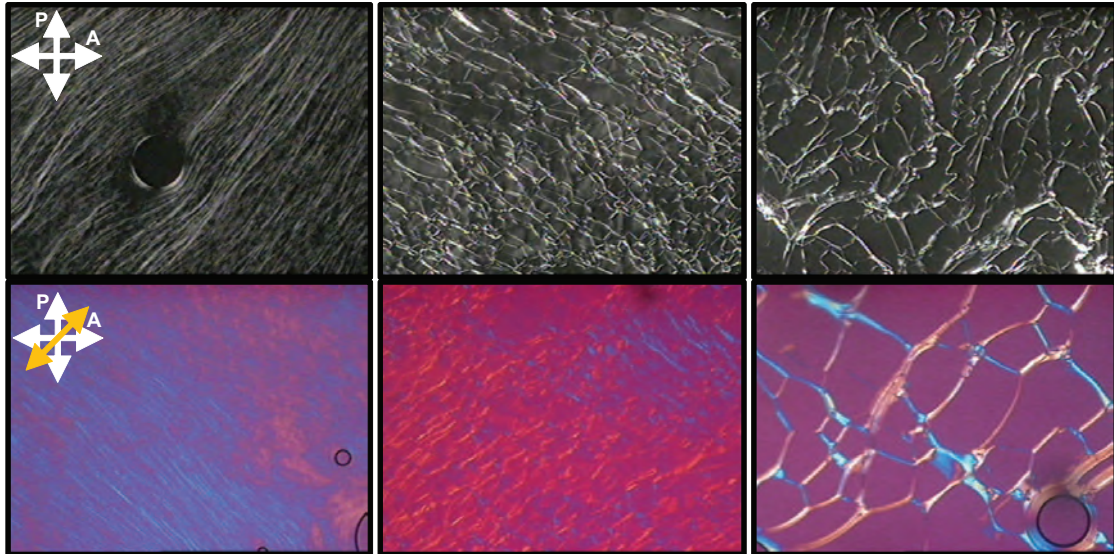


Figure 5.9: Variety of SDS/decanol/water mesophases including 3% wt/wt DSCG (top, cross-polarizer, bottom, cross-polarizer with full-wavelength retarding waveplate). Left: SDS/decanol in nematic calamitic ( $N_C$ ) phase (5% decanol, 33.5% SDS). Middle: SDS/decanol in nematic discotic ( $N_D$ ) phase (5.9% decanol, 31% SDS)/ Right: SDS/decanol in lamellar ( $L_\alpha$ ) phase (9.4% decanol, 29.2% SDS).

bands structures could have novel electrically conductive properties different from those seen in uniform LCLC films [115], depending on the underlying surfactant phase structure.

#### 5.4 Diblock Copolymer Vesicles Suspended in CLCs

The bio-compatibility of aqueous LCLC suspensions make them quite appealing for applications detecting and manipulating biological molecules and micro-organisms [113, 144, 146, 168, 188]. As such, it is important to understand not only the chemical, but the physical effects of the liquid crystal on cell-like materials. Diblock copolymers can form giant bilayer vesicles which serve as simple models of cells in suspension [91]. By suspending these vesicles in nematic suspensions, interesting distortions of these vesicles might be observed through elastic interactions with the surrounding nematic, yielding important insight into the behavior of flexible micro-organisms

in nematics. Additionally, the shape of these vesicles could couple to the nematic director in LCLCs to form novel configurations. This would be unique behavior compared to droplets in thermotropic nematic emulsions, which have a high enough surface tension to remain spherical [97, 134].

To create such vesicle suspensions, we follow a well-practiced method [91], substituting a sugar/water mixture with a nematic suspension of DSCG. After suspending a PEO-PBD diblock copolymer in chloroform and drying the suspension to a film on the inside of a glass vial, we fill the vial with a nematic DSCG suspension (15% wt/wt), and heat the system to 60 ° C for 24 hours. This causes vesicles to bud and separate from the dried polymer film and enter the suspension.

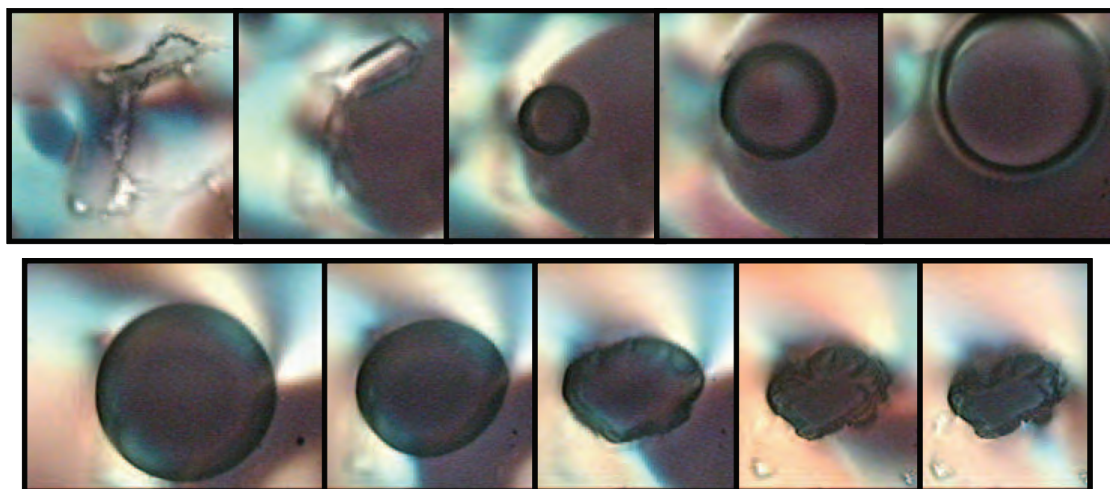


Figure 5.10: Cross-polarizing images of PEO-PBD vesicle in nematic DSCG shortly after initial suspension. Top: Temperature increase from 25C to 36C (left to right) induces swelling of crumpled vesicle. Bottom: Cooling from 36C to 25C (left to right) causes vesicle to deswell and crumple.

Hours after cooling the system to room temperature, most diblock structures observed appeared to be highly crumpled or burst vesicles, or unstructured polymer aggregates. One particular vesicle was observed which appeared intact, with no nematic LCLC phase in its interior. Upon heating to 36°C, the outside nematic melted to the isotropic phase, and the crumpled vesicle swelled to a large, smooth sphere. Upon cooling back to room temperature, the vesicle deswelled and crumpled. Though this swelling/deswelling was repeatable, it was only observed in a single vesicle, so drawing general conclusions about this behavior may as yet be premature.

After leaving the sample unperturbed for three days, multiple uncrumpled vesicles filled with nematic phase LCLC were observed. Though the shape of these vesicles varied, tactoidal geometries were fairly prevalent. Observation of this system during heating and cooling indicates that these shapes do not necessarily arise from elastic interactions with the nematic director. Rather, it appears that vesicles adsorb onto moving isotropic-nematic interfaces, which in turn appears to stretch the vesicles into the observed tactoidal shapes.

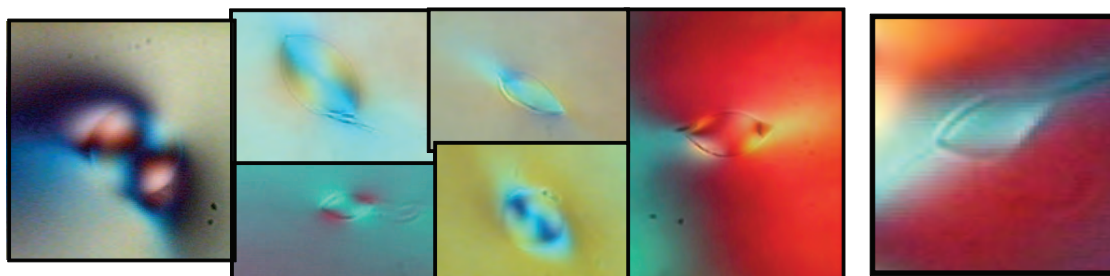


Figure 5.11: Vesicles in nematic DSCG 3 days after initial cooling, under cross-polarizers. Image at the far right demonstrates deformation of vesicle shape by a moving isotropic-nematic interface.

These preliminary results demonstrate some interesting new potential uses for LCLCs. The vesicle swelling/deswelling behavior implies that temperature-induced changes in the chromonic phase and aggregate size may be a novel way to control osmotic pressure in an aqueous system.

Additionally, careful control of the moving isotropic-nematic fronts using temperature gradients may be an interesting new way for deforming and assembling microstructures.

## 5.5 Summary

The preliminary experiments with LCLC suspensions that we have described in this chapter are not “finished” or conclusive, but they offer interesting results which merit further study. The structures observed in micropost arrays with a deformed interface suggest an interesting new mechanism for patterning nematic films through modulation of film thickness and curvature. The initial studies of LCLCs in microtubes have inspired further study which demonstrates a non-intuitive yet robust emergence of chiral structure. The mixtures of chromonic and amphiphilic liquid crystal phases can potentially be controlled to make a variety of co-organized structures. Finally, though preliminary experiments on diblock copolymer vesicles in nematic LCLC revealed a behavior more complicated than expected, they demonstrate some potentially interesting properties of LCLCs related to osmotic pressure and isotropic-nematic interface surface tension. With finer experimental design and control, the underlying physical mechanisms of these systems should become clear, allowing for precise characterization of new methods for aqueous microstructure assembly.

These experiments also serve to inspire a wide variety of general, less explored ideas for useful new applications of LCLCs. The wide coexistence regime of isotropic and nematic phases (which can be made more stable through the addition of additives [121, 158, 159]) allows for the creation of novel water-water interfaces. These interfaces, though strong enough to drag and manipulate vesicles and colloidal particles, have a much lower surface tension than the

more common oil-water interfaces. These might then serve as novel and flexible templates for colloidal assembly. Additionally, though the structure, dynamics and stability of chromonic molecular aggregates is a widely researched field, the temperature tunability of their size and concentration provides an unutilized system for control of osmotic pressure. Consequently, as is shown in some preliminary experiments not discussed in this text, dilute, isotropic chromonic suspensions could provide a new mechanism for tunable colloidal depletion.

## Chapter 6

# Conclusions and Future Work

### 6.1 Summary

The research presented in this thesis elucidates physical properties of a variety of novel microstructures in soft matter. The helical packings, the glass-gel transition, and the microtemplated aqueous liquid crystals presented in the preceding chapters all exhibit novel phase and configuration behavior upon rigorous analysis of their microscopic structure and dynamics. Further, such analyses provide insight into the microscopic mechanisms behind formation of stable and structured soft materials.

The first study, presented in **Chapter 2**, clarified questions about the stability of quasi-1D helical structures in thermal equilibrium via microscopic observations of colloids in cylindrical confinement. By packing fluorescent microgel spheres in a glass capillary of slightly larger diameter and then imaging the system with confocal microscopy, we were able to characterize a variety of helical structures at a microscopic scale. When we decreased sample volume

fraction using the thermosensitive properties of the microgel particles, we found the first experimental evidence of stable helical crystals under thermal Brownian fluctuations. Further, by decreasing the volume fraction of these packings more and by tracking the evolving structure and dynamics, we were able to quantitatively characterize of the melting behavior of these “helical phases”. We find evidence for a potentially discontinuous crossover between ordered and disordered states using measurements of the long-range orientational order and local orientational susceptibility. This presence of long-range order was validated with theoretical calculations on a tightly wrapped two-dimensional model with similar structure. In confirming the stability of this ordered phase, we not only provide a powerful counter-example to the argument against the stability of one-dimensional translationally ordered structures [126, 162], but we demonstrate that thermal fluctuations are not a technical barrier to fabrication of such structures on a microscopic scale. Additionally, we find that changes in volume fraction result in transitions between ordered phases prior to melting, and that these transitions are not mediated by the well-understood movement of dislocations seen in athermal media. With careful engineering, this trait could provide a novel mechanism for materials with temperature-tunable microscale pitch or chirality.

The second study identified a vibrational signature of the crossover between gel-like and glassy states in aggregating colloidal suspensions (i.e., suspension with particles that have attractive short-range interactions). In **Chapter 3**, we presented careful experiments with particles and a binary-fluid-induced wetting-based attraction. In particular, we devised a novel method for creating strongly attractive monolayers of quasi-2D attractive colloidal particles which still exhibit Brownian vibrations at high densities. We then implemented a method for extracting the vibrational modes from particle trajectories in a series of samples of attractive packings with

varying packing fraction and spatial heterogeneity. The shape of the resulting vibrational density of states curves classified these packings into two categories of relatively sparse (“gel-like”) and dense (“glassy”) packings. While the dense packings show vDOS curves qualitatively similar to previously observed glassy packings, the sparse packings exhibit an excess of low-frequency modes which appear to be highly localized to microstructures with low local coordination. Beyond providing a distinct characterization of disordered packings into more glass-like and gel-like states, this result provides the beginnings of a micro-structural definition of otherwise poorly defined “gel” phases.

**Chapter 4** presented an investigation of patterning and defect formation in lyotropic chromonic liquid crystal (LCLC) films in micropost arrays. Through a combination of experiment (on two different LCLC formers, disodium cromoglycate (DSCG) and Sunset Yellow (SSY)) and numerical free energy minimizations, we demonstrated that square patterns of anisotropic cylindrical microposts can be used to induce ordering in a nematic liquid crystal film along a diagonal of the square lattice. Then, by allowing these nematic films to dry into the columnar phase, multiple patterns of defects and director orientations were induced from a single microtemplate. Through extensions of nematic numerical techniques to the columnar limits, we were able to demonstrate that these different structures arise as a result of competition between splay and bend deformations in the LC film. These patterns can thus be controlled through careful modification of the elastic properties of the liquid crystals.

The potential of LCLCs to create various other novel microstructures is demonstrated through preliminary work on a variety of aqueous liquid crystal dispersions described in **Chapter 5**. By

forming nematic films in the same micropatterned template described in **Chapter 4** under a deformed interface, we demonstrate a novel micropatterning technique from modulations of film thickness. Preliminary experiments on LCLCs confined to microtubes demonstrated spontaneous chiral symmetry breaking in achiral confinement which is being further explored in ongoing work. Mixtures of LCLC's with concentrated surfactant dispersions demonstrate ordered phase separation in multiple lyotropic liquid crystals with tunable structure. Finally, dispersions of diblock copolymer vesicles in a nematic LCLC demonstrate novel uses of LCLCs for micro-manipulation using temperature-tunable osmotic pressure and isotropic-nematic interfaces.

## **6.2 Future Work**

The following section describes potential fruitful avenues for continued research on the colloidal and liquid crystal systems presented in this thesis.

### **6.2.1 Three Dimensional Dynamics and Self-Assembly of Helical Structures**

As discussed in detail in **Chapter 2**, precise three dimensional particle tracking of pNIPAm microspheres in glass microcapillaries is difficult due to imaging artifacts from the highly-curved, index mismatched surfaces involved in the experimental setup. This does not mean that precise three dimensional trajectories are completely inaccessible to a more sophisticated experimental system, however. Recent work has shown that pNIPAm particles synthesized through a semi-batch process are more homogeneously polymerized, and as a result, are much better index-matched to water [148]. Additionally, pNIPAm particles with fluorescent cores would be far easier to distinguish at high densities than the particles we have employed in our investigations.

Assuming the index matching of the aqueous solvent to the capillary can be addressed, more precise three dimensional tracking could then be used to examine new structural order parameters more carefully. Specific interesting analyses would include a careful examination of dislocation structures at boundaries of ordered packings with different pitch or chirality, the radial distribution and dynamics of particles, and vibrational density of states calculations using the methods outlined in **Chapter 3**.

The stability of helical quasi-1D packings begs a more thorough fundamental investigation of orientational order in confined dimensions. Though we argue that orientational order could be stable in these packings due to the quasi-2D nature of the packings, extensions of the arguments against 1D order [126,162] could be made that disprove such orientational stability. Also, observations of longer helical structures could demonstrate a finite correlation length of orientational order dependent on inter-particle interactions. The stability of orientational order might thus be a result of interactions of the particles with the highly curved cylindrical boundary. Though the improved experimental resolution described above (as well as a larger sample size/field of view) would certainly serve to clarify such points, a more rigorous theoretical treatment incorporating the ordering effects of boundaries might provide a more thorough explanation for these effects. Even without a better theoretical explanation, it might be interesting to examine the stability of orientational order in hard sphere simulations. Simulational studies of sphere packings in tubes to date examine translational order without probing orientational order [46]. It would also be interesting to theoretically and experimentally study other quasi-1D systems with orientational order. For example, anisotropic particles (e.g. ellipsoids, cubes, trimers, etc.), or particles with anisotropic interactions (e.g. Janus particles, magnetic dipoles) confined to a

one-dimensional chain might exhibit orientational order beyond a certain pressure, though they might not exhibit long-range translational order. Also, it would be interesting to study experimental analogues of simulated systems which *always* exhibit long-range orientational order, for example, rods/anisotropic particles free to rotate in two dimensions and translate only along a fixed line [50, 70].

Though placing particles in a cylinder is a simple method for creating helical packings, there is evidence that such packings could also be self-assembled from colloids with complex anisotropic interactions. For example, suspensions of so-called Janus particles with dipolar interactions have been shown to create chain-like structures with some degree of helical order [56]. Additionally, simulations of spherical particles with competing long-range dipolar and short-range attraction have predicted the self-assembly of helical structures with the exact pitch determined by fine tuning of these interactions [131]. Though this system has not yet been experimentally realized, a colloidal analogue could be produced in a relatively straightforward manner using well-characterized techniques. A tunable short-range attraction could be induced by the addition of a size-changing depleting polymer or surfactant, or a binary phase separating solvent (as used in **Chapter 3**). A tunable long-range dipolar interaction could be produced by applying a uniform magnetic field to superparamagnetic colloids or applying a strong oscillating electric field to index-mismatched particles. Though the engineering of such a system would take time, and both potentials would need to be carefully tuned to have strengths on the order of  $\approx 1k_B T$ , it is certainly within the realm of possibility. Once these structures were assembled, it would be interesting to see how their phase behavior compared to the confined short-range repulsive thermal system studied in **Chapter 2**.

## 6.2.2 Precise Structural Nature and Generality of the Gel-Glass Crossover

The exact structural nature of the low-frequency modes which characterize sparse, gel-like packings is still unclear, despite the finding of a correlation between areas with low local coordination and highly localized vibrational modes presented in **Chapter 3**. We have found qualitative correlation of these modes to local “linear” structures; however, the correlation is not one-to-one (i.e., not all linear structures dominate low-frequency modes, and not all low-frequency modes are localized to linear structures). A more rigorous analysis of the structures surrounding these localized low-frequency modes would better help to define gel-like packings based on their morphology alone.

Additionally, the experiments described in **Chapter 3** only observe this low-frequency signature of states in a rather specific set of two-dimensional morphologies. Whether or not this signature would be observed in other classes of high-density attractive particles is crucial to determining the generality of this gel-glass crossover. It would thus be useful to apply this same analysis to short-range attractive packings at identical area fractions with coarser, sparser or more fractal structures. Additionally, it would be interesting to see whether short-range attractive particles stabilized by long-range repulsion and “patchy” particles with a limited attractive valence (i.e., systems which approach gel states through non-aggregated, “equilibrium” states as proposed in [181]) show similar behavior. It would also be helpful to see if this vibrational crossover can be applied to three-dimensional systems, assuming three-dimensional confocal imaging could be performed at a fast enough speed to capture simultaneous particle displacements and thus calculate vibrational modes. Replicating these results in numerical simulations would also serve to verify the generality of this crossover.

A connection must be made between these microscopic vibrational behaviors and bulk rheological properties to give the described analysis more pertinent physical meaning. The localized modes in sparse packings might correspond the fragile regions of the packing in the same way that localized low frequency modes in dense disordered packings correlate to rearrangement-prone regions. The breaking of these “fragile” bonds might correlate to cluster-breaking relaxations observed in the multi-step yielding of attractive packings [86]. This correlation could be experimentally probed by calculating vibrational modes and then observing consequent shears in colloidal packings using confocal rheometer setups (such as those used in [6]) or more sophisticated apparatuses which induce local shear using magnetic fields [73] or optical tweezers.

### **6.2.3 Further Engineering of LCLC films via Microtemplating**

The control of local director microstructure in LCLC films by micropost arrays and bulk LC elastic properties is shown by the work in **Chapter 4** to be a powerful new microengineering technique. However, a large range of possibilities for fabricating a whole menagerie of microstructures through variations of microtemplating geometry remains largely unexplored. The size, spacing, height, shape, anchoring conditions and placement geometry of microposts could all be varied to create a wide variety of stable structures in nematic and columnar films. Recently discovered methods for inducing homeotropic anchoring on LCLCs [65] would allow for the creation of microposts geometries with hybrid boundary conditions, allowing exploration of LCLCs in the post-aligned bistable nematic structures studied in [77–79]. Additionally, LCLC films could be modified with the addition of polymer and ionic additives [121, 158, 159] to explore a wider range of elastic properties. The micropattern formation demonstrated in LCLCs should also be generalizable to other lyotropic and thermotropic liquid crystals, which could

exhibit an even wider variety of elastic properties.

Micropost arrays created from polymers sensitive to external conditions could be used to fabricate dynamically switchable LC micropattern configurations. For example, posts fabricated from thermosensitive pNIPAm polymer would change size with temperature. Preliminary simulations on nematics confined between microposts of different size (performed by the author) saw a continuous transition between alignment along the post diagonal (small posts) and alignment along the lattice directions (large posts). In this setup, tuning the temperature of pNIPAM microposts would then tune the alignment angle of LC director. Similar dynamically controllable patterns could be imagined using posts of tunable shape fabricated from liquid crystal elastomers.

Additionally, as the “tile” like pattern of interlocking aligned domains formed in columnar LCLC films resemble the patterns predicted to make novel self-folding materials [107, 108], it would be a challenging but novel engineering task to transfer these micropatterns to elastically anisotropic films and observe their bulk properties. Also, films with switchable configurations could be made from context-sensitive polymers. For example, one could make a membrane with micropores that open and close with changes in the film elasticity. Additionally, one could consider using the defect patterns in the columnar films as nucleation/concentration/patterning points for depositing nanoparticle solutions. If the nanoparticles used are conductive, this could be an interesting method for printing novel circuits at a microscopic scale.

#### **6.2.4 Continuing Work on Novel LCLC-Facilitated Microstructures**

Finally, the preliminary results put forth in **Chapter 5** initiate the first steps of several future projects on microstructures precipitated in-and-by LCLCs. To reiterate specifically, by utilizing the low surface tension of the isotropic-nematic interface, one can create nematic micropatterns

governed by undulations in film thickness. The twisted configurations of LCLCs in cylinders are already under thorough investigation. The ordering of columnar LCLC bands in surfactants is a promising method for making structurally and rheologically unique materials. Though vesicles exhibit interesting structural behavior in LCLCs, more carefully designed experiments might see these effects better controlled.

These experiments also serve to inspire a wide variety of general, less explored ideas for useful new applications of LCLCs. The wide coexistence regime of isotropic and nematic phases (which can be made more stable through the addition of additives [121, 158, 159]) allows for the creation of novel water-water interfaces. These interfaces, though strong enough to drag and manipulate vesicles and colloidal particles, have a much lower surface tension than the more common oil-water interfaces. These might then serve as novel and flexible templates for colloidal assembly. Additionally, though the structure, dynamics and stability of chromonic molecular aggregates is a widely researched field, the temperature tunability of their size and concentration provides an unutilized system for control of osmotic pressure. Consequently, as is shown in some preliminary experiments not discussed in this text, dilute, isotropic chromonic suspensions could provide a new mechanism for tunable colloidal depletion.

# Bibliography

- [1] A. M. Alsayed, M. F. Islam, J. Zhang, P. J. Collings, and A. G. Yodh. Premelting at defects within bulk colloidal crystals. *Science* **309**(5738), 1207–1210 AUG (2005).
- [2] P. W. Anderson. Through the glass lightly. *Science* **267**(5204), 1615–1616 MAR (1995).
- [3] V. Anderson and H. Lekkerkerker. Insights into phase transition kinetics from colloid science. *Nature* **416**(6883), 811–815 APR 25 (2002).
- [4] T. Aste, M. Saadatfar, and T. J. Senden. Geometrical structure of disordered sphere packings. *Physical Review E* **71**(6) JUN (2005).
- [5] T. Attwood, J. E. Lydon, C. Hall, and G. J. T. Tiddy. The distinction between chromonic and amphiphilic lyotropic mesophases. *Liquid Crystals* **7**, 657–668 (1990).
- [6] A. Basu, Q. Wen, X. Mao, T. C. Lubensky, P. A. Janmey, and A. G. Yodh. Nonaffine displacements in flexible polymer networks. *Macromolecules* **44**(6), 1671–1679 MAR 22 (2011).
- [7] J. Bergenholtz and F. M. Nonergodicity transitions in colloidal suspensions with attractive interactions. *Physical Review E* **59**(5), 5706–5715 MAY (1999).

- [8] D. Beysens and T. Narayanan. Wetting-induced aggregation of colloids. *Journal of Statistical Physics* **95**(5-6), 997–1008 JUN (1999).
- [9] P. Boltenhagen and N. Pittet. Structural transitions in crystalline foams. *Europhysics Letters* **41**(5), 571–576 MAR (1998).
- [10] P. Boltenhagen, N. Pittet, and N. Rivier. Giant deformations and topological hysteresis of an ordered foam. *Europhysics Letters* **43**(6), 690–694 SEP (1998).
- [11] N. Bowden, S. Brittain, A. Evans, J. Hutchinson, and G. Whitesides. Spontaneous formation of ordered structures in thin films of metals supported on an elastomeric polymer. *Nature* **393**(6681), 146–149 MAY 14 (1998).
- [12] C. Brito and M. Wyart. Heterogeneous dynamics, marginal stability and soft modes in hard sphere glasses. *Journal of Statistical Mechanics - Theory and Experiment* AUG (2007).
- [13] C. Brito and M. Wyart. Geometric interpretation of previtrification in hard sphere liquids. *Journal of Chemical Physics* **131**(2) JUL (2009).
- [14] G. Burducea. Lyotropic liquid crystals ii. structural polymorphism. *Romanian Reports in Physics* **56**(1), 87–100 (2004).
- [15] M. Cavallaro, M. Gharbi, D. Beller, S. Copar, Z. Shi, T. Baumgart, S. Yang, R. Kamien, and K. Stebe. Exploiting imperfections: Directed assembly of surface colloids via bulk topological defects. *Proceeding of the National Academy of Sciences* **110**(47), 18804–18808 November (2013).

- [16] P. Chaikin and T. C. Lubensky. *Principles of Condensed Matter Physics*. Cambridge University Press Cambridge (2006).
- [17] D. T. N. Chen, Q. Wen, P. A. Janmey, J. C. Crocker, and A. G. Yodh. Rheology of soft materials. *Annual Review of Condensed Matter Physics* **1**, 301–322 (2010).
- [18] K. Chen, W. Ellenbroak, Z. Zhang, D. Chen, P. Yunker, S. Henkes, C. Brito, O. Dauchot, W. van Saarloos, A. Liu, and A. Yodh. Low-frequency vibrations of soft colloidal glasses. *Physical Review Letters* **105**(2) JUL 9 (2010).
- [19] K. Chen, M. Manning, P. Yunker, W. Ellenbroek, Z. Zhang, A. Liu, and A. Yodh. Measurement of correlations between low-frequency vibrational modes and particle rearrangements in quasi-two-dimensional colloidal glasses. *Physical Review Letters* **107**(10) AUG 31 (2011).
- [20] K. Chen, T. Still, S. Schoenholz, K. Aptowicz, M. Schindler, A. Maggs, A. Liu, and A. Yodh. Phonons in two-dimensional soft colloidal crystals. *Physical Review E* **88**(2) (2013).
- [21] S. Chui. Grain-boundary theory of melting in 2 dimensions. *Physical Review B* **28**(1), 178–194 (1983).
- [22] A. I. Chumakov, G. Monaco, A. Monaco, W. A. Crichton, A. Bosak, R. Rüffer, A. Meyer, F. Kargl, L. Comez, D. Fioretto, H. Giefers, S. Roitsch, G. Wortmann, M. H. Manghnani, A. Hushur, Q. Williams, J. Balogh, K. Parliński, P. Jochym, and P. Piekarczyk. Equivalence of the boson peak in glasses to the transverse acoustic van hove singularity in crystals. *Physical Review Letters* **106**, 225501 May (2011).

- [23] A. Ciferri. *Polymer Liquid Crystals*. Materials science and technology. Elsevier Science (1982).
- [24] A. Coniglio, T. Abete, A. de Candia, E. Del Gado, and A. Fierro. Dynamical heterogeneities: from glasses to gels. *Journal of Physics: Condensed Matter* **20**(49), 494239 DEC (2008).
- [25] M. L. Cowan, J. H. Page, and P. Sheng. Ultrasonic wave transport in a system of disordered resonant scatterers: Propagating resonant modes and hybridization gaps. *Physical Review B* **84**(9), 094305 SEP 19 (2011).
- [26] J. Crocker and D. Grier. Methods of digital video microscopy for colloidal studies. *Journal of Colloidal Interface Science* **179**(1), 298 (1996).
- [27] J. Cuesta and A. Sanchez. General non-existence theorem for phase transitions in one-dimensional systems with short range interactions, and physical examples of such transitions. *Journal of Statistical Physics* **115**(3-4), 869–893 MAY (2004).
- [28] V. K. de Souza and P. Harrowell. Unconstrained motions, dynamic heterogeneities, and relaxation in disordered solids. *Physical Review E* **80**(4) OCT (2009).
- [29] P. G. Debenedetti and F. H. Stillinger. Supercooled liquids and the glass transition. *Nature* **410**(6825), 259–267 MAR (2001).
- [30] C. J. Dibble, M. Kogan, and M. J. Solomon. Structure and dynamics of colloidal depletion gels: Coincidence of transitions and heterogeneity. *Physical Review E* **74**(4), 041403 OCT (2006).

- [31] C. J. Dibble, M. Kogan, and M. J. Solomon. Structural origins of dynamical heterogeneity in colloidal gels. *Physical Review E* **77**(5), 050401 MAY (2008).
- [32] J. Dreyer. The fixing of molecular orientation. *Journal of Physical and Colloid Chemistry* **52**(5), 808–810 (1948).
- [33] F. J. Duran-Olivencia and M. C. Gordillo. Ordering of hard spheres inside hard cylindrical pores. *Physical Review E* **79**(6) JUN (2009).
- [34] A. Eberle, R. Castaneda-Priego, J. Kim, and N. Wagner. Dynamical arrest, percolation, gelation, and glass formation in model nanoparticle dispersions with thermoreversible adhesive interactions. *Langmuir* **28**(3), 1866–1878 JAN 24 (2012).
- [35] T. Eckert and E. Bartsch. Re-entrant glass transition in a colloid-polymer mixture with depletion attractions. *Physical Review Letters* **89**(12), 125701 SEP (2002).
- [36] M. D. Ediger and P. Harrowell. Perspective: Supercooled liquids and glasses. *Journal of Chemical Physics* **137** AUG (2012).
- [37] R. O. Erickson. Tubular packing of spheres in biological fine structure. *Science* **181**(4101), 705–716 (1973).
- [38] J. S. Evans, C. N. Beier, and I. I. Smalyukh. Alignment of high-aspect ratio colloidal gold nanoplatelets in nematic liquid crystals. *Journal of Applied Physics* **110**(3), 033535 AUG 1 (2011).

- [39] L. Fabbian, W. Gotze, F. Sciortino, P. Tartaglia, and F. Thiery. Ideal glass-glass transitions and logarithmic decay of correlations in a simple system. *Physical Review E* **59**(2), R1347–R1350 FEB (1999).
- [40] L. Feng, R. Dreyfus, R. Sha, N. C. Seeman, and P. M. Chaikin. Dna patchy particles. *Advanced Materials* **25**(20), 2779–2783 MAY 28 (2013).
- [41] U. Gasser, E. Weeks, A. Schofield, P. Pusey, and D. Weitz. Real-space imaging of nucleation and growth in colloidal crystallization. *Science* **292**(5515), 258–262 APR 13 (2001).
- [42] A. Ghosh, V. Chikkadi, P. Schall, and D. Bonn. Connecting structural relaxation with the low frequency modes in a hard-sphere colloidal glass. *Physical Review Letters* **107**(18) OCT 31 (2011).
- [43] A. Ghosh, V. Chikkadi, P. Schall, J. Kurchan, and D. Bonn. Density of states of colloidal glasses. *Physical Review Letters* **104**(24) JUN 17 (2010).
- [44] M. A. Glaser and N. A. Clark. Melting and liquid structure in two dimensions. *Advances in Chemical Physics* **83**, 543–709 (1993).
- [45] C. P. Goodrich, W. G. Ellenbroek, and A. J. Liu. Stability of jammed packings i: the rigidity length scale. *Soft Matter* **9**(46), 10993–10999 (2013).
- [46] M. C. Gordillo, B. Martinez-Haya, and J. M. Romero-Enrique. Freezing of hard spheres confined in narrow cylindrical pores. *Journal of Chemical Physics* **125**(14) OCT (2006).

- [47] M. Gratale, P. Yunker, K. Chen, T. Still, K. Aptowicz, and A. Yodh. Phonons in two-dimensional colloidal crystals with bond-strength disorder. *Physical Review E* **87**(5) MAY 8 (2013).
- [48] N. L. Green, D. Kaya, C. E. Maloney, and M. F. Islam. Density invariant vibrational modes in disordered colloidal crystals. *Physical Review E* **83**(5), 051404 MAY 27 (2011).
- [49] F. Guo, A. Mukhopadhyay, B. W. Sheldon, and R. H. Hurt. Vertically aligned graphene layer arrays from chromonic liquid crystal precursors. *Advanced Materials* **23**(4), 508+ JAN 25 (2011).
- [50] P. Gurin and S. Varga. Orientational ordering of hard zigzag needles in one dimension. *Physical Review E* **82**, 041713 Oct (2010).
- [51] Y. Han, N. Y. H. Ha, A. M. Alsayed, and A. G. Yodh. Melting of two-dimensional tunable-diameter colloidal crystals. *Physical Review E* **77**(4) APR (2008).
- [52] Y. Han, Y. Shokef, A. M. Alsayed, Y. P., T. C. Lubensky, and A. G. Yodh. Geometric frustration in buckled colloidal monolayers. *Nature* **456**(7224), 898–903 DEC (2008).
- [53] W. F. Harris and R. O. Erickson. Tubular arrays of spheres - geometry, continuous and discontinuous contraction, and the role of moving dislocations. *Journal of Theoretical Biology* **83**(2), 215–246 (1980).
- [54] S. Henkes, C. Brito, and O. Dauchot. Extracting vibrational modes from fluctuations: a pedagogical discussion. *Soft Matter* **8**(22), 6092–6109 (2012).

- [55] C. Hertlein, L. Helden, A. Gambassi, S. Dietrich, and C. Bechinger. Direct measurement of critical casimir forces. *Nature* **451**(7175), 172–175 JAN 10 (2008).
- [56] L. Hong, A. Cacciuto, E. Luijten, and S. Granick. Clusters of amphiphilic colloidal spheres. *Langmuir* **24**(3), 621–625 FEB (2008).
- [57] A. Honglawan, D. A. Beller, M. Cavallaro, R. D. Kamien, K. J. Stebe, and S. Yang. Pillar-assisted epitaxial assembly of toric focal conic domains of smectic-a liquid crystals. *Advanced Materials* **23**(46), 5519+ DEC 8 (2011).
- [58] A. Honglawan, D. A. Beller, M. Cavallaro, Jr., R. D. Kamien, K. J. Stebe, and S. Yang. Topographically induced hierarchical assembly and geometrical transformation of focal conic domain arrays in smectic liquid crystals. *Proceedings of the National Academy of the Sciences* **110**(1), 34–39 JAN 2 (2013).
- [59] L. A. Hough, M. F. Islam, B. Hammouda, A. G. Yodh, and P. A. Heiney. Structure of semidilute single-wall carbon nanotube suspensions and gels. *Nano Letters* **6**(2), 313–317 FEB (2006).
- [60] L. E. Hough, H. T. Jung, D. Krueerke, M. S. Heberling, M. Nakata, C. D. Jones, D. Chen, D. R. Link, J. Zasadzinski, and G. Heppke. Helical nanofilament phases. *Science* **325**(5939), 456–460 JUL (2009).
- [61] H. C. Huang, S. K. Kwak, and J. K. Singh. Characterization of fluid-solid phase transition of hard-sphere fluids in cylindrical pore via molecular dynamics simulation. *Journal of Chemical Physics* **130**(16) APR (2009).

- [62] G. L. Hunter and E. R. Weeks. The physics of the colloidal glass transition. *Reports on Progress in Physics* **75**(6) JUN (2012).
- [63] M. Islam, A. Alsayed, Z. Dogic, J. Zhang, and T. Lubensky. Nematic nanotube gels. *Physical Review Letters* **92**(8), 088303 FEB (2004).
- [64] J. Jeong, Z. Davidson, P. Collings, T. Lubensky, and A. Yodh. Chiral symmetry breaking and surface faceting in chromonic liquid crystal droplets with giant elastic anisotropy. *Proceedings of the National Academy of Sciences* **111**(5), 1742–1747 (2014).
- [65] J. W. Jeong, G. H. Han, A. T. C. Johnson, P. J. Collings, T. C. Lubensky, and A. G. Yodh. Homeotropic alignment of lyotropic chromonic liquid crystals using noncovalent interactions. *Langmuir* **30**(10), 2914–2920 MAR (2014).
- [66] L. Jiang, J. de Folter, J. Huang, A. Philipse, W. Kegel, and A. Petukhov. Helical colloidal sphere structures through thermo-reversible co-assembly with molecular microtubes. *ANGEWANDTE CHEMIE-INTERNATIONAL EDITION* **52**(12), 3364–3368 (2013).
- [67] R. D. Kamien, P. Le Doussal, and D. R. Nelson. Theory of directed polymers. *Physical Review A* **45**, 8727–8750 Jun (1992).
- [68] R. D. Kamien and D. R. Nelson. Defects in chiral columnar phases: Tilt-grain boundaries and iterated moiré maps. *Phys. Rev. E* **53**, 650–666 Jan (1996).
- [69] R. D. Kamien and J. Toner. Anomalous elasticity of polymer cholesterics. *Phys. Rev. Lett.* **74**, 3181–3184 Apr (1995).

- [70] Y. Kantor and M. Kardar. One-dimensional gas of hard needles. *Physical Review E* **79**(4) APR (2009).
- [71] T. Kawasaki and H. Tanaka. Structural signature of slow dynamics and dynamic heterogeneity in two-dimensional colloidal liquids: glassy structural order. *Journal of Physics - Condensed Matter* **23**(19), 194121 MAY 18 (2011).
- [72] D. Kaya, N. Green, C. Maloney, and M. Islam. Normal modes and density of states of disordered colloidal solids. *Science* **329**(5992), 656–658 AUG 6 (2010).
- [73] N. C. Keim and P. E. Arratia. Mechanical and microscopic properties of the reversible plastic regime in a 2d jammed material. *Physical Review Letters* **112**(2), 028302 JAN 15 (2014).
- [74] P. Keim, G. Maret, U. Herz, and H. von Grunberg. Harmonic lattice behavior of two-dimensional colloidal crystals. *Physical Review Letters* **92**(21), 215504 MAY 28 (2004).
- [75] A. N. Khlobystov, D. A. Britz, A. Ardavan, and G. A. D. Briggs. Observation of ordered phases of fullerenes in carbon nanotubes. *Physical Review Letters* **92**(24) JUN (2004).
- [76] J. B. Kim, P. Kim, N. C. Pegard, S. J. Oh, C. R. Kagan, J. W. Fleischer, H. A. Stone, and Y.-L. Loo. Wrinkles and deep folds as photonic structures in photovoltaics. *Nature Photonics* **6**(5), 327–332 MAY (2012).
- [77] S. Kitson and A. Geisow. Controllable alignment of nematic liquid crystals around microscopic posts: Stabilization of multiple states. *Applied Physics Letters* **80**(19), 3635–3637 MAY 13 (2002).

- [78] S. C. Kitson, E. G. Edwards, and A. D. Geisow. Designing liquid crystal alignment surfaces. *Applied Physics Letters* **92**(7), 073503 FEB 18 (2008).
- [79] S. Kitson and A. Geisow. Bistable alignment of nematic liquid crystals around microscopic posts. *Molecular Crystals and Liquid Crystals* **412**, 1763–1771 (2004). 19th International Liquid Crystal Conference, EDINBURGH, SCOTLAND, JUN 30-JUL 05, 2002.
- [80] C. Kittel. Phase transition of a molecular zipper. *American Journal of Physics* **37**(9), 917 (1969).
- [81] H. Kleinert. Disclinations and 1st order transitions in 2d melting. *Physics Letters A* **99**(7), 381–384 (1983).
- [82] M. Kleman and P. Oswald. Defects in hexagonal discotic mesophases - disclinations and walls. *Journal de Physique* **42**(10), 1461–1472 (1981).
- [83] M. Kleman and P. Oswald. Columnar discotic mesophases - elasticity, dislocations, instabilities. *Journal de Physique* **43**(4), 655–662 (1982).
- [84] K. Koga and H. Tanaka. Close-packed structures and phase diagram of soft spheres in cylindrical pores. *Journal of Chemical Physics* **124**(13) APR (2006).
- [85] J. M. Kosterlitz and D. J. Thouless. Ordering, metastability and phase-transitions in 2 dimensional systems. *Journal of Physics C - Solid State Physics* **6**(7), 1181–1203 (1973).
- [86] N. Koumakis and G. Petekidis. Two step yielding in attractive colloids: transition from gels to attractive glasses. *Soft Matter* **7**(6), 2456–2470 (2011).

- [87] M. Kozubek, S. Kozubek, E. Lukasova, E. Bartova, M. Skalnikova, P. Matula, P. Matula, P. Jirsova, A. Cafourkova, and I. Koutna. Combined confocal and wide-field high-resolution cytometry of fluorescent in situ hybridization-stained cells. *CYTOMETRY* **45**(1), 1–12 SEP 1 (2001).
- [88] M. Kroon, W. L. Vos, and G. H. Wegdam. Structure and formation of a gel of colloidal disks. *Physical Review E* **57**(2), 1962–1970 FEB (1998).
- [89] A. Latka, Y. Han, A. M. Alsayed, A. B. Schofield, A. G. Yodh, and P. Habdas. Particle dynamics in colloidal suspensions above and below the glass-liquid re-entrance transition. *Europhysics Letters* **86**(5), 58001 JUN (2009).
- [90] M. Laurati, S. U. Egelhaaf, and G. Petekidis. Nonlinear rheology of colloidal gels with intermediate volume fraction. *Journal of Rheology* **55**(3), 673–706 MAY-JUN (2011).
- [91] J. Lee, H. Bermudez, B. Discher, M. Sheehan, Y. Won, F. Bates, and D. Discher. Preparation, stability, and in vitro performance of vesicles made with diblock copolymers. *Biotechnology and Bioengineering* **73**(2), 135–145 APR 20 (2001).
- [92] F. Li, X. Badel, J. Linnros, and J. B. Wiley. Fabrication of colloidal crystals with tubular-like packings. *Journal of the American Chemical Society* **127**(10), 3268–3269 MAR (2005).
- [93] I.-H. Lin, D. S. Miller, P. J. Bertics, C. J. Murphy, J. J. de Pablo, and N. L. Abbott. Endotoxin-induced structural transformations in liquid crystalline droplets. *Science* **332**(6035), 1297–1300 JUN 10 (2011).

- [94] M. A. Lohr, A. M. Alsayed, B. G. Chen, Z. Zhang, R. D. Kamien, and A. G. Yodh. Helical packings and phase transformations of soft spheres in cylinders. *Physical Review E* **81**(4), 040401 APR (2010).
- [95] M. A. Lohr, J. Cavallaro, Marcello, A. Beller, Daniel, K. J. Stebe, D. Kamien, Randall, P. J. Collings, and A. G. Yodh. Elasticity-dependent self-assembly of micro-templated chromonic liquid crystal films. *Soft Matter* **10**(19), 3477 – 3484 (2014).
- [96] P. J. Lu, E. Zaccarelli, C. F. A. B. Schofield, F. Sciortino, and D. A. Weitz. Gelation of particles with short-range attraction. *Nature* **453**(7194), 499–U4 MAY (2008).
- [97] T. Lubensky, D. Petey, N. Currier, and H. Stark. Topological defects and interactions in nematic emulsions. *Physical Review E* **57**(1), 610–625 JAN (1998).
- [98] J. Lydon. Chromonic review. *Journal of Materials Chemistry* **20**(45), 10071–10099 (2010).
- [99] J. Lydon. Chromonic liquid crystalline phases. *Liquid Crystals* **38**(11-12, SI), 1663–1681 (2011).
- [100] L. A. Lyon, J. D. Debord, S. B. Debord, C. D. Jones, J. G. McGrath, and M. J. Serpe. Microgel colloidal crystals. *Journal of Physical Chemistry B* **108**(50), 19099–19108 DEC (2004).
- [101] M. Manning and A. Liu. Vibrational modes identify soft spots in a sheared disordered packing. *Physical Review Letters* **107**(10) AUG 31 (2011).

- [102] D. Matsunaga, T. Tamaki, H. Akiyama, and K. Ichimura. Photofabrication of micro-patterned polarizing elements for stereoscopic displays. *Advanced Materials* **14**(20), 1477+ OCT 16 (2002).
- [103] J. T. McGinley, I. Jenkins, T. Sinno, and J. C. Crocker. Assembling colloidal clusters using crystalline templates and reprogrammable dna interactions. *Soft Matter* **9**(38), 9119–9128 (2013).
- [104] C. K. McGinn, L. I. Laderman, N. Zimmermann, H. S. Kitzerow, and P. J. Collings. Planar anchoring strength and pitch measurements in achiral and chiral chromonic liquid crystals using 90-degree twist cells. *Physical Review E* **88**(0), 062513 DEC (2013).
- [105] R. B. Meyer. On the existence of even indexed disclinations in nematic liquid crystals. *Philosophical Magazine* **27**(2), 405424 (1973).
- [106] D. Meyerhofer, R. Williams, and A. Sussman. Electrooptic and hydrodynamic properties of nematic liquid films with free surfaces. *Journal of Applied Physics* **43**(9), 3685 (1972).
- [107] C. D. Modes and M. Warner. Blueprinting nematic glass: Systematically constructing and combining active points of curvature for emergent morphology. *Physical Review E* **84**(2, 1), 021711 AUG 30 (2011).
- [108] C. D. Modes, M. Warner, C. Sanchez-Somolinos, L. T. de Haan, and D. Broer. Angular deficits in flat space: remotely controllable apertures in nematic solid sheets. *Proceedings of the Royal Society A-Mathematical and Physical and Engineering Sciences* **469**(2153), 20120631 MAY 8 (2013).

- [109] J. H. Moon, S. Kim, G. R. Yi, Y. H. Lee, and S. M. Yang. Fabrication of ordered macroporous cylinders by colloidal templating in microcapillaries. *Langmuir* **20**(5), 2033–2035 MAR (2004).
- [110] A. Mukhopadhyay, F. Guo, A. Tokranov, X. Xiao, R. H. Hurt, and B. W. Sheldon. Engineering of graphene layer orientation to attain high rate capability and anisotropic properties in li-ion battery electrodes. *Advanced Functional Materials* **23**(19), 2397–2404 MAY 20 (2013).
- [111] M. Muller. *Introduction to Confocal Fluorescence Microscopy*. Tutorial Text Series. Society of Photo Optical (2006).
- [112] C. A. Murray and D. H. VanWinkle. Experimental-observation of 2-stage melting in a classical two-dimensional screened coulomb system. *Physical Review Letters* **58**(12), 1200–1203 MAR (1987).
- [113] P. C. Mushenheim, R. R. Trivedi, H. H. Tuson, D. B. Weibel, and N. L. Abbott. Dynamic self-assembly of motile bacteria in liquid crystals. *Soft Matter* **10**, 88–95 (2014).
- [114] Y. Nastishin, K. Neupane, A. Baldwin, O. Lavrentovich, and S. Sprint. Elasticity and viscosity of a lyotropic chromonic nematic studied with dynamic light scattering. *electronic-Liquid Crystal Communications* JULY (2008).
- [115] V. G. Nazarenko, O. P. Boiko, M. I. Anisimov, A. K. Kadashchuk, Y. A. Nastishin, A. B. Golovin, and O. D. Lavrentovich. Lyotropic chromonic liquid crystal semiconductors for water-solution processable organic electronics. *Applied Physics Letters* **97**(26), 263305 DEC 27 (2010).

- [116] V. G. Nazarenko, O. P. Boiko, H. S. Park, O. M. Brodyn, M. M. Omelchenko, L. Tortora, Y. A. Nastishin, and O. D. Lavrentovich. Surface alignment and anchoring transitions in nematic lyotropic chromonic liquid crystal. *Physical Review Letters* **105**(1) JUN 28 (2010).
- [117] D. R. Nelson and B. I. Halperin. Dislocation-mediated melting in 2 dimensions. *Physical Review B* **19**(5), 2457–2484 (1979).
- [118] C. O’Hern, L. E. Silbert, A. J. Liu, and S. R. Nagel. Jamming at zero temperature and zero applied stress: The epitome of disorder. *Physical Review E* **68**(1) JUL (2003).
- [119] M. O’Neill and S. M. Kelly. Ordered materials for organic electronics and photonics. *Advanced Materials* **23**(5), 566–584 FEB 1 (2011).
- [120] N. Ould-Moussa, C. Blanc, C. Zamora-Ledezma, O. D. Lavrentovich, I. I. Smalyukh, M. F. Islam, A. G. Yodh, M. Maugey, P. Poulin, A. E., and M. Nobili. Dispersion and orientation of single-walled carbon nanotubes in a chromonic liquid crystal. *Liquid Crystals* **40**(12), 1628–1635 (2013).
- [121] H.-S. Park, S.-W. Kang, L. Tortora, S. Kumar, and O. D. Lavrentovich. Condensation of self-assembled lyotropic chromonic liquid crystal sunset yellow in aqueous solutions crowded with polyethylene glycol and doped with salt. *Langmuir* **27**(7), 4164–4175 APR 5 (2011).
- [122] H.-S. Park, S.-W. Kang, L. Tortora, Y. Nastishin, D. Finotello, S. Kumar, and O. D. Lavrentovich. Self-assembly of lyotropic chromonic liquid crystal sunset yellow and

- effects of ionic additives. *Journal of Physical Chemistry B* **112**(51), 16307–16319 DEC 25 (2008).
- [123] S. K. Park, S. E. Kim, D. Y. Kim, S. W. Kang, S. Shin, S. W. Kuo, S. H. Hwang, S. H. Lee, M. H. Lee, and K. U. Jeong. Polymer-stabilized chromonic liquid-crystalline polarizer. *Advanced Functional Materials* **21**(11), 2129–2139 JUN (2011).
- [124] J. Pawley. *Handbook of Biological Confocal Microscopy*. Cognition and Language. Springer Dordrecht (1995).
- [125] R. Peierls. *Surprises in Theoretical Physics*. Princeton series in physics. Princeton University Press Princeton, NJ (1979).
- [126] R. Peierls. *More Surprises in Theoretical Physics*. Princeton University Press Princeton, NJ (1991).
- [127] R. Pelton. Temperature-sensitive aqueous microgels. *Advances in Colloid and Interface Science* **85**(1), 1–33 FEB (2000).
- [128] K. N. Pham, G. Petekidis, D. Vlassopoulos, S. U. Egelhaaf, W. C. K. Poon, and P. N. Pusey. Yielding behavior of repulsion- and attraction-dominated colloidal glasses. *Journal of Rheology* **52**(2), 649–676 (2008).
- [129] K. N. Pham, G. Petekidis, D. Vlassopoulos, S. U. Egelhaaf, P. N. Pusey, and W. C. K. Poon. Yielding of colloidal glasses. *Europhysics Letters* **75**(4), 624–630 AUG (2006).

- [130] K. N. Pham, A. M. Puertas, J. Bergenholtz, S. U. Egelhaaf, A. Moussaid, P. N. Pusey, A. B. Schofield, M. E. Cates, M. Fuchs, and W. C. K. Poon. Multiple glassy states in a simple model system. *Science* **296**(5565), 104–106 APR (2002).
- [131] G. T. Pickett, M. Gross, and Okuyama. Spontaneous chirality in simple systems. *Physical Review Letters* **85**(17), 3652–3655 OCT (2000).
- [132] N. Pittet, P. Boltenhage, N. Rivier, and D. Weaire. Structural transitions in ordered, cylindrical foams. *Europhysics Letters* **35**(7), 547–552 SEP (1996).
- [133] N. Pittet, N. Rivier, and D. Weaire. Cylindrical packing of foam cells. *Forma* **10**(1), 65–73 (1995).
- [134] P. Poulin, H. Stark, T. Lubensky, and D. Weitz. Novel colloidal interactions in anisotropic fluids. *Science* **275**(5307), 1770–1773 MAR 21 (1997).
- [135] P. Pusey and W. VanMegen. Phase behavior of concentrated suspensions of nearly hard colloidal spheres. *Nature* **320**(6060), 340–342 MAR 27 (1986).
- [136] P. Pusey, W. VanMegen, P. Bartlett, B. Ackerson, J. Rarity, and S. Underwood. Structure of crystals of hard colloidal spheres. *Physical Review Letters* **63**(25), 2753–2756 DEC 18 (1989).
- [137] A. Rapini and M. J. Papoular. Distortion d’une lamelle nématique sous champ magnétique conditions d’ancrage aux parois. *J. Phys. (Paris) Colloq.* **30**, C4–54 (1969).
- [138] M. Ravnik and S. Zumer. Landau-de Gennes modelling of nematic liquid crystal colloids. *Liquid Crystals* **36**(10-11), 1201–1214 (2009).

- [139] L. Rovigatti, W. Kob, and F. Sciortino. The vibrational density of states of a disordered gel model. *Journal of Chemical Physics* **135**(10) (2011).
- [140] B. R. Saunders and B. Vincent. Microgel particles as model colloids: theory, properties and applications. *Advances in Colloid and Interface Science* **80**(1), 1–25 FEB (1999).
- [141] M. Schindler and A. Maggs. Truncated correlations in video microscopy of colloidal solids. *Soft Matter* **8**(14), 3864–3874 (2012).
- [142] T. Scopigno, G. Ruocco, F. Sette, and G. Monaco. Is the fragility of a liquid embedded in the properties of its glass? *Science* **302**(5646), 849–852 OCT (2003).
- [143] H. Shintani and H. Tanaka. Universal link between the boson peak and transverse phonons in glass. *Nature Materials* **7**(11), 870–877 NOV (2008).
- [144] S. Shiyanovskii, O. Lavrentovich, T. Schneider, T. Ishikawa, I. Smalyukh, C. Woolverton, G. Niehaus, and K. Doane. Lyotropic chromonic liquid crystals for biological sensing applications. *Molecular Crystals and Liquid Crystals* **434**, 587–598 (2005). 20th Biennial International Liquid Crystal Conference, Ljubljana, SLOVENIA, JUL 04-09, 2004.
- [145] J. Sjoblom, A. Blokhus, M. Wei, and S. FRiberg. Surfactants and cosurfactants in lamellar liquid crystals and adsorbed on solid-surfaces 1. the model system sodium dodecyl-sulfate butanol or sodium dodecyl-sulfate benzyl alcohol and alpha-alumina. *Journal of Colloid and Interface Science* **140**(2), 481–491 DEC (1990).
- [146] I. I. Smalyukh, J. Butler, J. D. Shrouf, M. R. Parsek, and G. C. L. Wong. Elasticity-mediated nematiclike bacterial organization in model extracellular dna matrix. *Physical Review E* **78**(3), 030701 (2008).

- [147] T. Still, C. P. Goodrich, K. Chen, P. J. Yunker, S. Schoenholz, A. J. Liu, and A. G. Yodh. Phonon dispersion and elastic moduli of two-dimensional disordered colloidal packings of soft particles with frictional interactions. *Physical Review E* **89**(1) JAN (2014).
- [148] T. Still, K. Chen, A. M. Alsayed, K. B. Aptowicz, and A. G. Yodh. Synthesis of micrometer-size poly(n-isopropylacrylamide) microgel particles with homogeneous crosslinker density and diameter control. *Journal of Colloid and Interface Science* **405**, 96–102 SEP 1 (2013).
- [149] J. Swift and B. Andereck. Statics and dynamics near the nematic-columnar phase-transition in liquid-crystals. *Journal de Physique Lettres* **43**(12), L437–L440 (1982).
- [150] S.-W. Tam-Chang and L. Huang. Chromonic liquid crystals: properties and applications as functional materials. *Chemical Communications* (17), 1957–1967 MAY 7 (2008).
- [151] S. Tam-Chang, J. Helbley, T. Carson, W. Seo, and I. Iverson. Template-guided organization of chromonic liquid crystals into micropatterned anisotropic organic solids. *Chemical Communications* (5), 503–505 FEB 7 (2006).
- [152] H. Tanaka, T. Kawasaki, H. Shitani, and K. Watanabe. Critical-like behavior of glass-forming liquids. *Nature Materials* **9**(5), 324–331 APR (2010).
- [153] S. Taraskin and S. R. Elliott. Vibrations in disordered systems. *Physica B* **316**, 81–88 MAY (2002).
- [154] V. Taratuta and R. Meyer. Elasticity of a nematic polymer in the infinite molecular chain limit. *Liquid Crystals* **2**(3), 373–379 MAY-JUN (1987).

- [155] R. Thurston, J. Cheng, and G. Boyd. Mechanically bistable liquid-crystal display structures. *IEEE Transactions on Electron Devices* **27**(11), 2069–2080 (1980).
- [156] C. M. Tone, M. P. De Santo, and F. Ciuchi. Alignment of chromonic liquid crystals: A difficult task. *Molecular Crystals and Liquid Crystals* **576**(1), 2–7 JUL 1 (2013).
- [157] C. M. Tone, M. P. De Santo, M. G. Buonomenna, G. Golemme, and F. Ciuchi. Dynamical homeotropic and planar alignments of chromonic liquid crystals. *Soft Matter* **8**(32), 8478–8482 (2012).
- [158] L. Tortora and O. D. Lavrentovich. Chiral symmetry breaking by spatial confinement in tactoidal droplets of lyotropic chromonic liquid crystals. *Proceedings of the National Academy of the Sciences* **108**(13), 5163–5168 MAR 29 (2011).
- [159] L. Tortora, H.-S. Park, S.-W. Kang, V. Savaryn, S.-H. Hong, K. Kaznatcheev, D. Finotello, S. Sprunt, S. Kumar, and O. D. Lavrentovich. Self-assembly, condensation, and order in aqueous lyotropic chromonic liquid crystals crowded with additives. *Soft Matter* **6**(17), 4157–4167 (2010).
- [160] V. Trappe, V. Prasad, L. Cipelletti, P. N. Segre, and D. A. Weitz. Jamming phase diagram for attractive particles. *Nature* **411**(6839), 772–775 JUN (2001).
- [161] M. Tymczenko, L. F. Marsal, T. Trifonov, I. Rodriguez, F. Ramiro-Manzano, J. Pallares, A. Rodriguez, R. Alcubilla, and F. Meseguer. Colloidal crystal wires. *Advanced Materials* **20**(12), 2315 JUN (2008).
- [162] L. Van Hove. Sur l’integrale de configuration pour les systemes de particules a une dimension. *Physica* **16**(2), 137–142 FEB (1950).

- [163] W. van Meegen. Dynamical perspective of the freezing transition of a suspension of hard spheres from the velocity autocorrelation function. *Physical Review E* **73**(2), 020503 FEB (2006).
- [164] G. Vroege and H. Lekkerkerker. Phase-transitions in lyotropic colloidal and polymer liquid-crystals. *Reports on Progress in Physics* **55**(8), 1241–1309 (1992).
- [165] A. Widmer-Cooper, H. Perry, P. Harrowell, and D. R. Reichman. Irreversible reorganization in a supercooled liquid originates from localized soft modes. *Nature Physics* **4**(9), 711–715 SEP (2008).
- [166] S. Williams, G. Bryant, I. Snook, and W. van Meegen. Velocity autocorrelation functions of hard-sphere fluids: Long-time tails upon undercooling. *Physical Review Letters* **96**(8), 087801 MAR 3 (2006).
- [167] D. Wood, C. Santangelo, and A. Dinsmore. Self-assembly on a cylinder: a model system for understanding the constraint of commensurability. *Soft Matter* **9**(42), 10016–10024 (2013).
- [168] C. Woolverton, E. Gustely, L. Li, and O. Lavrentovich. Liquid crystal effects on bacterial viability. *Liquid Crystals* **32**(4), 417–423 APR (2005).
- [169] M. Wyart, L. Silbert, S. Nagel, and T. Witten. Effects of compression on the vibrational modes of marginally jammed solids. *Physical Review E* **72**(2) (2005).
- [170] N. Xu, V. Vitelli, A. J. Liu, and S. R. Nagel. Anharmonic and quasi-localized vibrations in jammed solids modes for mechanical failure. *Europhysics Letters* **90**(5), 56001 (2010).

- [171] T. Yamazaki, K. Kuramochi, D. Takagi, Y. Homma, F. Nishimura, N. Hori, K. Watanabe, S. Suzuki, and Y. Kobayashi. Ordered fullerene nanocylinders in large-diameter carbon nanotubes. *Nanotechnology* **19**(4) JAN (2008).
- [172] J. Yin, J. L. Yaguee, D. Eggenpieler, K. K. Gleason, and M. C. Boyce. Deterministic order in surface micro-topologies through sequential wrinkling. *Advanced Materials* **24**(40), 5441–5446 OCT 23 (2012).
- [173] A. P. Young. Melting and the vector coulomb gas in two dimensions. *Physical Review B* **19**(4), 1855–1866 (1979).
- [174] P. Yunker, Z. Zhang, K. Aptowicz, and A. Yodh. Irreversible rearrangements, correlated domains, and local structure in aging glasses. *Physical Review Letters* **103**(11) SEP 11 (2009).
- [175] P. J. Yunker, M. Gratale, M. A. Lohr, T. Still, T. C. Lubensky, and A. G. Yodh. Influence of particle shape on bending rigidity of colloidal monolayer membranes and particle deposition during droplet evaporation in confined geometries. *Physical Review Letters* **108**(22), 228303 JUN 1 (2012).
- [176] P. J. Yunker, M. A. Lohr, T. Still, A. Borodin, D. J. Durian, and A. G. Yodh. Effects of particle shape on growth dynamics at edges of evaporating drops of colloidal suspensions. *Physical Review Letters* **110**(3), 035501 JAN 18 (2013).
- [177] P. J. Yunker, T. Still, M. A. Lohr, and A. Yodh. Suppression of the coffee-ring effect by shape-dependent capillary interactions. *Nature* **476**(7360), 308–311 AUG 18 (2011).

- [178] P. Yunker, K. Chen, M. Gratale, M. Lohr, T. Still, and A. Yodh. Physics in ordered and disordered colloidal matter composed of poly(*n*-isopropyl acrylamide) microgel particles. *Reports on Progress in Physics* **77**(5), 056601 (2014).
- [179] P. Yunker, K. Chen, Z. Zhang, and A. Yodh. Phonon spectra, nearest neighbors, and mechanical stability of disordered colloidal clusters with attractive interactions. *Physical Review Letters* **106**(22) JUN 1 (2011).
- [180] P. Yunker, Z. Zhang, M. Gratale, K. Chen, and A. Yodh. Relationship between neighbor number and vibrational spectra in disordered colloidal clusters with attractive interactions. *Journal of Chemical Physics* **138**(12) MAR 28 (2013).
- [181] E. Zaccarelli. Colloidal gels: equilibrium and non-equilibrium routes. *Journal of Physics: Condensed Matter* **19**(32) (2007).
- [182] E. Zaccarelli and W. Poon. Colloidal glasses and gels: The interplay of bonding and caging. *Proceedings of the National Academy of Sciences* **106**(36), 15203–15208 (2009).
- [183] A. Zaccone, H. Wu, and E. Del Gado. Elasticity of arrested short-ranged attractive colloids: Homogeneous and heterogeneous glasses. *Physical Review Letters* **103**(20) NOV 13 (2009).
- [184] K. Zahn, R. Lenke, and G. Maret. Two-stage melting of paramagnetic colloidal crystals in two dimensions. *Physical Review Letters* **82**(13), 2721–2724 MAR (1999).
- [185] Z. Zhang, P. Yunker, P. Habdas, and A. Yodh. Cooperative rearrangement regions and dynamical heterogeneities in colloidal glasses with attractive versus repulsive interactions. *Physical Review Letters* **107**(20) NOV 11 (2011).

- [186] Z. Zhang, I. Jones, H. Schriemer, J. Page, D. Weitz, and P. Sheng. Wave transport in random media: The ballistic to diffusive transition. *Physical Review E* **60**(4), 4843–4850 OCT (1999).
- [187] Z. Zhang, N. Zu, D. Chen, P. Yunker, A. Alsayed, K. Aptowicz, P. Habdas, A. Liu, S. Nagel, and A. Yodh. Thermal vestige of the zero-temperature jamming transition. *Nature* **495**(7244), 230–233 MAY 14 (2009).
- [188] S. Zhou, A. Sokolov, O. D. Lavrentovich, and I. S. Aranson. Living liquid crystals. *Proceedings of the National Academy of Sciences* **111**(4), 12651270 (2014).
- [189] S. Zhou, Y. A. Nastishin, M. M. Omelchenko, L. Tortora, V. G. Nazarenko, O. P. Boiko, T. Ostapenko, T. Hu, C. C. Almasan, S. N. Sprunt, J. T. Gleeson, and O. Lavrentovich. Elasticity of lyotropic chromonic liquid crystals probed by director reorientation in a magnetic field. *Physical Review Letters* **109**(3), 037801 JUL 18 (2012).
- [190] J. Zhu, M. Li, R. Rogers, W. Meyer, R. Ottewill, W. Russell, and P. Chaikin. Crystallization of hard-sphere colloids in microgravity. *Nature* **387**(6636), 883–885 JUN 26 (1997).